NTNU
Norwegian University of
Science and Technology

Impact Behaviour of Stiffened Aluminium Plates

Even Josten Lien
Aleksander Skyrud

Civil and Environmental Engineering
Submission date: June 2016
Supervisor: Magnus Langseth, KT
Co-supervisor: David Morin, KT

Norwegian University of Science and Technology
Department of Structural Engineering

Department of Structural Engineering
Faculty of Engineering Science and Technology
NTNU- Norwegian University of Science and Technology

ACCESSIBILITY:

Open

MASTER THESIS 2016

SUBJECT AREA:	DATE:	NO. OF PAGES:
Structural mechanics	June 2016	107

TITLE:

Impact behaviour of stiffened aluminium plates

Oppførsel til avstivede platefelt i aluminium utsatt for støtlaster

BY:

Even Josten Lien and
Aleksander Skyrud

SUMMARY:

In this master thesis stiffened aluminium plates of the aluminium alloy AA6082 subjected to impact loading has been studied. The main objective was to study the behaviour of welded and stiffened aluminium plates exposed to impact loading from a ship, and determine how to model this in a large scale analysis. This master thesis was initiated in a cooperation between CASA at NTNU, Hydro Aluminium and SAPA, as a part of the project "*Ferry-free coastal route E39*". This project is a continuation of the master thesis that Bente Larsen Kårstad and Birgitte Skajaa wrote in 2015.

It was planned to conduct both material tests and quasi-static impact tests of the stiffened aluminium plates in the laboratory as part of this report. Due to problems in the production line, the components never arrived on time. After a discussion with our supervisors in mid-May, the laboratory tests were cancelled and it was decided to focus on the establishment and validation of numerical models to replicate the experiments that Hilde Giæver Hildrum carried through in her Dr.Ing- thesis, and to do a preliminary analysis of a different test setup with both T4- and T6-plates. A literature study on the behaviour and modelling of stiffened aluminium plates subjected to impact loading has also been conducted.

As a part of this thesis a numerical model in the finite element software *Abaqus* has been established in order to replicate the static tests that Hildrum carried through. The numerical models give acceptable estimations and captures the failure modes for all of the different test setups in a satisfactorily way. However, there are some aberrations in predictions of failure and the stiffness of the plate. The material model was simplified by implementing the isotropic von Mises yield criterion, in which case the great degree of anisotropy in the AA6082-T6 alloy was neglected. It was also decided to model the plate without a weld. This could explain some of the varying accuracy in the numerical simulations.

The numerical model in the preliminary analysis was conducted with two different heat treatments of the AA6082 alloy, namely T4 and T6. The difference between the behaviour of the plate with the two alloys is large, since different heat treatments yields different material properties and behaviour. For both the T4- and T6-plate, two different fracture criterions has been implemented, the Cockcroft-Latham (CL) fracture criterion and the Bressan-Williams-Hill (BWH) instability criterion. The numerical simulations show difference in both initiations of fracture and failure modes for the two criterions. Analyses run with BWH yields a better coherence between different mesh sizes than CL, and is also less computational expensive, which makes it more favourable in large scale analysis.

RESPONSIBLE TEACHER: Prof. Magnus Langseth

SUPERVISOR(S): Prof. Magnus Langseth and Associate Prof. David Morin

CARRIED OUT AT: CASA, Department of Structural Engineering

SAMMENDRAG PÅ NORSK:

I denne masteroppgaven har oppførselen til avstivede platefelt av aluminiumslegeringen AA6082 utsatt for støtlast blitt studert. Hovedmålet var å vurdere oppførselen til store platefelt i aluminium sveist sammen av ekstruderte profiler under støtlast fra skip, og hvordan disse skal modelleres i en storskala analyse. Denne masteroppgaven er en del av prosjektet *Ferjefri E39 og* et samarbeid mellom CASA ved NTNU, Hydro Aluminium og SAPA. Oppgaven er en fortsettelse av arbeidet som Bente Larsen Kårstad og Birgitte Skajaa gjorde i sin masteroppgave i 2015.

Det var i utgangspunktet planlagt å gjennomføre både materialtester og støtforsøk på avstivede platefelt i laboratoriet, men grunnet problemer i produksjonslinjen dukket ikke komponentene opp i tide. Etter samtaler med veileder, i midten av mai, ble det enighet om å kansellere laboratorietestene, og heller fokusere på etablering og validering av en numerisk modell for å gjenskape eksperimentene Hilde Giæver Hildrum gjorde i sin doktoroppgave, samt en innledende analyse på et nyere platefelt. Det har også blitt gjennomført et litteraturstudium knyttet til oppførsel og modellering av avstivede platefelt i aluminium utsatt for støtlaster.

Som en del av denne masteroppgaven har det blitt etablert numeriske modeller i elementmetodeprogrammet *Abaqus*, for å gjenskape noen av de eksperimentene Hildrum gjennomførte. De numeriske modellene gir akseptable estimater for de eksperimentelle resultatene. Bruddmønsteret i platen blir spesielt godt gjenskapt, for alle de ulike forsøkene. Det er dog noen avvik i de numeriske modellene når det kommer til stivheten til platefeltet og bruddkraft. Materialmodellen ble forenklet ved å implementere det isotropiske flytekriteriet von Mises, hvor de anisotrope egenskapene til AA6082-T6 blir neglisjert, samt at platen ble modellert uten sveis. Dette kan være en av grunnen til avvikene som finnes mellom forsøkene og de numeriske resultatene.

Den numeriske modellen i den innledende analysen ble gjennomført for to ulike varmebehandlinger for AA6082-legeringen, nemlig T4 og T6. Det er store forskjeller i oppførselen til platefeltet for de to ulike varmebehandlingene, da disse gir ulike materialegenskaper og oppførsel. Legeringer med T4 er generelt mer duktile enn T6, men har lavere styrke. For begge materialene har det blitt implementert to ulike bruddkriterium, Cockckroft-Latham (CL) bruddkriterium og Bressan-Williams-Hil (BWH) instabilitetskriterium. Analysen viser forskjell mellom de to kriteriene når det kommer til initiering av brudd samt bruddmønsteret. Analysene med BWH er mindre sensitive til endringer av elementstørrelser enn CL, samt at analysene har lavere beregningsmessig varighet, og vil dermed være noe mer effektiv i en storskala analyse.

Institutt for konstruksjonsteknikk
FAKULTETET FOR INGENIØRVITENSKAP OG TEKNOLOGI
NTNU – Norges teknisk naturvitenskapelige universitet

MASTEROPPGAVE 2016

for
Even Josten Lien og Aleksander Skyrud

Oppførsel til avstivede platefelt i aluminium utsatt for støtlaster

Impact behaviour of stiffened aluminium plates

Samferdselsdepartementet har bedt Statens vegvesen om å utrede hvilket potensiale en fergefri E39 vil ha for næringsliv og tilhørende bo- og arbeidsregioner. Prosjektet skal også vurdere teknologiske løsninger for fjordkryssinger, og hvordan konstruksjonene eventuelt kan utnyttes til å produsere energi fra sol, bølger, strøm og vind. I tillegg skal også gjennomførings- og kontraktstrategier inngå i prosjektet E39 går langs kysten fra Kristiansand til Trondheim, og er i dag ca. 1100 km lang. Også økonomiske vurderinger av fergefri E39 skal inngå, dvs. både kostander og gevinster.

Som et ledd i prosjektet fjordkrysninger så er det ønskelig å vurdere bruk av aluminium blant annet på grunn av reduserte vedlikeholdskostnader og lav vekt i forhold til styrke. En av utfordringene er å vurdere hvordan store platefelt i aluminium sveiset sammen av ekstruderte profiler oppfører seg under en støtlast fra t skip og hvordan disse skal modelleres i en storskala analyse. Denne masteroppgaven er et ledd i dette prosjektet og er et samarbeid mellom SIMLab ved NTNU, Hydro Aluminium og Sapa.

Følgende foreløpige plan er definert for denne oppgaven:

- Det skal gjennomføres et litteraturstudium knyttet til oppførsel og modellering av avstivede platefelt i aluminium og stål utsatt for støtlaster.
- Studentene skal delta i gjennomføring av forsøk i laboratoriet. I dette ligger støtforsøk på avstivede platefelt samt materialtester.
- Etablering av en numerisk modell samt validering basert på de tester som er utført.
- Parameterstudier og retningslinjer for modellering.
- Rapportering.

Veiledere: *Magnus Langseth og David Morin*

Kandidatene kan avvike fra den foreslåtte plan, men kun etter plan med veilederne. Hovedoppgaven skal skrives på engelsk og utformes som en forskningsrapport og i henhold til gjeldene regler for en hovedoppgave. Oppgaven skal leveres til Institutt for konstruksjonsteknikk, NTNU innen 14. juni 2016.

NTNU, 14. januar 2016

Magnus Langseth
Professor

Preface

This master´s thesis was written for Centre for Advanced Structural Analysis (CASA) hosted by Department of Structural Engineering, Norwegian University of Science and Technology (NTNU). The object of the work was to study the behaviour of stiffened aluminium plates in different loading situations in the low-velocity regime and how to model this in a large scale analysis using a finite element code. The extent of the work was 20 working weeks and 30 educational points.

We would like to thank our supervisors Professor Magnus Langseth and Associate Professor David Morin for their inspiring guidance and support during this semester. A special thank is also directed to PhD candidate Petter Henrik Holmstrøm, for answering to all kinds of strange questions throughout this period.

This thesis marks the end to five years of study at the Norwegian University of Science and Technology and it will hopefully reflect some of the knowledge that we have acquired over the years.

Table of Contents

Preface i

Table of Contents iii

List of Figures v

List of Tables vii

Abbreviations viii

Symbols ix

1. Introduction 1

1.1 Background 1

1.2 Definitions used in structural impact 2

1.2.1 Classification of target by thickness 2

1.2.2 Velocity definitions 2

1.2.3 Failure modes 3

1.3 Previous work 6

1.4 Objective and scope 9

1.5 Computer software 9

2. Theory 11

2.1 Aluminium alloys 11

2.2 Friction stir welding 13

2.3 Material mechanics 15

2.3.1 Definitions of stress and strain 15

2.3.2 Necking 16

2.4 Material modeling 19

2.4.1 Yield criterion 19

2.4.2 Flow rule 20

2.4.3 Work-hardening 21

2.4.4 Flow stress ratio, R-value 22

2.5 Fracture mechanics 25
2.5.1 General 25
2.5.3 Fracture criterion 27
2.6 Finite element method 34
2.6.1 Impact problems and motivation of using nonlinear theory 34
2.6.2 Explicit analysis 35
2.6.3 Quasi-static analysis 38
2.6.4 Plate theory 39
2.6.5 Shell elements 40

3. Dr ing. thesis of Hilde Giæver Hildrum 43
3.1 Experimental programme 43
3.2 Numerical modelling 45
3.3 Results and discussion 47

4. Preliminary analysis of T6- and T4-plates 55
4.1 Experimental program 55
4.2 Numerical simulations of T6-alloy 57
4.2.1 Model and material 57
4.2.2 Results and parametric study 60
4.3 Numerical simulations with the T4-alloy 69
4.3.1 Model and material 69
4.3.2 Results and parametric study 70
4.3.3 Comparison with T6-analysis by Kårstad and Skajaa 75

5. Conclusion and proposal to future work 77
5.1 Impact loading of plate with L-stiffeners 77
5.2 Impact loading of T4- and T6-plates 78

Appendices 81

References 89

List of Figures

Figure 1-1: Illustration of a floating (pontoon) bridge 1
Figure 1-2: Non-failure modes for thin plates 3
Figure 1-3: Different failure modes 4

Figure 2-1: FCC unit-cell 11
Figure 2-2: Stress-strain curve for AA6082 13
Figure 2-3: Friction stir welding principle and microstructure. 14
Figure 2-4: Two aluminium panels joined together with FSW 14
Figure 2-5: Typical engineering stress-strain curve for aluminium alloys 15
Figure 2-6: Necking criterions 17
Figure 2-7: Illustration of localized and diffuse necking in a bar 18
Figure 2-8: Illustraions of stages in a ductile fracture 25
Figure 2-9: Stress-strain curves comparing the effects of FSW 26
Figure 2-10: Forming limit diagrams. 29
Figure 2-11: BWH and shear instability. 31
Figure 2-12: Energy history output for a quasi-static analysis 38
Figure 2-13: Stresses and associated moments and transverse shear forces. 39
Figure 2-14: Load bearing by bending (out-of-plane) and membrane (in-plane) action 40
Figure 2-15: Shell element (S4R) in Abaqus 41

Figure 3-1: Experimental setup for the static tests 43
Figure 3-2: Plate geometry, loading positions and idealised boundary conditions 44
Figure 3-3: Snapshot of the replicated model with a hemispherical indenter 45
Figure 3-4: Geometry of indenters 46
Figure 3-5: Force-displacement curves for different setups 48
Figure 3-6: Deformation of the plate, with von Mises stress 49
Figure 3-7: Failure modes 50
Figure 3-8: Internal and kinetic energy history output 51
Figure 3-9: Mesh sensitivity. 51
Figure 3-10: Force-displacement curves with new material properties in the stiffener. 52
Figure 3-11: Force-displacement curves with different fracture criterions 53

Figure 4-1: Test rig for quasi-static experiments 55
Figure 4-2: Illustrations of plate and rig 56
Figure 4-3: Snapshot of the model used in Abaqus/Explicit 57
Figure 4-4: One quarter of the hemispherical indenter 57
Figure 4-5: Deformation of the plate during the simulations 60
Figure 4-6: Force-displacement curves and displacement at failure (CL criterion) 62
Figure 4-7: Force-displacement curves for different fracture criterions 63
Figure 4-8: Failure modes for different fracture criterion 64
Figure 4-9: Mesh sensitivity for BWH 65

Figure 4-10: FLDs for different materials ... 66
Figure 4-11: Force-displacement curves for different frictions coefficients ... 66
Figure 4-12: Force-displacement curve for different hardening rules ... 67
Figure 4-13: Stress-strain curves for different hardening rules ... 68
Figure 4-14: Equivalent plastic strain and von Mises stress before fracture ... 68
Figure 4-15: Abaqus model used in the analysis of the T4-alloy ... 69
Figure 4-16: Displacement for T4-plate during the simulations ... 70
Figure 4-17: Force-displacement curves for different mesh sizes and fracture criterion ... 72
Figure 4-18: Failure in plate with BWH for different directions ... 73
Figure 4-19: Force-displacement curves for different fracture criterions ... 73
Figure 4-20: Force-displacement curves for different friction coefficients between: ... 74
Figure 4-21: Force-displacement curves for T4 and T6 ... 75
Figure 4-22: Deformation of T4-plate under transversal loading ... 76

Figure 5-1: Comparison between different setups ... 79

List of Tables

Table 2-1: Chemical composition of the AA6082 aluminium alloy 12
Table 2-2: Hardening rules and their parameters 22
Table 2-3: Test results AA6082-T6: R-ratios and flow-stress ratios 23

Table 3-1: Key values for AA6082-T6 46
Table 3-2: Comparison for aluminium plates with L-stiffeners 47

Table 4-1: Key values from the material card for AA6082-T6 58
Table 4-2: Material properties for S355 steel and 12.9 steel bolts 59
Table 4-3: Computational time for different mesh sizes and fracture criterions 61
Table 4-4: Key values from the material card, estimated with Voce rule 67
Table 4-5: Key values for AA6082-T4 69
Table 4-6: Computational time for different mesh size and fracture criterions 71

Abbreviations

BWH	Bressan-Williams-Hill
CL	Cockcroft-Latham
CPU	Central Processing Unit
DOF	Degrees of Freedom
FCC	Face-Centered Cubic
FEA	Finite Element Analysis
FEM	Finite Element Method
FLD	Forming Limit Diagram
FSW	Friction Stir Welding
HAZ	Heated Affected Zone
MIG	Metal Inert Gas
MDOF	Multi Degree of Freedom
NFEA	Nonlinear Finite Element Analysis
NFEM	Nonlinear Finite Element Method
NPRA	Norwegian Public Road Administration
TMAZ	Thermo-Mechanically affected zone

Symbols

A	current cross-sectional area
A_0	initial cross-sectional area
c_d	dilatational wave speed of element
$\boldsymbol{c}_k$	curvature vector
$\boldsymbol{C}$	isotropic material matrix
C_R	hardening parameter (voce rule)
dT_1	traction increment
D	flexural rigidity for plate
$\mathcal{D}\rho$	plastic dissipation per unit volume
E	young’s modulus, E-modulus
E_I	internal energy
E_V	viscous energy
E_F	frictional energy
E_W	external work energy
E_{total}	sum of the energy components
f	yield function
F_i	force (arbitrary)
F_su	force at fracture
g	plastic potential function
h_R	hardening modulus
J_2	second invariant
K	hardening parameter (power law)
L_e	characteristic length of element
$\tilde{n},\ n$	hardening parameter (power law)
Q_R	hardening parameter (voce rule)
R	isotropic hardening variable
R_α	ratio of plastic strains, R-ratio
r_α	ratio of flow-stress, r-ratio
t	thickness
t_e	element thickness
Δt	stable time increment
Δt_{cr}	critical stable time increment
V	shear force
w	displacement in vertical direction
W	measure for energy per unit volume
W^p	specific plastic work
Δt_{cr}	cockcroft-latham parameter

α	ratio between minor and major principle stress
β	ratio between minor and major principle strain
γ	shear deformation
$\boldsymbol{\varepsilon}$	strain tensor
$\mathrm{\varepsilon}$	true strain
ε_e	engineering strain
$\bar{\varepsilon}$	equivalent strain
$\varepsilon_1, \varepsilon_2, \varepsilon_3$	principal strains
ε_f	fracture strain
$\dot{\mathrm{\varepsilon}}$	strain rate (increment)
ε^e	elastic strain
ε^p, p	plastic strain
ε_l^p	plastic strain in length direction
ε_t^p	plastic strain in thickness direction
ε_w^p	plastic strain in width direction
$\dot{\lambda}$	plastic multiplier
$\mathrm{\xi}$	damping ratio
$\boldsymbol{\sigma}$	stress tensor
$\mathrm{\sigma}$	true stress
σ_e	engineering stress
$\bar{\sigma}$	equivalent stress
$\sigma_1, \sigma_2, \sigma_3$	principal stresses
σ_Y	yield stress
σ^*	peak stress
τ_{cr}	critical shear stress
$\mathrm{\varphi}$	magnitude of the stress state
ν	Poisson´s ratio
ω_{max}	highest (maximum) natural frequency

1. Introduction

1.1 Background

Route E39 is the main highway in the western part of Norway. The road is approximately 1100 km long and it connects Kristiansand in the south with Trondheim in the central part of Norway. As of 2016 the total travel time is somewhere around 21 hours, which include a total of eight ferry connections.

In 2010 the Ministry of Transport and Communications in Norway gave the Norwegian Public Road Administration (NPRA) commission to do initial studies on the impacts of a ferry-free E39. The project is still on-going and split into four groups [1]:

- Planning, implementing of strategies and choice of contract forms.
- Study of social impacts, i.e. impacts on economy, employment, trade and settlement.
- Technological development of fjord crossings.
- Possible solutions and utilization of renewable energy.

Figure 1-1: Illustration of a floating (pontoon) bridge (NPRA, 2012)

Ships and boats are passing through the fjords on a regular basis, which implies that possible collisions and damages to the structures have to be accounted for. Because of this, it is desirable to study how welded, extruded aluminium profiles behave when they are subjected to impact loads, e.g. when a ship collides with a bridge.

Aluminium has a high strength to weight ratio and the maintenance and service costs are considerably low compared to other building materials. Bearing in mind that a lot of the aluminium alloys also show great corrosion resistance, will make them even more suitable for these kinds of structures.

1.2 Definitions used in structural impact

The study of impact phenomena, the collision of two or more solid bodies, involves a variety of complex problems. A complete treatment of the impact response of materials and structures would demand a considerably amount of work, hence are only the most fundamental parts of the impact theory presented in this section.

1.2.1 Classification of target by thickness

In addition to the complex treatment of an impact, it is several ways to characterize this phenomenon, e.g. according to impact angle, geometric and material characteristics or striking velocity. According to Backman and Goldsmith [2], a convenient way to classify impacts is by the thickness of the target, i.e. any moving or stationary object struck by a projectile.

1) *Semi-infinite*: no influence of the distal boundary of the target element.
2) *Thick*: influence of the distal boundary on the penetration process only after substantial travel into the target.
3) *Intermediate*: the rear surface exerts considerable influence on the deformation process.
4) *Thin*: the stress and deformations gradients throughout the thickness of the target do not exist.

1.2.2 Velocity definitions

The most fundamental consideration in impact mechanics is the velocity and it may be so dominant that it will override most other effects. Therefore, it is common to distinguish between different velocity regimes [2]:

1) *Low velocity regime (0-50 m/s)*: deformation controlled by elastic and plastic bending.
2) *Sub-ordnance velocity regime* (50-500 m/s): projectiles will normally behave in an elastic manner, while the response in the target is primarily plastic.
3) *Ordnance velocity regime (500-1300 m/s*): most of the kinetic energy is converted into plastic work in both the indenter and the target.
4) *Ultra-ordnance velocity regime (1300-3000 m/s):* the materials will behave like fluids, i.e. a hydrodynamic description is necessary.
5) *Hypervelocity regime (>3000 m/s):* material strength is no longer important, because the projectile often will be completely eroded during impact.

The low velocity regime will cover a ship crashing into an aluminium structure; thus, this thesis will only deal with impact in this regime. When the mass of an indenter, with velocity within this regime, increase, the response is essentially plastic membrane stretching and bending. A considerable plate deflection that extends to the supports is also expected to occur [3].

1.2.3 Failure modes

It is common to dived target response into non-failure and failure modes.
Characteristic for non-failure modes of thin plate elements is elastic deformation with no damage, and two types of transverse displacement due to plastic deformation.
One in the contact zone, called bulging, that indicates that the target deforms to the shape of the projectile, and dishing, induced by bending, who may extend to considerable distance from the impact area [2]. See Figure 1-2.

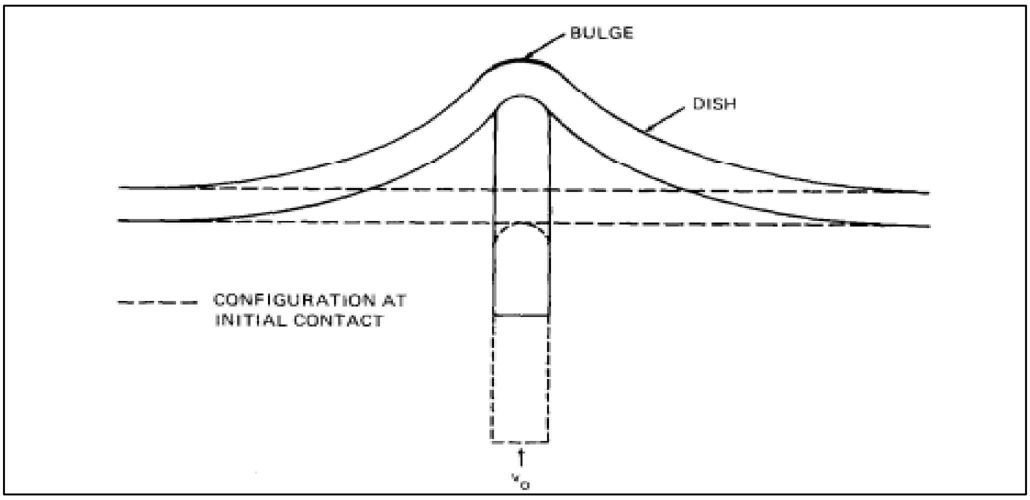

Figure 1-2: Non-failure modes for thin plates (Backman and Goldsmith, 1978)

Failure modes for thin plates depend on variables such as material properties, impact velocity, projectile nose shape and angle, geometry of target and support conditions. Some of the most common failure modes are illustrated in Figure 1-3. In most cases, one of these will dominate the failure development, but several mechanics may interact. The most relevant failure modes for this master thesis are described below. For a more comprehensive description, please refer to [2], [4] or [5].

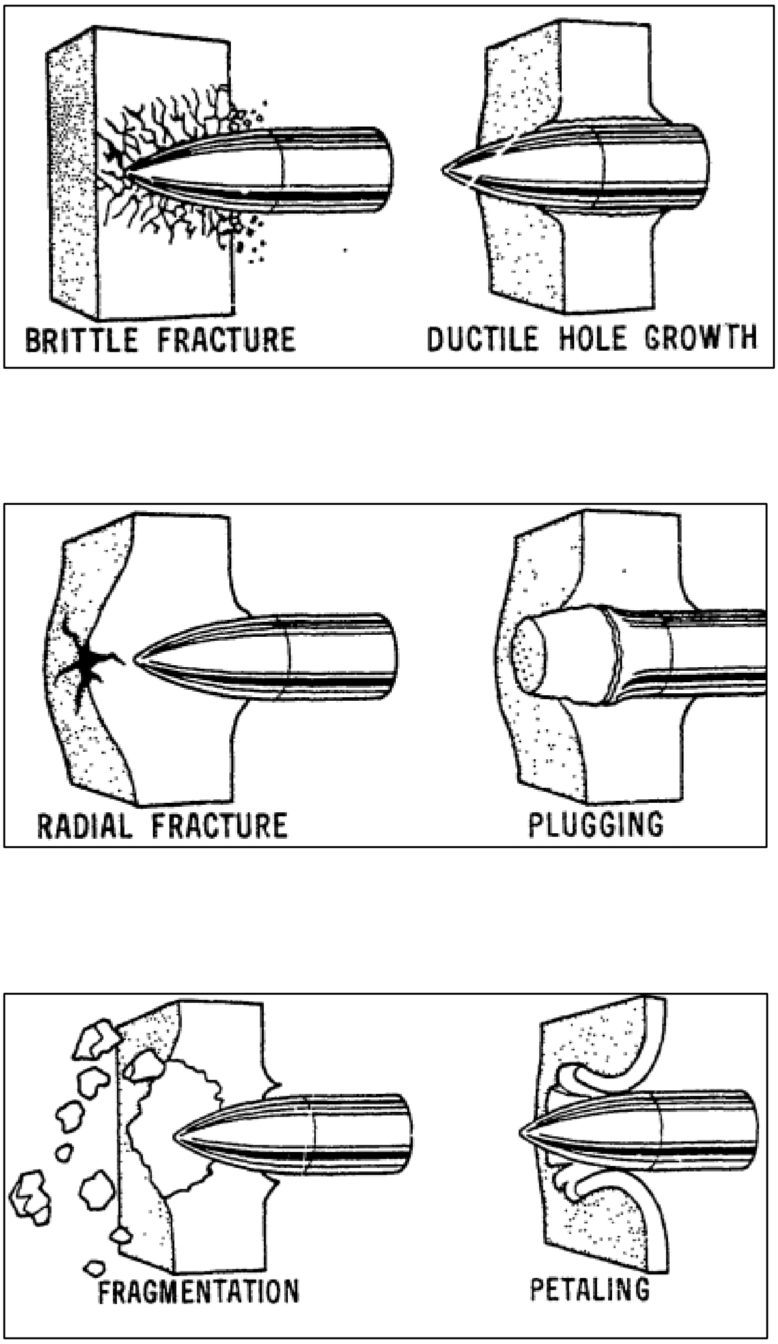

Figure 1-3: Different failure modes (Zukas, 1980)

Plugging

Failure due to plugging is most frequently observed in thin or intermediate thick targets, struck by a blunt or hemispherical nosed indenter. The moving indenter creates a nearly cylindrical plug in the target material, with approximately the same diameter as the nose. The shape of the plug depends on the triaxial stress situation, i.e. shear in combination with membrane and bending stresses in the target material. The separation of the plug from the target creates large shear forces, which generates heat. A rise in temperature leads to additional plastic flow and decreasing material strength, resulting in an instability. This is called an adiabatic shearing process [2].

Petaling

Petaling fracture is also common in thin plates impacted by a blunt projectile at relatively low velocities. As the indenter pushes the target material forwards, large bending moments create the characteristic deformation pattern, as illustrated in Figure 1-3. This effect is produced by high radial and circumferential stresses after passage of the initial stress wave [4]. Petaling is accompanied by large plastic flow and/or permanent flexure, which eventually will result in that the tensile strength of the plate material is exceeded, and a star-shaped crack develops around the tip of the indenter.

1.3 Previous work

In this section a brief summary of relevant work and literature will be given as part of the literature study on stiffened plates. Note that more theory and research work will be discussed throughout this report and references will be made where we find them appropriate

There exists various literature governing plates that are subjected to impact loading. The first comprehensive testing of penetration of projectiles and study of impact mechanics were carried out in the 1970s. Backman and Goldsmith [2] did tests that concerned all sorts of impact on thin to thick targets with both small and large projectiles in all velocity regimes. However, most of the experimental data covers small projectiles travelling with high velocities. This section will emphasize on impacts in the low velocity regime.

Langseth and Larsen [5], [6] did extensive numerical and experimental studies on single steel plates and stiffened steel plates subjected to large mass projectiles in the low velocity regime. Two distinct phases were observed in the force-time curves: In the transient phase, inertia forces are the only forces present and no forces are transmitted to the supports. Short after, the supports are fully activated and the impact can be considered as quasi-static. This is called the global mode phase. A comparison between the dynamic and the static tests indicated that the force-displacement curves had approximately the same slope in the global mode phase, which explains why the impact can be idealized as quasi-static when the supports are activated. The structural response was described by global plastic deformations of the plates with the possibility of plugging at impact point. The results showed that the critical impact energy increased with the plate thickness and decreased with the in-plane panel stiffness. An increase in the mass of the projectile resulted in a drop of the critical impact energy, which eventually seemed to approach the static plugging energy when the mass reached a certain value.

An experimental study of the plugging capacity of aluminium plates in alloy AA5083-H112 and AA6082-T6 was carried out by Langseth and Larsen in 1994 [7]. Similar to the tests on steel plates, the impact could be divided into a transient phase and a global mode phase. Based on the same height of drop, the weight saving of using aluminium alloy instead of steel was approximately 35% and 12% for alloy AA5083-H112 and AA6082-T6, respectively. The variation between the alloys was described by the difference in yield stress.

Langseth et al. [8] did validation of numerical simulations by performing impact tests on steel and aluminium plates in the low-velocity regime. The results showed that the response of the plates were mainly controlled by plastic membrane stresses, which indicated that the interface force curves were strongly influenced by the shape and the magnitude of the input stress-strain curve. The simulations were performed with the computer code LS-DYNA and good agreement was found for steel plates by using quasi-static material properties and shell elements in the analysis. The reason is that about 90 – 95 % of the initial kinetic energy of the projectile is absorbed as strain energy in the plate and that only a small fraction is spent to create a plug. As plugging always takes place at maximum force, they suggested that an analysis with shell elements is useful provided that the critical interface force is known.

Wang et al. [9] did impact studies on double hull structures made of steel. In order to replicate different collision scenarios, nine independent tests were carried out with different indenters. The test results revealed that the nose radius and location of penetration had a very strong influence on the behaviour and resistance of the double hull: the structure showed much higher capacity when the spherical indenter were blunt (larger radius) instead of sharp.

Hilde Giæver Hildrum [10] wrote her Dr.-Ing thesis on stiffened aluminium plates subjected to large mass projectiles in the low velocity regime. The plates were fabricated from AA6082-T6 aluminium alloy extrusions joined together with metal inert gas (MIG) welds to form flat stiffened plates. The impact testing was performed with various nose shapes (blunt and hemispherical) and different load applications (between, on and next to a stiffener). Results from the experiments showed that the estimated incipient fracture velocity was significant lower for the hemispherical indenter than the blunt ended indenter. This coincides well with the results presented by Wang et al. [9]. Two different failure modes were also observed: The blunt projectile caused failure by plugging, while petaling failure modes were observed for the hemispherical projectile. Loading on the weld between the stiffeners yielded the lowest incipient fracture velocity, while loading on the stiffener gave the highest. In addition to impact tests, static punch tests were carried out to study any relationship between dynamic and quasi-static capacities before fracture occurs. In the given velocity range, the results indicated that the static tests of the blunt ended projectile may give a conservative estimate of the incipient fracture impact energy in the dynamic tests, while the static tests for the hemispherical ended projectile may lead to non-conservative results.

Liu et al. [11] presented a simplified analytical method to examine the energy absorbing mechanisms of small-scaled stiffened steel plates, quasi-statically punched at the mid-span by a rigid indenter. The proposed method, validated with the experimental and the numerical results, derives expressions to estimate the relation between the plastic deformation and the energy dissipation. Both the plate and the stiffeners dissipate the incident energy through the membrane plastic tension of the structural elongation and the rotation of plastic hinges at the applied load and the supports. The tripping and folding of the stiffeners decreases the energy dissipation, and the stress concentration and material fracture makes the plate absorb more energy. The results indicate that the geometry of the indenter strongly influences the plastic deformation and failure mechanisms of the plates. In general, the critical deflection and energy increased with the indenter's width, mainly due to the fact that a wider contact area decreases the stress concentration, and consequently delayed the crack initiation. A longer indenter allows for more structural elements to participate in the deformation and more energy is absorbed.

This report is a continuation of the master thesis written by Bente Larsen Kårstad and Birgitte Skajaa [12]. Their main objective was to study the impact behaviour of extruded aluminium profiles joined together with friction stir welds (FSW) and how to model this in a large scale analysis. They did both quasi-static and dynamic impact tests between the welds on stiffened plates of the aluminium alloy AA6082-T6. The results showed that a quasi-static test gives satisfying validation for this particular alloy, for the cylindrical indenter in both the transverse and the longitudinal direction. In the material tests a large degree of anisotropy was detected for the alloy, as well as a large difference in the material properties for the plates, stiffeners and the welds. Since their material implementation included an isotropic yield criterion, they suggested that an anisotropic yield criterion may give more accurate results in future simulations. The experiments were simulated using conventional shell elements in a nonlinear element analysis in Abaqus/Explicit. The experimental and numerical results were compared and the model was validated.

Two different fracture criterions were implemented and compared: Cockcroft-Latham (CL) fracture criterion and Bressan-Williams-Hill (BWH) instability criterion. Both gave acceptable estimates in terms of initiation of fracture, but the CL-criterion showed a higher degree of mesh sensitivity and a mesh size equal to the thickness of the plate was necessary to obtain acceptable results.

1.4 Objective and scope

This master thesis was established as part of the "*Ferry-free coastal route E39*"-project as a cooperation between CASA at NTNU, Hydro Aluminium and Sapa. The main objective was to study the behaviour of welded and stiffened aluminium plates exposed to impact loading from a ship and determine how to model this in a large scale analysis.

The main tasks of the project were as following:

- A literature study on the behaviour and modelling of stiffened aluminium and steel plates subjected to impact loading.
- Conduct material tests of the aluminum alloys AA6082-T4 and AA6082-T6 in the laboratory to study the material properties.
- Conduct tests of the components in the laboratory, i.e. quasi-static impact loading of the aluminum plates, with focus on different loading positions.
- Establish a numerical model in Abaqus/Explicit and validate the model.
- Conduct a parametric study on our model and present guidelines on how to make and use these in large scale analysis.

The aluminium plates were supposed to be delivered to the test facility in middle of the semester, but due to problems in the production line, the components never arrived on time. After a discussion with our supervisors mid-May, the laboratory tests were cancelled and it was decided to focus on the establishment of a numerical model to replicate the experiments by Hildrum and to do a preliminary analysis of the T4- and T6- plates.

1.5 Computer software

A central part of this project is to establish numerical models to replicate the experiments that have been carried out in the laboratory. The numerical simulations in this thesis are completed using the finite element analysis (FEA) software Abaqus, which is a general purpose finite element method (FEM) system operated by Dassault Systèmes. PlotDigitizer has been used to digitize scanned data plots. General data processing is performed in MATLAB. Relevant codes will be presented in the appendices.

2. Theory

2.1 Aluminium alloys

Pure aluminium is a relatively soft, ductile and light material. It is the most abundant metal in the Earth's crust, but it does not exist as a free metal in the nature due to its reactive behaviour. Commercially, the most common and efficient way to produce aluminum is through electrolysis of alumina (aluminium oxide) that are extracted from bauxite. The reduction of alumina into aluminium through electrolysis is an energy-intensive process. It takes roughly 14 kWh to produce 1 kilogram of aluminium, but only 5% of the initial energy input is necessary to recycle the material [13].

Aluminium is a polycrystalline material with a face-centered cubic (fcc) crystal structure. In a polycrystalline aggregate the individual grains have a crystallographic orientation different from those of its neighbours, which explains some of the anisotropy in the material [14]. Most extruded aluminium profiles possesses crystallographic texture that leads to anisotropy in its strength, plastic flow and ductility. The exact nature of the anisotropy depends upon both alloy composition and process history.

Because aluminium alloys offers a high strength-to-weight ratio and high degree of ductility, the potential areas of application are vast. The ability to withstand plastic deformation is particularly interesting in cases where impact loading is relevant. In order to understand why aluminium is a ductile metal, a study of the crystal structure is necessary. Irreversible deformation happens within a slip system, which is a generic term for slip plane and slip direction in the lattice. The fcc crystal structure have 12 slip systems all together and because extensive plastic deformation is possible in all these systems, aluminium is said to be ductile [15].

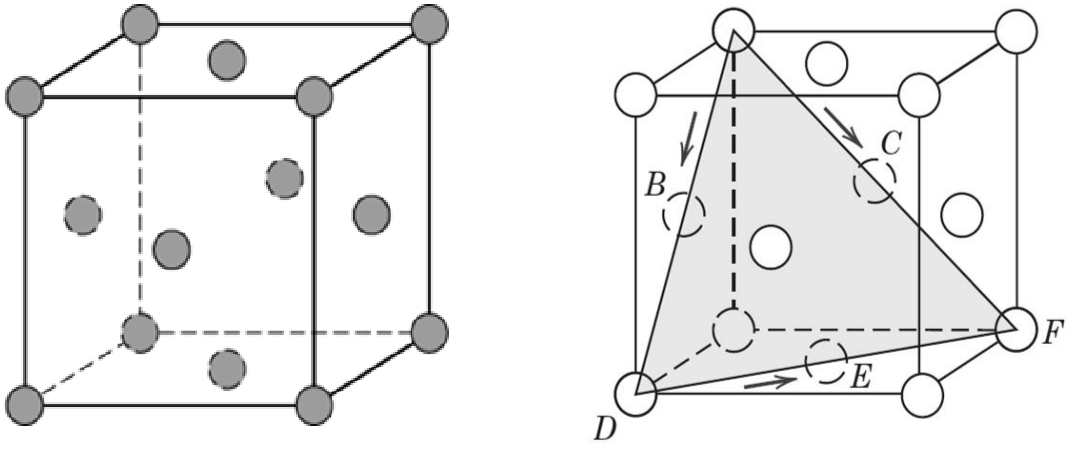

(a) (b)

Figure 2-1: (a) An fcc unit cell and (b) A slip system shown within an fcc unit cell.

(Callister, 2007)

Aluminium alloys are produced by adding chemical elements to the metal in order to cultivate certain characteristics and properties in the material. The particular aluminium alloy studied in this thesis is AA6082, with both Temper 4 (T4) and Temper 6 (T6).
The main alloying elements in AA6082 are magnesium and silicon, while the minor allying elements are manganese, iron, copper, chromium, zinc and titanium. Alloys belonging to the 6xxx series are also called Al-Mg-Si alloys. The nominal chemical composition is presented in Table 2-1.

Table 2-1: Chemical composition of the AA6082 aluminium alloy (Sapa, 2015)

Element	*wt%*
Si	0.70 – 1.30
Fe	< 0.50
Cu	< 0.10
Mn	0.40 – 1.00
Mg	0.60 – 1.20
Cr	< 0.25
Zn	< 0.20
Ti	< 0.10
Others	0.05 – 0.15
Al	Remainder

Good combination of strength, formability, corrosion resistance and weldability results in a vast variety of applications for the 6xxx series [16]. The alloy used in this thesis is a typical structural alloy and is often used in energy-absorbing structures. Because of the good formability and machinability, the AA6082 alloy is suitable for the extrusion process and can therefore be produced in large volumes. Extrusion processing is a dynamic forming process where mechanical working, friction and heat transfer can continuously evolve during the shaping process. Hence, control of the extrusion parameters, coupled with alloying, can be used to optimize the grain structure of the extruded aluminium components.

Heat treatment is one method used to improve or adjust the mechanical and physical properties of an aluminium alloy. The thermal history of the aluminium profile has an important impact on the strength of the material. The particular heat treatments used in this thesis are called T4 and T6, and both are in accordance with the temper designations in EN 515:1993 [17].

The heat treatment of an aluminium alloy is usually comprised in three steps [18]:

1. *Solution heat treatment*: Heating of the alloy so that all the constituents are into solid solution, i.e. a single phase.
2. *Quenching*: A rapid cooling-process to create a supersaturated solid solution.
3. *Ageing:* Hardening is achieved at room temperature (natural ageing) for the T4-alloy, while the T6-alloy is reheated (artificial ageing) in order to obtain more efficient formations of hardening precipitates.

The effects of precipitation on mechanical properties are greatly accelerated when the quenched material is reheated to 110-200^{o}C, which hardens the material quicker than natural ageing and to a greater level. Consequently, the T6-alloy will have higher strength than a T4-alloy. The downside of artificial ageing is that some of the original ductility in the material is lost, which means that T4-treated alloys allow for more plastic deformation than T6-alloys. Bear in mind that since hardening is obtained at room temperature for T4-alloy, it is not in a fully stable condition and some of the material properties may change over time.

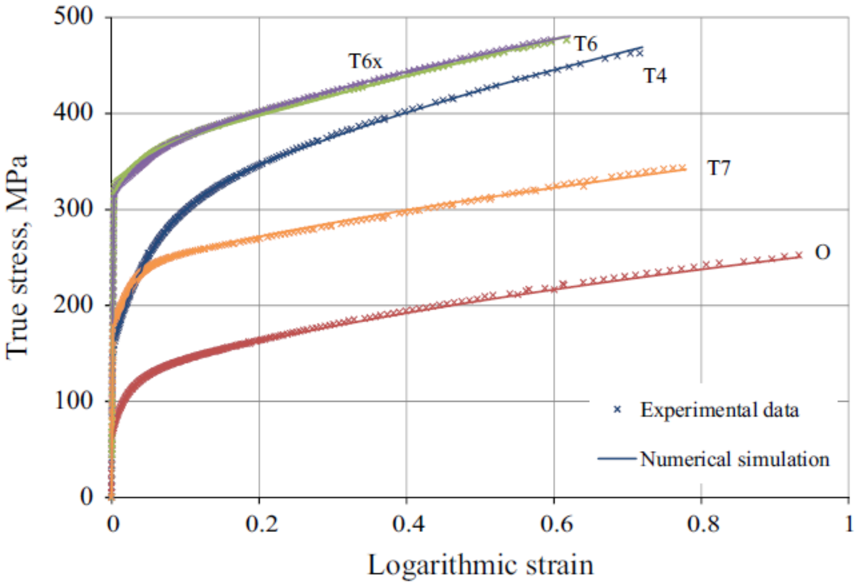

Figure 2-2: Stress-strain curve for AA6082 (Khadyko et al., 2013)

When extruded aluminium profiles are joined through welding, some softening of the material should be expected and as a result, reduced strength zones will arise. In general, the size of the softened zone in weldment is dependent on the welding parameters and material thickness [19]. This will be further discussed in the next section.

2.2 Friction stir welding

Friction stir welding (FSW) is a relatively new solid-state joining process, invented at TWI in Cambridge, in 1991. In particular, it is used to join sheet and plate materials such as aluminum, copper and lead. The joining process uses a non-consumable rotating tool, that moves along the joint between the two plates, producing heat and plastic deformations of the material. The heat causes the material to soften, without reaching the melting point, which allows the rotating tool to move along the joint, creating a solid phase bond between the two pieces, i.e. the plates are stirred together [20]. The plastic deformation results in generation of fine and recrystallized grains, which provide good mechanical properties.

Beside the good mechanical properties, and the fact that the loss in mechanical properties are low, due to the low heat input, FSW has a lot of advantages compared to other joining techniques. Because it is a solid-state process, problems like cracking and porosity will not restrict the capacity of the weld. Experiences from earlier studies show that shrinkage, distortion and residual stresses are very small as well [21]. The process is also environmentally friendly, since there is no emission of gas or dust, and FSW is considerably less energy-consuming compared to other welding techniques.

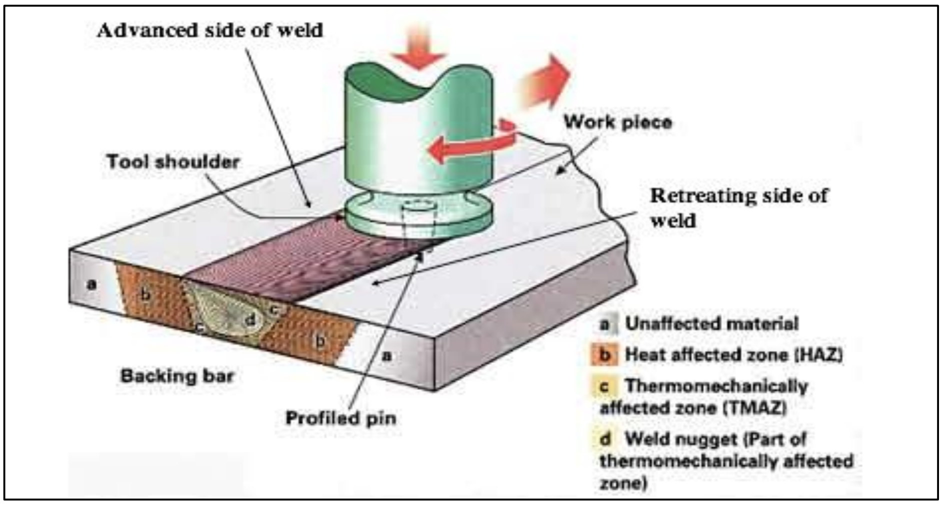

Figure 2-3: Friction stir welding principle and microstructure (Kallee et al., 2001).

The area around a friction stir weld can be divided into four different regions, based on the microstructure and how much the welding process affects them (see Figure 2-3). In the unaffected zone, the material is remote from the weld, and although it may have experienced some thermal effects, the microstructure remains unaffected. The aluminum in the heat affected zone (HAZ) has experienced a thermal cycle which has modified the microstructure, but there has not occurred any plastic deformation. The material in this area may therefore experience some changes in the mechanical properties. The region that extends to the width of the tool shoulder is called the thermo-mechanically affected zone (TMAZ). Here is the aluminum influenced by both plastic deformation and heat that may lead to significant plastic strain without recrystallization, because aluminum can be deformed at high temperatures without recrystallization, as opposed to other materials. The recrystallized area in the TMAZ in aluminum alloys is often called weld nugget, and this area has significantly lower hardness than the base alloy [20].

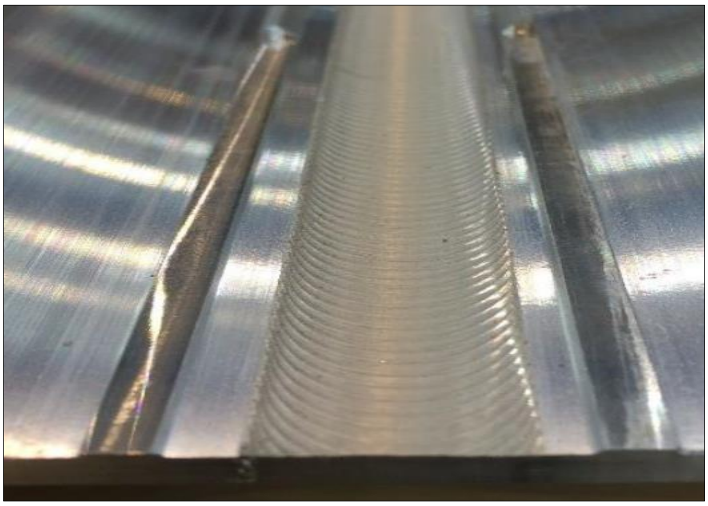

Figure 2-4: Two aluminium panels joined together with FSW (Kårstad and Skajaa, 2015)

2.3 Material mechanics

We know from basic solid mechanics that materials can deform when they are subjected to an external load. In order to understand and explain how materials deform, we need to know what stresses and strains are. Basic definitions of stress and strain will be given in this chapter. The necking phenomenon will also be discussed. The theory presented in this section is collected from the book by Ashby & Jones [22].

2.3.1 Definitions of stress and strain

Consider a uniform rod with initial gauge length L_0 and initial cross-section area A_0. By applying an external tensile load F to the rod, the material will deform and a change in the gauge length, ΔL, will be observed. Now assume that the force is being distributed uniformly over the cross-sectional area. This gives the following definition of the engineering strain ε_e and engineering stress σ_e:

$$\varepsilon_e = \frac{\Delta L}{L_0} = \frac{L - L_0}{L_0} = \frac{L}{L_0} - 1 \tag{2-1}$$

$$\sigma_e = \frac{F}{A_0} \tag{2-2}$$

Note that equations presented above are valid for small deformations only and that they represent the average values in the elastic domain. As long at the load-deformation relationship is linear, the stress-strain relationship remains proportional. This relationship is known as Hooke's law and can be expressed in the following way:

$$\sigma_e = E\varepsilon_e \tag{2-3}$$

where E is the Young's modulus (or E modulus), which represents the slope in linear part of the stress-strain curve. It is also a measure of the stiffness of a solid material.

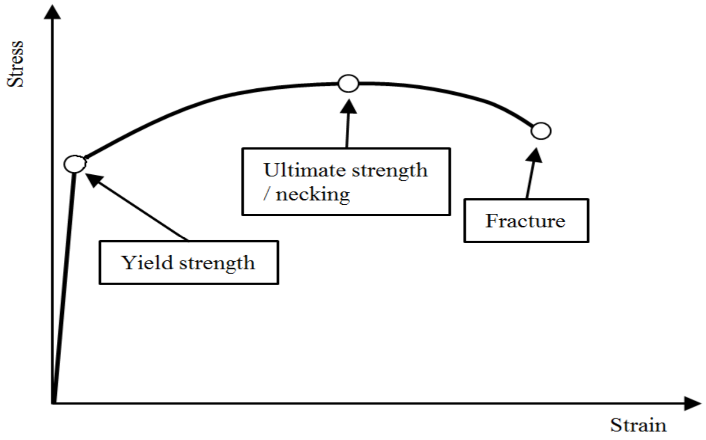

Figure 2-5: Typical engineering stress-strain curve for aluminium alloys (Ashby & Jones, 2012)

For metals and alloys the elastic strain is rather small (in the order 0.001 to 0.01) and the engineering formulations above remain valid. As the stress and strain increases and the deformation becomes rather large, we observe a permanent deformation of the material. This means that we have moved from the elastic domain and into the plastic domain where the material has a non-linear plastic behaviour and Hooke's law no longer is valid.

In order to allow for larger (finite) deformations, new definitions of strain and stress are introduced. These values are based on the current configuration of the material. By assuming that the plastic deformation is volume preserving, which is valid for most metals, we have the relation:

$$A_0 L_0 = AL \tag{2-4}$$

where A and L represent the current cross-sectional area and length, respectively. Thus, by using Equation (2-1), (2-2) and (2-4), the true (logarithmic) strain ε and the true (Cauchy) stress σ can be expressed as:

$$\varepsilon = \int_{L_0}^{L} \frac{dL}{L} = \ln\left(\frac{L}{L_0}\right) = \ln(1 + \varepsilon_e) \tag{2-5}$$

$$\sigma = \frac{F}{A} = \frac{F}{A_0}\frac{L}{L_0} = \sigma_e\left(\frac{L}{L_0}\right) = \sigma_e(1 + \varepsilon_e) \tag{2-6}$$

Most of the commercial finite element software today are based on the true definitions of stress and strain, which make these two equations important if it is desirable to introduce data from conventional tensile test that are based on the initial geometry of the specimen.

2.3.2 Necking

Necking is a phenomenon caused by plastic instability in the material. Let us for simplicity consider the same uniform rod as in section 2.3.1. As the tensile force increases, and thus the engineering stress, the rod will eventually reach its maximum force and the specimen will start to neck down. That means that somewhere along the rod, the cross-sectional area will start to decrease and in order to balance the external load, the stresses in that particular spot have to increase. See Figure 2-6 (a). The reduced cross-section is able to carry the extra stress due to work-hardening of the material. The rapidly decrease of the area with increasing elongation is called diffuse necking.

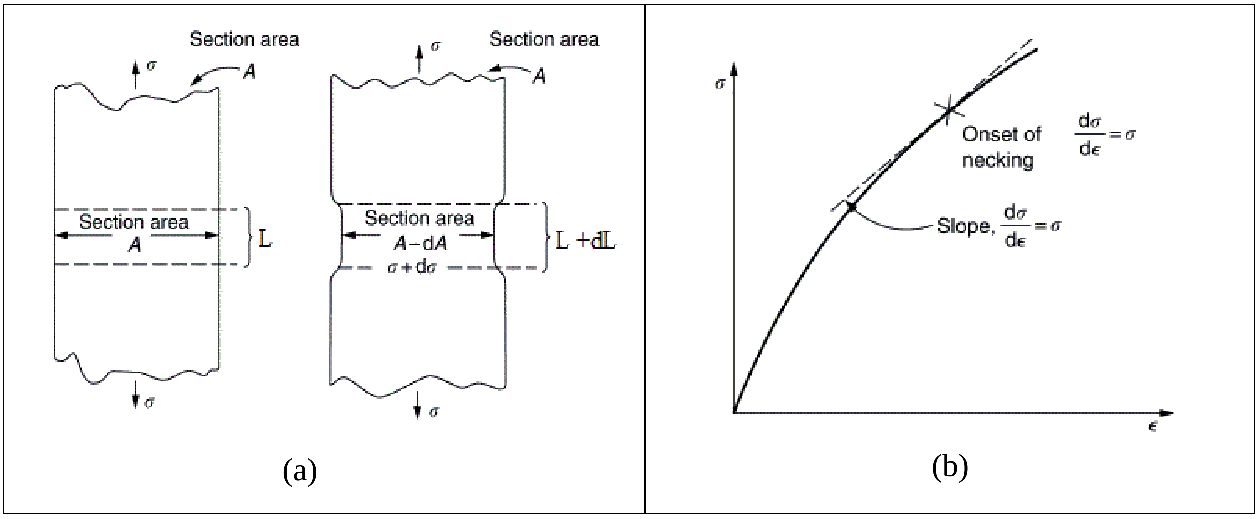

(a)

(b)

Figure 2-6: (a) Reduction of cross-sectional area somewhere along the specimen (b) The condition for necking shown in a true stress-strain curve (Ashby & Jones, 2012)

By combining (2-5) and (2-6), the engineering stress can be expressed as:

$$\sigma_e = \sigma \exp(-\varepsilon) \tag{2-7}$$

Plastic instability occurs at maximum tensile load, which is the same as saying that the incremental change of the engineering stress is equal to zero, that is $d\sigma_e = 0$. Thus, the diffuse necking criterion can be expressed the following way:

$$\frac{d\sigma}{d\varepsilon} = \sigma \tag{2-8}$$

At this point, the strain hardening can no longer keep up with increasing stress and the cross-section becomes unstable and a neck forms somewhere along the specimen. At some point, the accumulation of stress in the neck can no longer be accommodated for and fracture occurs. The diffuse necking marks the end of the useful part of a tensile test [23].

In a uniaxial tensile test of a rod, a diffuse neck will introduce a complex triaxial state of stress in the given region. Because of the local contraction in both the width and thickness directions, a raise of the longitudinal stress is required to cause plastic flow. Necking in a cylindrical specimen is symmetrical if the material is isotropic.

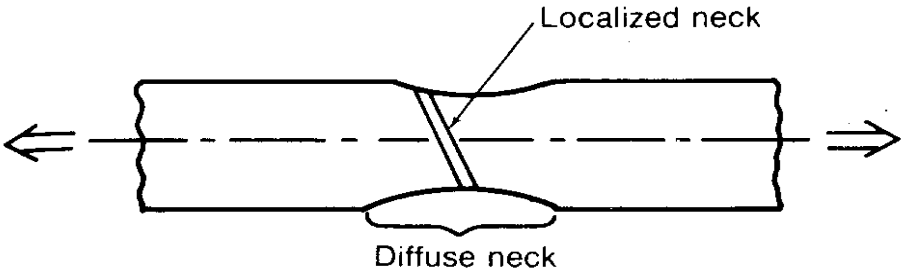

Figure 2-7: Illustration of localized and diffuse necking in a bar (Dieter, 1986)

A different type of necking is found for tensile specimen with rectangular cross-section (e.g. plates) that is cut from a sheet [24]. Because the width of the specimen is much greater than the thickness, there exists two types of plastic instabilities in tension. The first is diffuse necking, as discussed above. This instability may terminate in fracture, but it is often followed by a second instability called localized necking. Localized necking is caused by a narrow band with a width about equal to the sheet thickness, across the width of the specimen. Since only the thickness direction is localized, the neck develops gradually and considerable extension is possible after the onset of necking.

2.4 Material modeling

2.4.1 Yield criterion

As emphasized in Section 2.3.1, most metals in uniaxial tension show a linear elastic behaviour as long as the strain remains small, while a non-linear behaviour is typical for larger strains. An important consideration in the field of plasticity is deducing mathematical relationships in order to predict and describe when a material yields, i.e. when the material no longer has a proportional stress-strain relationship. In uniaxial tension testing, the proportional limit or yield limit (denoted σ_0), is defined as the value of stress necessary to initiate plastic flow which allow the material to deform plastically [24]. The transition between the elastic and plastic domain may be abrupt or more gradual, depending on the actual material. Most aluminium alloys and high-strength steel materials show a gradual transition [23].

Mathematically the yield limit can be described by a yield criterion. Let f be the continuous yield function of the stress tensor $\boldsymbol{\sigma}$. By definition, we have the following conditions:

$$\begin{aligned} f(\boldsymbol{\sigma}) < 0: &\quad \textit{elastic domain} \\ f(\boldsymbol{\sigma}) = 0: &\quad \textit{yielding} \\ f(\boldsymbol{\sigma}) > 0: &\quad \textit{inadmissible region} \end{aligned} \tag{2-9}$$

Geometrically, the components of the stress tensor $\boldsymbol{\sigma}$ creates a surface, often called the yield surface. It is defined in such a way that the elastic range forms its interior, while the surface represents the plastic domain. For convenience, the yield criterion may be written on the form:

$$f(\boldsymbol{\sigma}) = \varphi(\boldsymbol{\sigma}) - \sigma_Y \tag{2-10}$$

where $\varphi(\boldsymbol{\sigma})$ is the equivalent stress, measuring the magnitude of the stress state to which the material is subjected, and σ_Y is the yield stress. Note that φ is assumed to be a positive homogenous function. In most metals and alloys, the plastic deformation will to a large extent take place by plastic slip (dislocations) and the materials are said to be pressure insensitive. Because of this, the yield criterion can be assumed to depend on the deviatoric stress state only.

von Mises yield criterion

The von Mises criterion is one of the most common methods to describe yielding in isotropic materials, due to its simple mathematical representation. The criterion is based on the assumption of isotropy and pressure insensitivity of the material [25]. It is assumed that yielding occurs when the second principal invariant of the stress deviator J_2 reaches a critical value k^2, namely $J_2 = k^2$. Mathematically, the von Mises yield criterion can be expressed by the stress deviator [23]:

$$f(\boldsymbol{\sigma}) = \sqrt{\frac{3}{2}\sigma'_{ij}\sigma'_{ij}} - \sigma_Y \tag{2-11}$$

2.4.2 Flow rule

In theories of plasticity for small deformations, it is generally accepted to decompose the strain tensor $\boldsymbol{\varepsilon}$ into an elastic and a plastic part:

$$\boldsymbol{\varepsilon} = \boldsymbol{\varepsilon}^e + \boldsymbol{\varepsilon}^p \tag{2-12}$$

where $\boldsymbol{\varepsilon}^e$ represents the (reversible) elastic strain and $\boldsymbol{\varepsilon}^p$ represents the (irreversible) plastic strain. Note that the time differentiated strain tensor $\dot{\boldsymbol{\varepsilon}}$ can be decomposed the same way.

Plastic deformation is a dissipative deformation process. It is assumed that work has to be done to the material at all times for the deformation continue, and thus we have the inequality:

$$\mathcal{D}\rho = \boldsymbol{\sigma}\dot{\boldsymbol{\varepsilon}}^p \geq 0 \tag{2-13}$$

where $\mathcal{D}\rho$ is the plastic dissipation per unit volume, which is assumed to dissipate as heat. The stress tensor and the plastic rate tensor is denoted $\boldsymbol{\sigma}$ and $\dot{\boldsymbol{\varepsilon}}^p$, respectively. The plastic strain rate tensor is defined through the general (non-associated) plastic flow rule:

$$\dot{\boldsymbol{\varepsilon}}^p = \dot{\lambda}\frac{\partial g}{\partial \boldsymbol{\sigma}} \tag{2-14}$$

where $\dot{\lambda}$ represents the non-negative plastic multiplier and g = g($\boldsymbol{\sigma}$) ≥ 0 is the plastic potential function.

Like the yield criterion, the flow rule represents a fundamental part of the material modeling. Therefore, it is often desirable to associate the plastic potential function with a yield function. By assuming that the plastic potential function g is defined by the yield function f, we obtain the associated flow rule:

$$\dot{\boldsymbol{\varepsilon}}^p = \dot{\lambda}\frac{\partial f}{\partial \boldsymbol{\sigma}} \quad \Leftrightarrow \quad d\boldsymbol{\varepsilon}^p = d\lambda\frac{\partial f}{\partial \boldsymbol{\sigma}} \tag{2-15}$$

Since the strain increment is proportional to the gradient of the yield function in the stress space, the associated flow rule implies normality. This means that the plastic strain increment vector is directed along the outward normal vector of the yield surface. In order to fulfill the dissipation inequality given in Equation (2-13), the yield function *f* has to constitute a convex surface, such that all possible combinations of $\boldsymbol{\sigma}$ and $\dot{\boldsymbol{\varepsilon}}^p$ remain non-negative [25].

2.4.3 Work-hardening

As described in Section 2.1, metals are built up from atoms that are arranged in a specific three-dimensional lattice. When a material yield, defects or misalignments arises and moves within the crystal. These irregularities are known as dislocations. The dislocations are able to move through the crystals in slip planes. Most crystals have several slip systems – the fcc lattice has twelve for instance [24]. As the material yields, dislocations on intersecting planes interact and obstruct each other. The accumulation of dislocations in the material makes the material stronger. This phenomenon is called work-hardening (also referred to as strain-hardening) [22].

Two of the most common ways to account for work-hardening are called isotropic hardening and kinematic hardening. Kinematic hardening involves a rigid translation of the elastic domain in stress space, which means that the yield surface is translated in the direction of the plastic flow.
Isotropic hardening corresponds to an isotropic expansion of the elastic domain, i.e. the yield surface keeps its shape during plastic deformation. In this particular thesis, isotropic hardening will be studied.

In order to account for isotropic hardening in the material model, an isotropic hardening variable R is introduced, which represents the expansion of the elastic domain. Because of this, the yield stress becomes a function of R, namely $\sigma_Y = \sigma_Y(R) = \sigma_0 + R$. Note that R is the strain-dependent increase of the yield stress, while σ_Y and σ_0 represents the flow stress and yield stress, respectively. The yield function in the presence of isotropic hardening can now be expressed as:

$$f(\boldsymbol{\sigma}, R) = \varphi(\boldsymbol{\sigma}) - \sigma_Y(R) \leq 0 \tag{2-16}$$

where $\varphi(\boldsymbol{\sigma})$ represents the equivalent stress.

There are numerous isotropic hardening rules proposed in the literature and the choice of a particular law depends mainly on the area of application and the actual material. Mathematically, a general isotropic hardening rule can be expressed as following:

$$\dot{R} = h_R \dot{\lambda} \tag{2-17}$$

where h_R represents the hardening modulus and $\dot{\lambda}$ is the plastic parameter which is equal to the plastic strain rate, denoted $\dot{p}$, for the associated flow rule. Two frequently used hardening rules are the power law and Voce rule. Both describe the evolution of the hardening variable R by the equivalent plastic strain p and are presented in Table 2-2.

Table 2-2: Hardening rules and their parameters. Note that associated flow is assumed. (Hopperstad and Børvik, 2013)

Hardening rule	Parameters
Power law	$R(p) = Kp^n$ $h_R = Knp^{n-1}$ K and n are hardening parameters fitted to experimental data.
Modified Power law	$R(p) = K(\varepsilon_0 + p)^n$ $\varepsilon_0 = \left(\frac{\sigma_0}{K}\right)^{\frac{1}{n}}$
Voce rule	$R(p) = \sum Q_{Ri}(1 - e^{-C_{Ri}p})$ $h_R = C_R(Q_R - R)$ C_R and Q_R are hardening parameters fitted to experimental data.

2.4.4 Flow stress ratio, R-value

As discussed earlier, the primary cause of anisotropy of plastic properties is the preferred orientation of the grains in the material. Lademo et al. [26] showed that aluminium alloys have a significant anisotropy in yield strength, plastic flow and ductility. Chen et al. [27] did extensive testing of extruded AA6xxx-T6 alloys under a wide range of strain rates. Results showed that AA6xxx alloys exhibit no significant rate sensitivity in the stress-strain behaviour. In order to study the anisotropy of the extruded aluminum profiles, tests were performed in three different directions: 0°, 45° and 90°, with respect to the extrusion direction of the plate.

A useful parameter to describe anisotropy and to calibrate the yield criterion is the R-ratio – often referred to as the ratio of plastic strains. The *R*-value is a measure of the flow properties of the material and it is defined as the ratio between the plastic strains in its width and thickness directions:

$$R_\alpha = \left.\frac{\dot{\varepsilon}_w^p}{\dot{\varepsilon}_t^p}\right|_\alpha \tag{2-18}$$

where $\dot{\varepsilon}_w^p$ and $\dot{\varepsilon}_t^p$ are the true, plastic strain increments in the width and thickness directions, respectively. The angle relative to the extrusion direction is denoted α.

To measure the magnitude of the thickness strain accurately can be somewhat challenging. A common way around this problem is to measure the plastic strain in the length direction ε_l^p and use the fact that $\varepsilon_t^p = -(\varepsilon_l^p + \varepsilon_w^p)$ [28].

Often, the strain increments are assumed to have the same ratio for increasing strains, which implies that Equation (2-18) can be rewritten as:

$$R_\alpha = \frac{\varepsilon_w^p}{\varepsilon_t^p} \tag{2-19}$$

As we would expect for an isotropic material, we have $R_\alpha = 1$ for all values of α. Accordingly, an R-value different from one signifies an anisotropic plastic flow of the material. Note that a high R-value implies that there is a high resistance to thinning of the plate.

A different way to go about anisotropy is to look at the flow-stress ratios (r-ratios). The r-ratio is an another parameter used to calibrate the yield function. It is defined as the uniaxial flow stress for a material direction α normalized to the uniaxial flow stress in a reference direction for a certain amount of plastic work, mathematically described as:

$$r_\alpha = \left.\frac{\sigma_f^\alpha}{\sigma_f^0}\right|_{W^p} \tag{2-20}$$

$$W^p = \int_0^{\varepsilon_\alpha^p} \sigma_f^\alpha \, d\varepsilon_\alpha^p \tag{2-21}$$

where σ_f^α is the flow stress in the angle α relative to the extrusion direction and σ_f^0 is the reference flow stress in the extrusion direction ($\alpha = 0°$). W^p is the specific plastic work for a given plastic strain ε_α^p.

A direct consequence of Equation (2-20), is that the flow-stress ratio always is equal to 1 in the extrusion direction, unlike the R-ratio given by Equation (2-18), which may take on different values.

Table 2-3: Test results AA6082-T6: R-ratios and flow-stress ratios
(1st line: Wang, 2006. 2nd line: Kårstad and Skajaa, 2015).

R_0	R_{45}	R_{90}	r_0	r_{45}	r_{90}
0.37	1.19	0.87	1.00	0.93	1.02
0.42	1.54	0.98	1.00	0.89	1.32

Wang [14] and Kårstad and Skajaa [12] performed uniaxial tensile tests of sheets made of aluminium alloy AA6082-T6. In order to characterize and measure the plastic anisotropy, the R-ratios and flow-stress ratios were calculated. The results presented in Table 2-2 indicate that the specimens exhibit significant anisotropy in plastic flow, with a strong tendency to thinning in the 0° (extrusion) direction.

A much more stable and less fluctuate behaviour is observed for the flow-stress ratios. Chen et al. [27] did similar testing on AA6082-T6 specimens and obtained approximately the same results for the three flow-stress ratios. Plastic anisotropy is accordingly nearly absent in the flow-stress ratios and because of the constant behaviour, it can be concluded that the material is quite well described by the assumption of isotropic hardening in the investigated uniaxial tension regime.

2.5 Fracture mechanics

2.5.1 General

Fracture could be defined as the separation, or fragmentation, of a solid body into two or more pieces, under the action of stress. The fracture process consists of two components, crack initiation and crack propagation, and it is also common to classify fractures in two categories, ductile and brittle fracture. Owing to the fact that aluminium is a ductile material, this thesis will only cover ductile fractures.

Ductile fractures are characterized by extensive plastic deformation prior and during the propagation of the crack, and the crack will commonly not extend unless an increased stress is applied. Usually, a considerable amount of deformation is also present at the fracture surface, resulting in a rough surface [29]. Another important property of this process is that the fracture occurs by a slow tearing of the metal with the expenditure of considerable energy. The different stages in the development of a ductile fracture are illustrated in Figure 2-8.

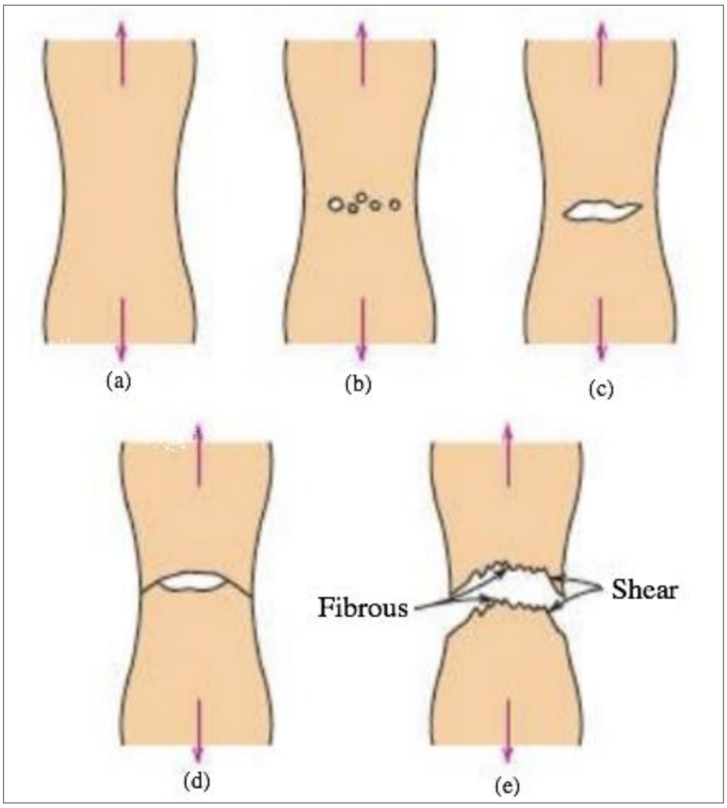

Figure 2-8: Stages in a ductile "cup-and-cone" fracture. (a) Initial necking. (b) Small cavity formation. (c) Coalescence of cavities to form a crack. (d) Crack propagation. (e) Final shear fracture at a 45-degree angle relative to the tensile direction (Callister, 2007).

The first step of a ductile fracture is necking (as discussed in 2.3.2). The necking introduces a triaxial state of stress, and a hydrostatic component of tension that acts along the axis of the centre of the necked region. This leads to the formation of many fine cavities (Figure 2-8 (b)), and if the specimen is exposed for increasing strain, these cavities will grow and coalesce into a central crack. This crack will grow, in a perpendicular direction to the axis of the force, until it reaches the surface. It then propagates along localized shear planes at roughly 45-degree angle, depicted in Figure 2-8 (e).

2.5.2 Fracture in friction stir welds

There are numerous papers and articles on the topic fracture behaviour of friction stir welded (FSW) aluminium alloys, e.g. Srivatsan et al. [30], Liu et al. [31] and Moreira et al. [32]. Common for all are that they indicate that the welding process significantly affects the tensile properties and fracture location of FSW joints. The reason for this is that the FSW gives rise to a softening of the material, especially in the thermo-mechanically affected zone (TMAZ) and in the nugget.

Results by Liu et al. [31] indicate that FSW joints are fractured under the conditions of local and heterogeneous deformation. The location of the fracture is at or near the interface between the weld nugget and the TMAZ, due to the significant difference in the internal structure in the two zones. The nugget is composed of fine recrystallized grains, while the TMAZ is composed of coarse-bent recovered grains [20]. It is also observed that the tensile properties of the joint are not the same on both sides of the welds: The lowest hardness was found at the retreating side of the joint i.e. fracture often occurs in this softened region where the initial mechanical strength of the alloy is lost [32].

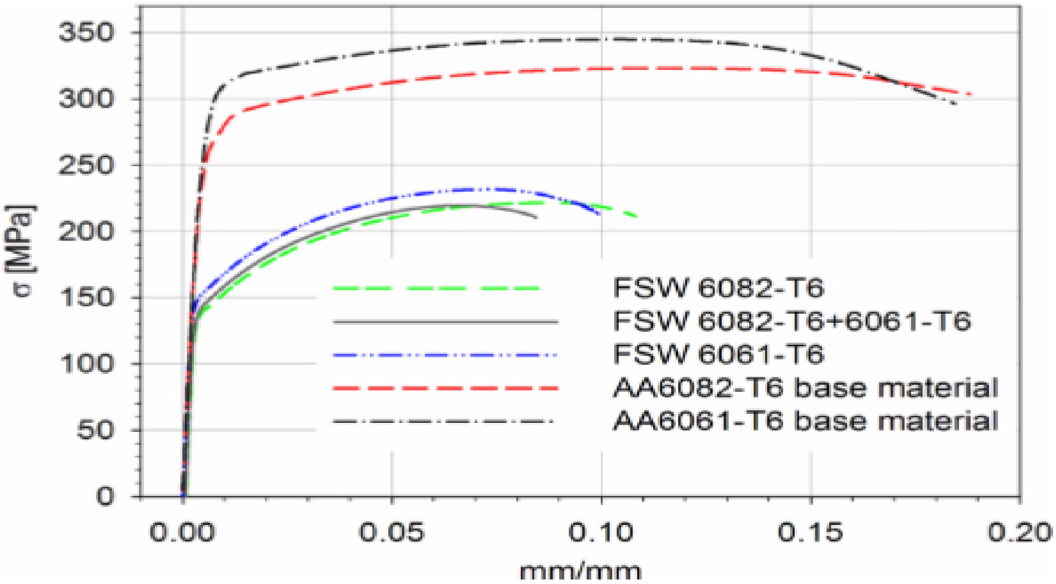

Figure 2-9: Stress-strain curves comparing the effects of FSW on tensile response of the AA6081 and AA6082-alloy aluminium alloy (Moreira et al., 2009).

2.5.3 Fracture criterion

Typically, fracture criterions for ductile materials express the deterioration of the material by an accumulative damage variable. There are numerous approaches for establishing a ductile fracture criterion numerically. The criterions used in the present study are the Cockcroft-Latham fracture criterion and the Bressan-Williams-Hill instability criterion.

The Cockcroft-Latham fracture criterion

The Cockcroft-Latham (CL) fracture criterion is a simple criterion based on a combination of stresses and strains. Therefore, the criterion was originally based on the total plastic work per unit volume at the fracture point. The criterion was later modified, since the original would only take into account the equivalent stress i.e. the current yield stress [33]. The shape of the necked area does not influence the current yield stress, which is incompatible to experimental facts. Therefore, Cockcroft and Latham proposed a modified criterion based on the tensile strain energy, where the magnitude of the highest normal stress is taken into account. At a uniaxial tensile test this would be the stress acting in the centreline where the fracture is initiated i.e. the peak stress $\sigma*$. The CL fracture criterion is only a description of observed experimental behaviour of metals, thus it is not considered a fundamental law. The concept of the criterion is that fracture is predicted when the following expression reaches a constant value C, for a given temperature and strain rate [34]:

$$\int_0^{\varepsilon_f} \bar{\sigma}\left(\frac{\sigma^*}{\bar{\sigma}}\right) d\bar{\varepsilon} = C \tag{2-22}$$

where ε_f is the fracture strain, $\bar{\varepsilon}$ and $\bar{\sigma}$ are respectively equivalent i.e. effective strain and stress, and $\left(\frac{\sigma^*}{\bar{\sigma}}\right)$ is a non-dimensional stress-concentration factor representing the peak stress $\sigma*$. If there is no tensile stress, but only a compressive stress, $\sigma^* = 0$, no fracture occurs. When used in calculations, the reduced form is often implemented:

$$C = \int_0^{\varepsilon_f} \sigma^* d\bar{\varepsilon} \tag{2-23}$$

Another way to define the CL criterion is derived from the concept that damage accumulates during straining. Fracture is initiated when W_1, a measure for energy per unit volume, reaches a critical value W_{cr}:

$$W_1 = \int_0^{p} \langle\sigma_1\rangle dp \leq W_{cr} \tag{2-24}$$

where σ_1 is the major principal stress and p is the equivalent plastic strain. At W_{cr} the values of the plastic strain is equal to the fracture strain [34].

Fracture will depend both on shear stresses, that give rise to plastic deformation and work hardening, and on tensile stresses. The CL fracture criterion will also allow the neck to evolve before failure is reached.
One of the disadvantages with the CL criterion appears when it is used on shell structures.
In these cases, it becomes computational demanding since it requires a high number of small elements. To capture the evolution of a neck, in a simulation using 4-node shell elements, the mesh size should be approximately equal to the thickness of the plate.

The Bressan-Williams-Hill instability criterion

In large-scale shell structures it may be convenient to define failure as the onset of local necking, instead of the point of fracture. The major reason for this is that a coarse mesh cannot detect the evolution of a local neck, i.e. it is possible to have an economical reasonable analysis in terms of computational time with failure at the onset of necking. The Bressan-Williams-Hill (BWH) instability criterion gives a simplified way of determining the onset of local necking, and is therefore appropriate to use in cases with large-scale shell structures [35]. The BWH instability criterion combines Hill´s local necking analysis with Bressan and Williams shear stress criterion. All of these concepts are based on the theory of forming limit diagrams.

Forming limit diagram (FLD) is a convenient and useful concept for characterizing the formability of sheet metal. The diagram shows the critical combination of major and minor strain in the sheet surface at the onset of necking [36]. When establishing a FLD, the strain paths are assumed proportional i.e. the strain ratio β between the minor and major principal strain rate remains constant during deformation.

$$\beta = \frac{d\varepsilon_2}{d\varepsilon_1} = \frac{\dot{\varepsilon_2}}{\dot{\varepsilon_1}} \tag{2-25}$$

In processes where large deformations take place, this is not necessary the case. Owing to various effects, such as material hardening, changed geometry and contact, the loading paths might change. This leads to non-proportional strain paths that could change the FLD. A simple alternative to the traditional strain-based FLDs is the stress-based FLDS, who remains more or less unaffected by altered strain paths, and can be conveniently converted from strain-based FLDs [37]. Stresses can be directly coupled to the plastic strain rates, through the relations between strain rates and conditions for yielding and plastic flow (see Section 2.4.2). This leads to a relation between the strain ratio β and the stress ration α, if the J_2 flow theory and plane stress conditions are assumed [35]:

$$\alpha = \frac{\sigma_2}{\sigma_1} = \frac{1 + 2\beta}{\beta + 2} \tag{2-26}$$

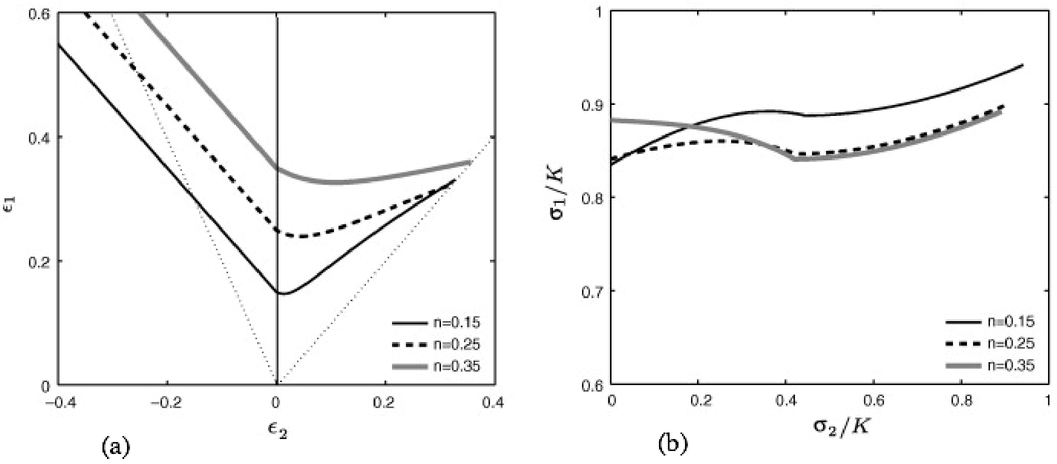

Figure 2-10: Forming limit diagrams in (a) strain space and (b) stress space. Both figures illustrate the same material. K and n refers to power law parameters (Alsos et al., 2008).

Hill´s local necking analysis [38] gives a criterion for local necking in the negative β regime i.e. it only yields rational results for a tension-compression strain state. Hill assumed that a local neck would form with an angle ϕ to the direction of the major principal stress. The orientation of the neck could be expressed as a function of the strain ratio β:

$$\phi = \tan^{-1}\left(\frac{1}{\sqrt{-\beta}}\right) \tag{2-27}$$

Within this neck, the strain increments along the narrow necking band will be zero. This leads to that the cross section of the neck will be subjected to plane straining. At the moment when a local neck is formed, the effect from strain hardening and the reduction in thickness balance each other. This indicates that the traction within the material reach a maximum value at the point of necking, and the traction increments is equal to zero, $dT_1 = 0$, which leads to the local necking criterion:

$$\frac{d\sigma_1}{d\varepsilon_1} = \sigma_1(1+\beta) \tag{2-28}$$

It is further assumed that the material stress-strain curve can be represented by the power law expression, $\sigma_{eq} = K\varepsilon_{eq}^{n}$ and that there is a proportionality between stresses and stress rates,

$$\alpha = \frac{\sigma_2}{\sigma_1} = \frac{\dot{\sigma_2}}{\dot{\sigma_1}} \tag{2-29}$$

If these assumptions are satisfied, the equivalent strain at necking can be expressed as:

$$\varepsilon_{eq} = \frac{2n}{\sqrt{3}} \frac{\sqrt{\beta^2 + \beta + 1}}{1 + \beta} \tag{2-30}$$

Directly from the power law expression it is then possible to find a path independent stress-based FLD and an equation for the equivalent stress at necking:

$$\sigma_{eq} = K\varepsilon_{eq}^{n} = K\left(\frac{2\tilde{n}}{\sqrt{3}} \frac{\sqrt{\beta^2 + \beta + 1}}{1 + \beta}\right)^{n} \tag{2-31}$$

where K and n still are the power law parameters, and $\tilde{n}$ is also a representation of the power law exponent n, but is denoted differently because it may be given element size dependent qualities. The expression for the equivalent stress leads to an equation for the major principal stress in the negative regime [39]:

$$\sigma_1 = \frac{\sigma_{eq}}{\sqrt{1 - \alpha + \alpha^2}} \tag{2-32}$$

$$=> \qquad \sigma_1 = \frac{2K}{\sqrt{3}} \frac{1 + \frac{1}{2}\beta}{\sqrt{\beta^2 + \beta + 1}} \left(\frac{2}{\sqrt{3}} \frac{\tilde{n}}{1 + \beta} \sqrt{\beta^2 + \beta + 1}\right)^{n} \tag{2-33}$$

This criterion does not give rational results for positive β, i.e. a tension-tension strain state, so other methods for estimating the onset of local necking are needed. Bressan and Williams established in 1982 a shear based instability criterion that could estimate the point of necking in the positive quadrant of the FLD [40]. The BW criterion may be solved analytically and can be used for failure estimation with reasonable accuracy at a low cost. The criterion is based on that the main mechanism of plastic deformation is slip arising from shear on certain preferred combinations of crystallographic planes and directions. In addition, some experimental data show that the failure planes in sheet metal lie close to the direction of maximum shear stress [40]. Thus, it is reasonable to assume that the instability takes place before any visual signs of local necking, and therefore, a shear stress based instability criterion could be useful to estimate the onset of local necking. The basis for the BW shear stress criterion follows three basic assumptions [35]:

- Shear instability is initiated through the thickness in the direction at which the material element experiences no change of length.
- The instability in the material is triggered by a local shear stress that exceeds a critical value, i.e. the initiation of local necking is a material property.
- Elastic strains are neglected.

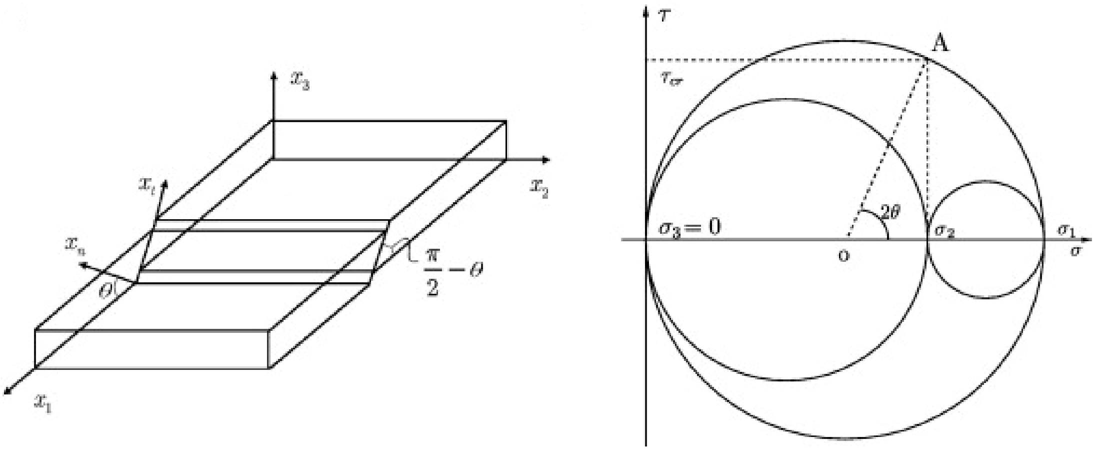

(a) (b)

Figure 2-11:(a) Local shear instability in a material element. (b) Mohr´s circle for the state of stress at the onset of necking (Alsos et al., 2008).

Based on the assumptions above, Bressan and Williams found a mathematical formulation for the criterion. As shown in Figure 2-11 (a), as the shear instability occurs, the inclined plane through the element thickness forms an angle $\frac{\pi}{2} - \theta$ to the shell plane. The material do not elongate in this direction, and the strain increment $\dot{\varepsilon_t} = 0$. This gives the following relation between the angle of the inclined plane and the principal strain rates:

$$\dot{\varepsilon_t} = \frac{\dot{\varepsilon_1} + \dot{\varepsilon_3}}{2} + \frac{\dot{\varepsilon_1} - \dot{\varepsilon_3}}{2} \cos 2\left(\theta + \frac{\pi}{2}\right) = 0 \qquad (2\text{-}34)$$

and since $\cos 2\left(\theta + \frac{\pi}{2}\right) = -\cos 2\theta$, the relation becomes:

$$\cos 2\theta = \frac{\dot{\varepsilon_1} + \dot{\varepsilon_3}}{\dot{\varepsilon_1} - \dot{\varepsilon_3}} \qquad (2\text{-}35)$$

Assuming volume constancy, $\dot{\varepsilon_3} = -\dot{\varepsilon_1}(1 + \beta)$, the angle θ can be expressed as a function of the strain ration β:

$$\cos 2\theta = -\frac{\beta}{2 + \beta} \qquad (2\text{-}36)$$

From the Mohr´s circle for the state of stress at onset of necking, in Figure 2-11 (b), or by the rules of stress transformation, the corresponding stress state can be found. This leads to the following relation between the inclined plane and the stresses involved:

$$\tau_{cr} = \frac{\sigma_1}{2} \sin 2\theta \qquad (2\text{-}37)$$

By combining Equation (2-36) and (2-37) the BW criterion can be expressed as:

$$\sigma_1 = \frac{2\tau_{cr}}{\sqrt{1 - \left(\frac{\beta}{2+\beta}\right)^2}} \tag{2-38}$$

where τ_{cr} is the critical shear stress, that can be calibrated at plane strain, i.e. $\beta = 0$. Note that there are multiple ways to calibrate the shear stress, but if the BW criterion is calibrated from Hill´s expression at plain strain, the critical BW shear stress takes the following form:

$$\tau_{cr} = \frac{1}{\sqrt{3}} K \left(\frac{2}{\sqrt{3}}\tilde{n}\right)^n \tag{2-39}$$

$$=> \qquad \sigma_1 = \frac{2}{\sqrt{3}} K \frac{\left(\frac{2}{\sqrt{3}}\tilde{n}\right)^n}{\sqrt{1 - \left(\frac{\beta}{2+\beta}\right)^2}} \tag{2-40}$$

The BW criterion was initially intended only for the positive quadrant of the FLD, but as the mathematical expression shows, it is also valid for negative values of β. However, for negative strain ratio the accuracy and validity of the BW criterion becomes uncertain. With that, to fulfil the wanted accuracy of the full range of β, the Hill and BW criterions have been combined into one criterion, *the Bressan-Williams-Hill instability criterion*. The resulting principal stress at incipient instability, in terms of the strain ratio, yields:

$$\sigma_1 = \begin{cases} \dfrac{2K}{\sqrt{3}} \dfrac{1 + \frac{1}{2}\beta}{\sqrt{\beta^2 + \beta + 1}} \left(\dfrac{2}{\sqrt{3}} \dfrac{\tilde{n}}{1+\beta} \sqrt{\beta^2 + \beta + 1}\right)^n , & if\ \beta \leq 0 \\ \dfrac{2}{\sqrt{3}} K \dfrac{\left(\frac{2}{\sqrt{3}}\tilde{n}\right)^n}{\sqrt{1 - \left(\frac{\beta}{2+\beta}\right)^2}} , & otherwise \end{cases} \tag{2-41}$$

Because the BWH criterion searches for local instability, it applies to membrane stresses and strains only, the effect of bending is not taken care of. When applying this criterion to a finite element code, this fact leads to that failure only is controlled in the mid through-thickness integration point of every shell element. Once the criterion is fulfilled, the element is removed and fracture is initiated. The simple nature of the BWH criterion makes it CPU efficient and may therefore be a cost effective and consistent alternative to more complex failure criterion.

In general, there is one major problem with finite element methods, which is the sensitivity to mesh size close to fracture. A coarse mesh might not detect the proper stress concentration, especially in zones with large strain gradients, e.g. close to crack tips, at structural intersections, like the transition to a stiffener, or in post necking zones. When using the BWH criterion, a consequence of this might be that the instability is predicted too late, and therefore leading to a non-conservative result. In order to overcome this problem, and get a robust failure response, a mesh scaling rule is required.

If a material follows the power law equation (Table 2-1) and the flow curve is given by this, it is possible to show that necking occurs for a strain equal to the strain-hardening coefficient n, when considering uniaxial tension. According to Hill´s analysis, the equivalent plastic strain at onset of necking, in uniaxial tension, is equal to $2n$. As mentioned earlier, the parameter $\tilde{n}$ corresponds to the strain-hardening coefficient, but is indicated differently because it may be given element size dependent qualities. Alsos et al. [39] proposed a geometric scaling of $\tilde{n}$ to solve this problem:

$$\tilde{n} = \frac{n}{2}\left(\frac{t_e}{l_e} + 1\right) \tag{2-42}$$

where t_e is the element thickness and l_e is the initial element length.

This implies that when the thickness/length ratio is approaching zero, the equivalent plastic strain at local necking approaches $\tilde{n}$, i.e. the same as the necking strain. With this scaling rule, referred to as geometric scaling, a coarse mesh will reduce the critical stress in Equation (2-41). In cases where stress concentrations are properly captured by a coarse mesh, the geometric scaling will lead to an underestimation of the stress instability, and therefore trigger instability to early.

2.6 Finite element method

In this section some aspects of the finite element method will be discussed. The general theoretical foundation of FEM is well established and well-documented, but since the theory is somewhat comprehensive, the emphasis will be on theory and methods that are relevant for this particular thesis, i.e. nonlinear finite element method (NFEM). If a more general presentation is desirable, there exists various text books about the topic, e.g. Cook et al. [41] and Hughes [42].

2.6.1 Impact problems and motivation of using nonlinear theory

The field of nonlinear finite element analysis (NFEA) have developed greatly over the last decades in which the increase of computational performance and capacity has played a key role. The range of application is huge and it has become particularly important in strength, stability and failure analysis. The finite element software has become more robust and user-friendly as well.

As discussed earlier, the impact phenomenon is a complex and highly nonlinear problem and the structural response can be markedly non-proportional to the applied load. Consequently, an effective use of NFEA requires a fundamental understanding of the problem, both physical and mathematically. Rules that apply to linear analysis does not necessarily apply to nonlinear problems and careful thoughts needs to be given to what is an appropriate measure of the behaviour. There are different sources of nonlinear physical behaviour [25]:

- *Material nonlinearity:*
  Material behaviour depends on current deformation state and deformation history.
  Other constitutive variables (strain-rate, pre-stress, time, etc.) may be involved.
- *Geometric nonlinearity:*
  Change in geometry as the structure deforms is taken into account in the
  kinematic quantities (displacement, strain and rotation) and equilibrium equations.
- *Nonlinear boundary conditions:*
  Both force and displacement depends on the deformation. Important for contact
  problems and hence for impact loading where bodies interact with each other.

The engineering significance of material nonlinearities varies across disciplines, but they are important to structural engineers that deals with nonlinear elasticity, plasticity, viscoelasticity or creep. This type of nonlinearity is a concern whenever the response for a given load causes strain levels in the material that not can be accounted for by linear stress-strain relationships (e.g. generalized Hooke’s law). A direct consequence of material nonlinearity is that the material properties may change with the applied loads.

An important assumption in linear systems is that, due to infinitesimal deformation, the difference between the deformed and initial state of the material is negligible. Geometric nonlinearities, in general, represent the cases when the relations among kinematic quantities are nonlinear, which implies that the linear analysis falls short of representing the deformation. This can be accounted for by defining suitable formulations (e.g. Lagrangian or Eulerian) that gives knowledge of the position occupied by the material particles comprising the body at all times [43].

A central part of impact loading is the interaction between two or more components in the system. The nonlinear boundary conditions are accounted for by introduction proper contact definitions. These conditions are discontinuous and nonlinear constraints on the system, which allows forces to be transmitted between components in the model. The boundary conditions are said to be deformation dependent because they only apply when the surfaces are in contact, which also explains the nonlinearity. The determination of the boundary conditions is a key part of the solution process and it exists various approaches on how to deal with it. For contact problems in this particular thesis, constraints are enforced using the penalty contact method in Abaqus. Interaction and contact formulations will be discussed in Section 2.6.2.

2.6.2 Explicit analysis

Integration schemes

As emphasized in Section 1.2, the impact phenomena include varying inertia forces and transmission of kinetic energy into strain energy over a short period of time.
In order to capture these effects, the response must be obtained through direct integration.
The various direct integration methods are classified into implicit or explicit schemes [44]:

- *Implicit method:*
  The displacement is obtained indirectly (implicitly) from the equilibrium conditions at time t_{n+1}, i.e. equation solving is required.
- *Explicit method:*
  The displacement at time t_{n+1} is obtained directly (explicitly) from the equilibrium conditions at one or more preceding time steps ($t \leq t_n$) without solving an equation system, i.e. unknown values are obtained from information that are already known.

The simulations in this thesis are performed with the explicit solving procedure in Abaqus, which is particularly well-suited to simulate brief dynamic events and large, nonlinear quasi-static deformation. The explicit dynamics analysis procedure in Abaqus/Explicit is based upon the implementation of an explicit integration rule with the use of lumped element mass matrices. As mentioned, the explicit method (often called the Central Difference Method) does not require any equation solving, which makes it computationally inexpensive. Convergence is not an issue since the method does not require equilibrium iterations. It is noteworthy that explicit method is conditionally stable, in the sense that the solution becomes unstable and diverges rapidly if the time increment is too big. In other words, the solution is bounded only when the time increment Δt is less than the stable time increment Δt_{cr}.

For most practical problems damping is likely to be small for all modes, which means that the stability limit is determined from the highest natural frequency (ω_{max}) and the damping ratio (ξ):

$$\Delta t \leq \frac{2}{\omega_{max}} (\sqrt{1 - \xi^2} - \xi) \tag{2-43}$$

As we can see from Equation (2-43), damping reduces the stable time increment.
In the non-damping case, the stability limit is dependent on the highest natural frequency only, and can be expressed as following:

$$\Delta t \leq \frac{2}{\omega_{max}} = \frac{L_e}{c_d} \tag{2-44}$$

where L_e is the characteristic length of the smallest element in the model and c_d is the current effective, dilatational wave speed of the element. Abaqus/Explicit calculates the wave speed on the basis of material parameters (Lamé parameters and density) [45]. Note that higher-order elements have higher frequencies than lower-order elements and tend to produce noise when stress waves move through the finite element mesh. Thus should higher-order elements be avoided when using explicit time integration.

Energy balance

An additional check for numerical stability is the energy balance check, which originates from the conservation of energy implied by the first law of thermodynamics. Numerical instability because of artificial energy is a problem that may arise when impact problems are solved with the explicit method and should therefore be controlled. An energy balance for the entire finite element model can be written as:

$$E_I + E_V + E_F + E_K - E_W = E_{total} = constant \tag{2-45}$$

where

E_I	Internal energy (elastic strain energy, energy dissipated through plasticity, viscoelasticity or creep and artificial strain energy stored in hourglass control and shear in the elements)
E_V	Viscous energy dissipated
E_F	Frictional energy dissipated
E_K	Kinetic energy
E_W	Work done by external loads and contact penalties
E_{total}	The sum of the energy components

An important aspect of this check is that the sum of energy within the finite element model should be constant, with an acceptable error of approximately 1-2% [46].
Large values of artificial energy may indicate that mesh refinement or other changes to the mesh are necessary.

Contact

Contact conditions are discontinuous nonlinear constraints which allow forces to be transmitted from one part of the model to another. Abaqus/Explicit provides two algorithms for modeling contact interactions [47]. The general contact algorithm allows a definition of contact between many or all regions of a model with a single interaction. It has few restrictions and will therefore be adequate for most contact problems and thus be suitable for our simulations.
The contact pair algorithm describes the contact between two surfaces. This algorithm has more restrictions on the types of surfaces involved and often requires more careful definition of contact. However, it allows for some interaction behaviour that not are available with the general contact algorithm.

For general contact Abaqus/Explicit enforces contact constraints using a penalty contact method, which searches for node-into-face and edge-into-edge penetrations in the current configuration. The method imposes the contact condition by extending the potential energy of the system by a penalty term. The penalty parameter can be interpreted as a spring stiffness in the contact interface [48].

Because the penalty method introduces additional stiffness behaviour into the model, this stiffness can influence the stable time increment. Abaqus/Explicit automatically accounts for the effect of the penalty stiffness in the automatic time incrementation, although this effect is usually small [46]. A friction coefficient can be defined for both surface-based and element-based contact in the model. Abaqus assumes by default that the interaction between contacting bodies is frictionless – which may be a non-valid assumption in the simulations. This will be further discussed in the next two chapters.

2.6.3 Quasi-static analysis

The application of explicit dynamics to model quasi-static events requires special consideration. Dynamic events happen over a short period of time (rapid loading), while quasi-static events happen over a considerably longer time period (slow loading). Because of this, it is often computationally impractical to model the process in its natural time period and it is necessary to artificially increase the speed of process in the simulation. There are two approaches to obtaining an economical quasi-static solution with the explicit dynamics method [49]:

- *Increased load rates:* Artificially reduce the time scale of the process by increasing the loading rate.
- *Mass scaling:* Artificially increase the size of the stable time increment. Note that this is the only option for reducing process time in a rate-dependent material.

Bear in mind that both these methods increase the speed of process and as a result of this, the system (partially) evolves into a state of dynamic equilibrium where inertia forces become more dominant. Consequently, the goal is to model the process in the shortest time period or with the most mass scaling in which inertia forces are still insignificant.

As in the dynamic analysis, an energy balance equation can be used to help evaluate whether a simulation is yielding an appropriate quasi-static response or not. Since the results can depend strongly on the process speed, it is vital to ensure that unrealistic results are not being generated by excessive artificial scaling. The kinetic energy of the deforming material should not exceed a small fraction (*5-10%*) of its internal energy throughout the analysis [50].

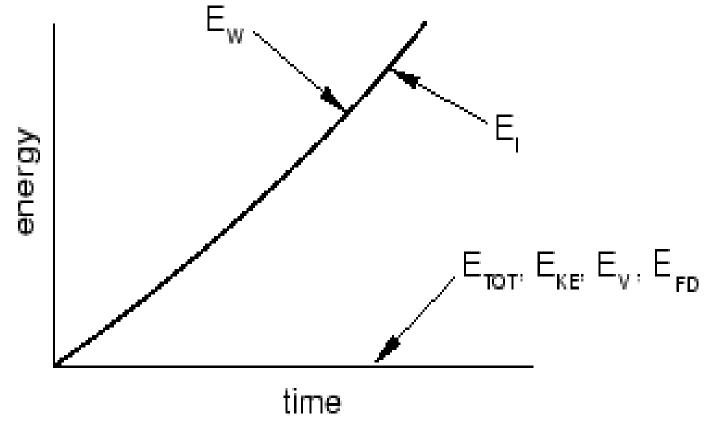

Figure 2-12: Energy history output for a quasi-static analysis

2.6.4 Plate theory

According to plate theory, a plate is a flat structural element where the thickness, t, is small compared with the surface dimensions. In a plate, the xy-plane is located in the centre of the plate, in distance $\frac{t}{2}$ from the two surfaces. This plane is assumed to act as a neutral surface, i.e. it is free for in-plane strains ($\varepsilon_x = \varepsilon_y = \gamma_{xy} = 0 \; at \; z = 0$).

Depending on the ratio between the thickness and a characteristic length of the surface, L, it is common to distinguish between thick, medium thick and thin plates. In this thesis we will only look into cases with thin plates, i.e. $\frac{t}{L} < \frac{1}{10}$. For thin plates the Kirchhoff theory is often used. Transverse shear deformation is neglected in this theory, and therefore, determining the lateral deflection of the mid-surface solves a thin plate problem [51].

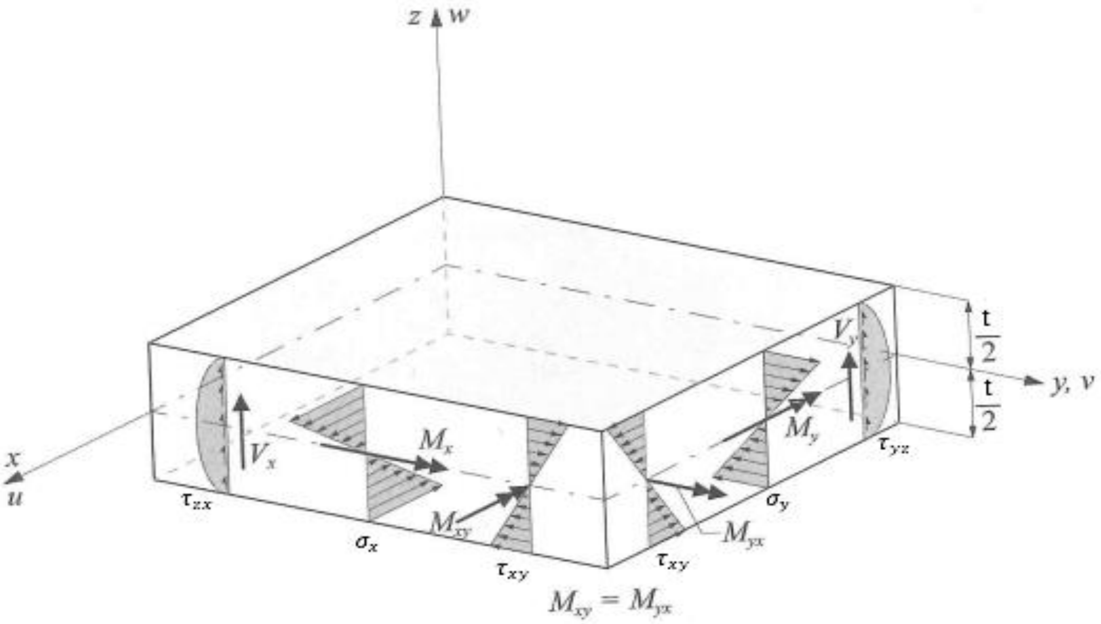

Figure 2-13: Stresses and associated moments and transverse shear forces (Bell, 2014).

The stresses over the cross-section for a linearly elastic and isotropic material are represented in Figure 2-13, and given by the following expression:

$$\begin{bmatrix} \sigma_x \\ \sigma_y \\ \tau_{xy} \end{bmatrix} = \frac{Et^3}{12(1-\nu^2)} \begin{bmatrix} 1 & \nu & 0 \\ \nu & 1 & 0 \\ 0 & 0 & \frac{(1-\nu)}{2} \end{bmatrix} \begin{bmatrix} \varepsilon_x \\ \varepsilon_y \\ \gamma_{xy} \end{bmatrix} = \boldsymbol{C\varepsilon} \qquad (2\text{-}46)$$

Usually these stresses are associated with moments and forces per unit of length in the xy-plane. Due to the fact that shear deformations are neglected for thin plates ($\gamma_{yz} = \gamma_{zx} = 0$), the shear forces V_x and V_y in Figure 2-10 can only be determined indirectly, from equilibrium considerations.

On the other hand, the moment-curvature relations for a homogeneous and isotropic Kirchhoff plate are given by:

$$M = \begin{bmatrix} M_x \\ M_y \\ M_{xy} \end{bmatrix} = -D \begin{bmatrix} 1 & \nu & 0 \\ \nu & 1 & 0 \\ 0 & 0 & \frac{(1-\nu)}{2} \end{bmatrix} \begin{bmatrix} w_{,xx} \\ w_{,yy} \\ 2w_{,xy} \end{bmatrix} = -\boldsymbol{D}\boldsymbol{c}_k \tag{2-47}$$

where D is the flexural rigidity for a plate, analogues to flexural stiffness EI of a beam, and $\boldsymbol{c}_k$ is the curvature vector for thin Kirchhoff plates [41].

2.6.5 Shell elements

A shell section has a lot of the same properties as a plate, but the principal difference is that the middle surface is curved. A curved structural form is in most cases a very efficient load-bearing form. The characteristic property of a shell structure is that the stresses can be represented as the superposition of membrane (in-plane) stresses and bending (out-of-plane) stresses. A shell can carry a large load if membrane stresses dominate, so it is favourable with small bending stresses [41].

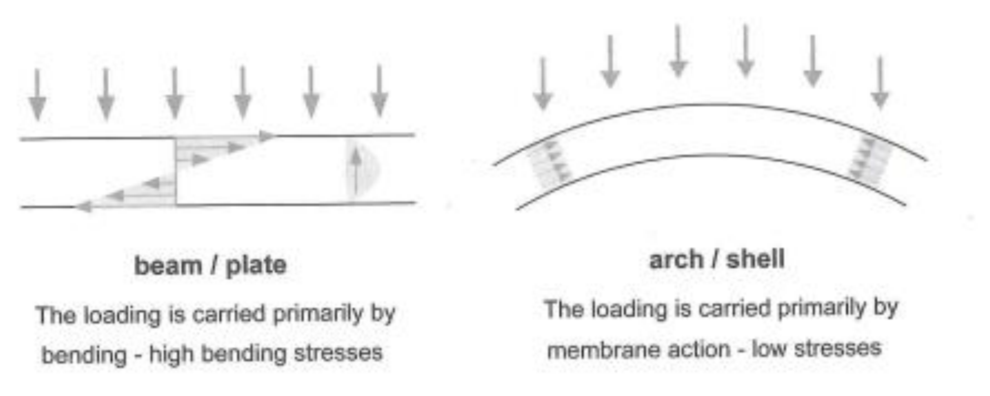

Figure 2-14: Load bearing by bending (out-of-plane) and membrane (in-plane) action (Bell, 2014).

The simulations in this thesis are simulated with conventional shell elements. Abaqus offer three different conventional shell elements; general-purpose and an element valid for thick and thin shell problems. For most applications, this thesis included, the general-purpose elements are used because these elements provide robust and accurate solutions in almost all loading conditions. For thin shell problems the general-purpose elements are described by discrete Kirchhoff theory [50].

In this thesis, the robust *S4R*-element with linear interpolation is used. This is a 4-node, quadrilateral shell element with reduced integration, and a large-strain formulation. The stiffness of the element is calculated in every integration point through the thickness of the shell i.e. the non-linear behaviour in the material is described with greater precision. The integration points through the thickness of the element are illustrated in Figure 2-15.

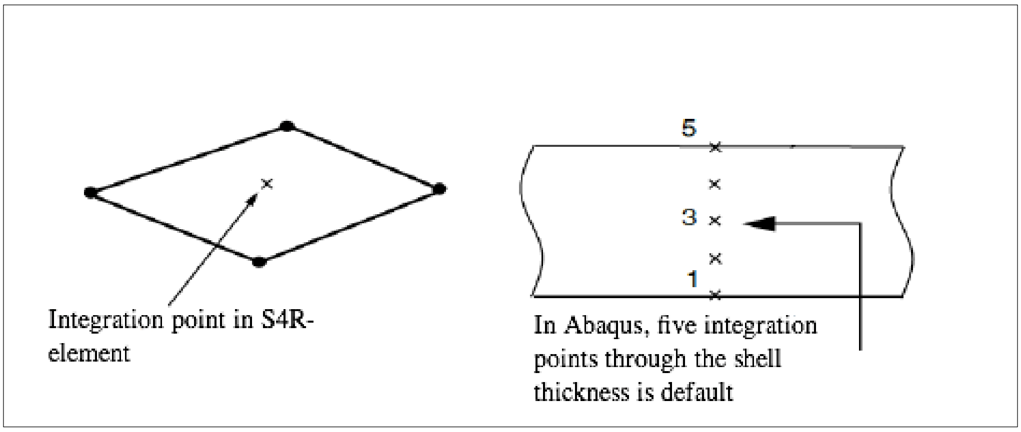

Figure 2-15: Shell element (S4R) in Abaqus

The S4R elements do not suffer from transverse shear locking, nor do they have hourglass modes in either the membrane or bending response of the element, hence, the element does not require hourglass control. The formulation of the elements allows thickness change as a function of in-plane deformations. The change in thickness is based on the *effective section Poisson´s ratio*, and is calculated as follows, for in plane stress $\sigma_{33} = 0$:

$$\varepsilon_{33} = -\frac{\nu}{1-\nu}(\varepsilon_{11} + \varepsilon_{22}) \tag{2-48}$$

For $\nu = 0.5$ the material is incompressible, and for $\nu = 0.0$ the section thickness remains unchanged.

3. Dr ing. thesis of Hilde Giæver Hildrum

3.1 Experimental programme

The static tests by Hildrum was carried out by using a 1000 kN hydraulic actuator in the laboratory. A blunt and a hemispherical indenter, both made of steel grade SS2541, was used to study the impact behaviour of the stiffened aluminium plates. Each test specimen was loaded transversely at a constant rate of 3 mm/min until peak load (fracture) was reached. The force was measured using two oil pressure transducers. The full experimental setup is illustrated in Figure 3-1.

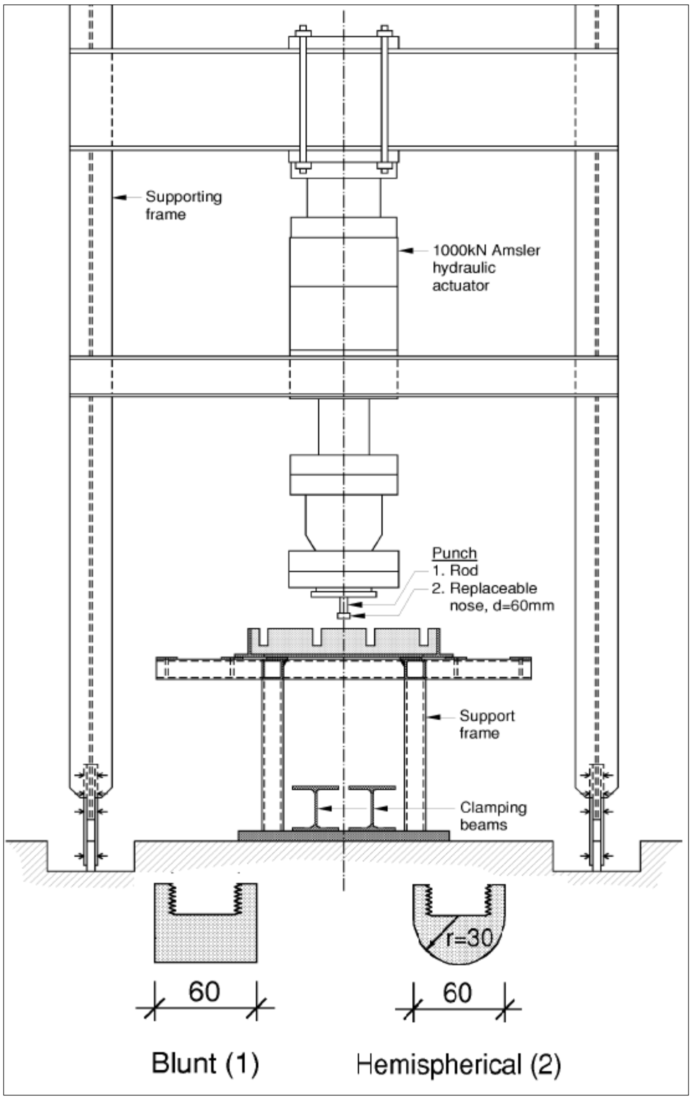

Figure 3-1: Experimental setup for the static tests (Hildrum, 2002)

The plates used in the experiments were extruded aluminium (AA6082-T6) panels, with L-stiffeners, joined together with MIG-welds. The exact geometry of the plates is given in Figure 3-2. The stiffened plates were simply supported with two supports in the x-direction and four supports in the y-direction. To minimize the friction between the supports and the plate, Teflon grease was used. Note that there was carried out tests in three different loading positions (setup A, B and C).

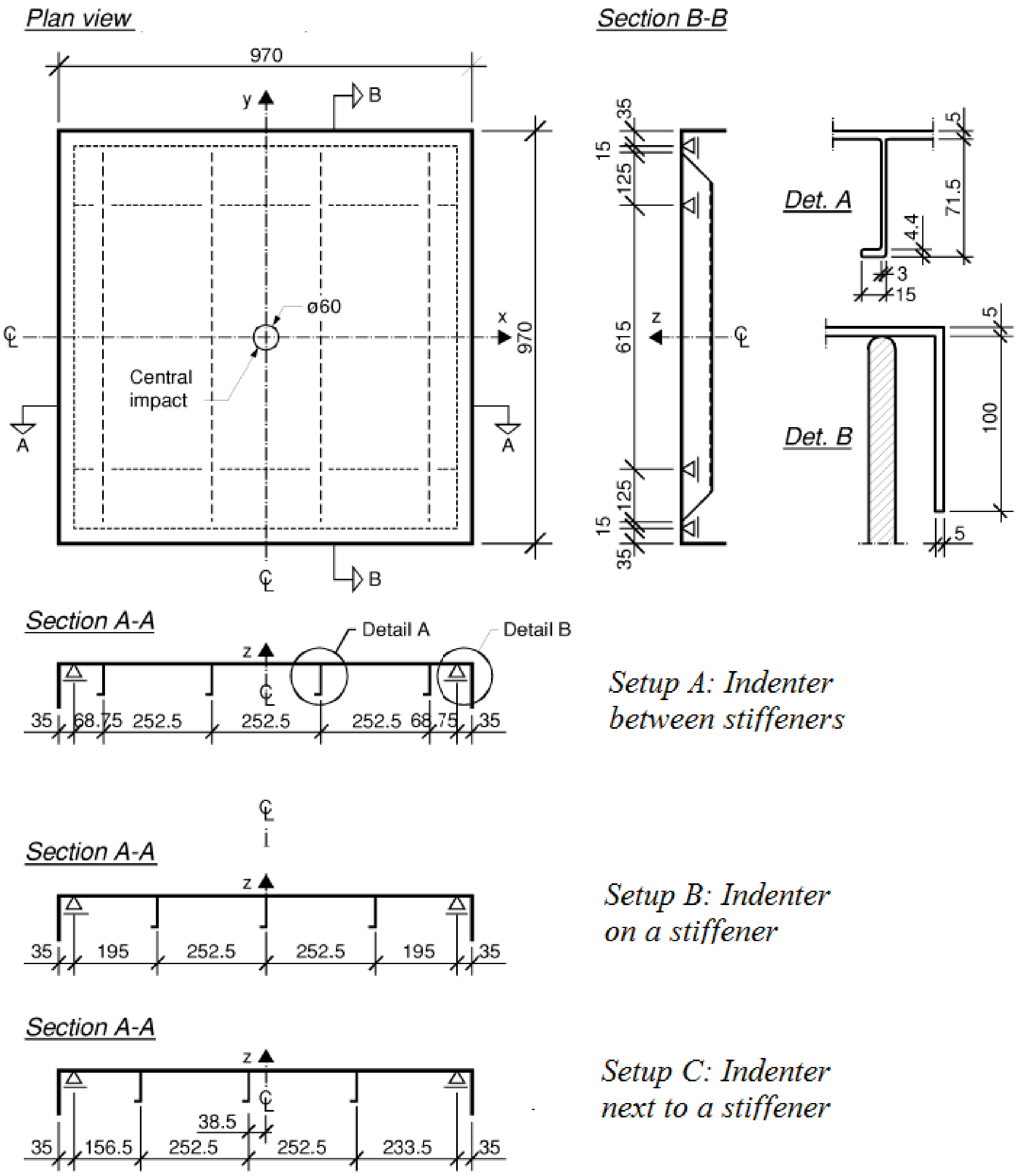

Setup A: Indenter between stiffeners

Setup B: Indenter on a stiffener

Setup C: Indenter next to a stiffener

Figure 3-2: Plate geometry, loading positions and idealised boundary conditions (Hildrum, 2002)

3.2 Numerical modelling

Different numerical models have been created in order to replicate some of the experiments conducted by Hildrum in her Dr Ing. thesis [10]. Hildrum implemented a small numerical investigation in her thesis, using the commercial code LS-DYNA. However, only one of the numerous tests were simulated and it was desirable to establish new numerical models in Abaqus to simulate more of the experiments.

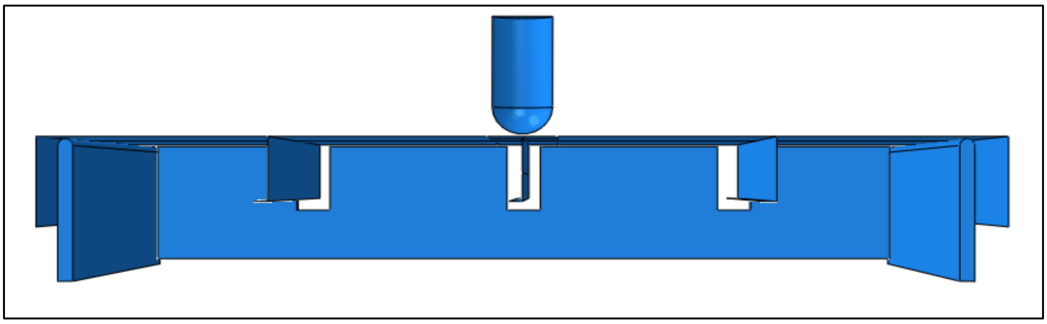

Figure 3-3: Snapshot of the replicated model with a hemispherical indenter

The geometry of the plate and support conditions are modelled as similar as possible to the original test setup from the experiments. The idealised support conditions are simply supported and the nodes at the supports are fixed in the direction normal to the plate. In order to save some computational time, only half of the system was modelled and symmetry was enforced in the simulations. One of the models is illustrated in Figure 3-3.

Hildrum used Belytschko-Tsay shell elements in the numerical simulations. This type of shell element has four-nodes and one point reduced in-plane integration, which make them identical to the S4R-elements available in the Abaqus library. Consequently, these elements were used in the simulations. Five integration points through the element thickness were used in order to capture bending. However, due to different commercial codes, there are some variations in the models. Hildrum modelled the contact between the indenter and plate using a *nodes-to-surface* penalty formulation without friction, while the interaction in the new model is as a *surface-to-surface* kinematic contact formulation with a friction coefficient equal to 0.61 [52].

Hildrum carried through both dynamic and static tests, but due to further research on the relationship between dynamic capacities and the corresponding static ones by Kårstad and Skajaa [12], it is concluded that simulations of the static punch test will be sufficient to get satisfying results for the impact behaviour of an aluminium plate. Accordingly, there are only completed static simulations in this thesis.

Beyond this, the two different numerical simulations are virtually equal. The supports were modelled as perfectly plastic deformable parts, with the material properties of S355 steel. Both the hemispherical and the blunt indenter were modelled as discrete rigid bodies. The material properties used in the model are collected from material tests that Hildrum did for the AA6082-T6 alloy. Key values are given in Table 3-1.

Table 3-1: Key values for AA6082-T6. (Hildrum, 2002)

	E *[MPa]*	$\boldsymbol{\sigma_0}$ $[MPa]$	***K*** *[MPa]*	***n***
AA6082-T6	70 000	329	523.1	0.11

As an idealization, both the plate and the stiffeners have been assigned the same material properties and the plate is modelled without any welds. Material cards are generated in MATLAB and two different fracture criterions are used to describe and capture material fracture within the model. The relevant codes are presented in Appendix A.

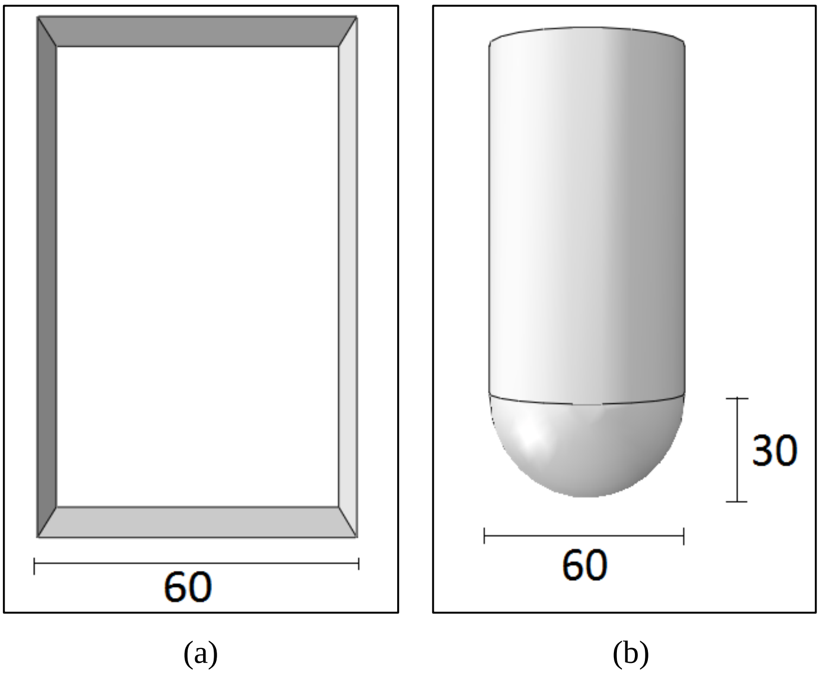

(a) (b)

Figure 3-4: Geometry of: (a) Blunt indenter (b) Hemispherical indenter

3.3 Results and discussion

With help from the computer program *PlotDigitizer*, data from the experiments carried out by Hildrum were collected and compared with the numerical results from the simulations in Abaqus. The key values are given in Table 3-2. Note that the numerical values presented are collected from the simulations with a mesh size equal to the thickness of the structural elements. The coherence between the force and displacement is plotted up to initiation of fracture, for both the numerical and experimental data (Figure 3-8). Even though there are some deviations between the results, the numerical model captures some of the same failure modes that were observed in the laboratory experiments.

Table 3-2: Comparison of numerical and experimental data for aluminium plates with L-stiffeners. Experimental data is collected from static tests by Hildrum (2002).

Test series	**Load position**	**Nose shape**	$F_{numerical}$ [kN]	$w_{numerical}$ [mm]	F_{su} [kN]	w_{cm} [mm]
A1	Between stiffeners	Blunt	50.5	24.9	57.0	25.7
A2	Between stiffeners	Hemispherical	39.7	24.4	32.2	25.3
B1	On a stiffener	Blunt	95.8	40.3	80.0	30.7
B2	On a stiffener	Hemispherical	78.5	40.6	57.9	29.0
C1	Next to a stiffener	Blunt	74.4	34.1	63.9	25.6
C2	Next to a stiffener	Hemispherical	58.1	37.0	51.8	31.0

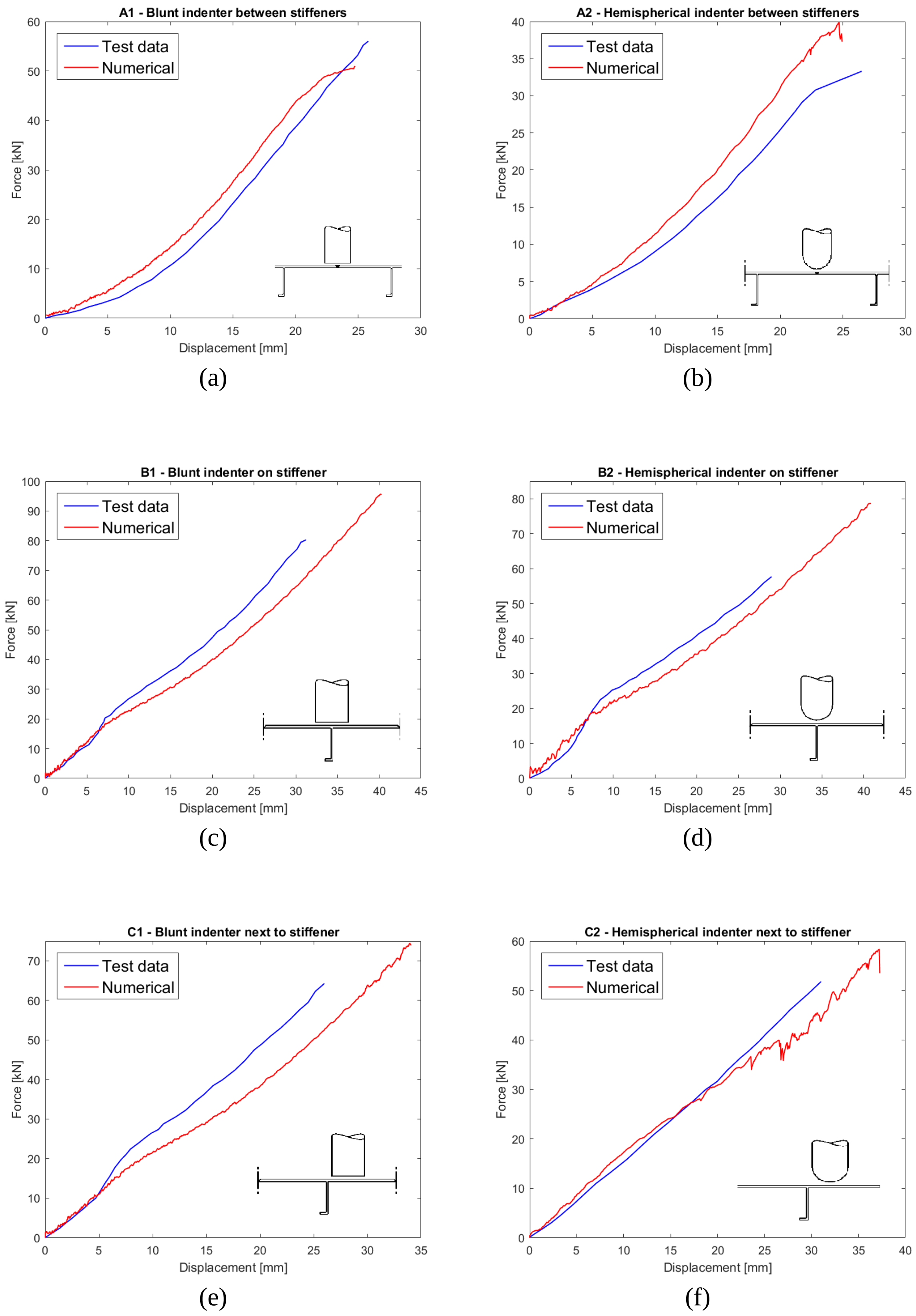

(a) (b)

(c) (d)

(e) (f)

Figure 3-5: Force-displacement curves: (a) Blunt nose between stiffeners, (b) Hemispherical nose between stiffeners, (c) Blunt nose on top of stiffener, (d) Hemispherical nose on top of stiffener, (e) Blunt nose next to stiffener, (f) Hemispherical nose next to stiffener

Figure 3-6 show the final deformation of the plate for the different test setups. The deformation is dependent on many different variables, for instance the boundary and loading conditions. As mentioned, the idealised support conditions for the numerical simulation are simply supported, i.e. the plate is free to rotate and displace at the supports.

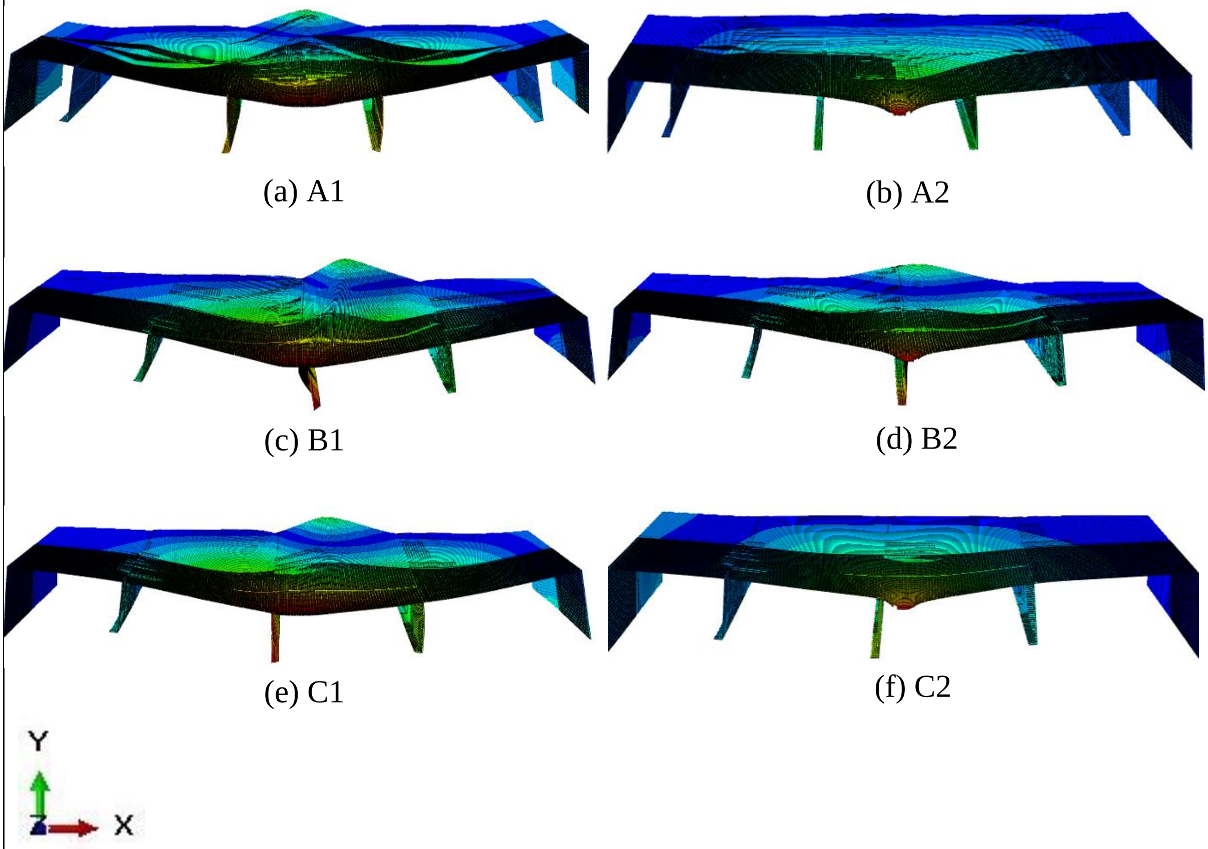
(a) A1

(b) A2

(c) B1

(d) B2

(e) C1

(f) C2

Figure 3-6: Deformation of the plate, with von Mises stress

With the blunt indenter, Figure 3-6 (a), (c) and (e), the deflection and deformation of the plates are in many ways similar for the three different setups. Most of the deformation takes place in the middle of the plate, under the indenter, but due to large stress concentrations in this area, deformations arise in other part of the plate as well. On the rear boundary, the plate will be forced up since the plate is free to displace in a positive y-direction. Some of the same behaviour is also observed for the test with a hemispherical indenter on the stiffener (setup B2), as seen in Figure 3-6 (d). With the blunt indenter on the stiffener (setup B1), rotation and lateral displacement of the stiffener are observed.

For test setup A2 and C2, as seen in see Figure 3-6 (b) and (f), the deformation patterns are very similar. The overall deformation of the plate is lower for these two cases, as most of the plastic strain is located in the middle stiffener and the area around the indenter. The magnitude of the stresses at the boundaries remain small, which explains why very little plastic deformation takes place there and the geometry remains unchanged.

When the load was placed between the stiffeners with a hemispherical indenter (test A2), petals were created for a specimen loaded beyond incipient fracture. This phenomenon was observed in both the experiments and the numerical simulations, see Figure 3-7 (a) and (b). In test setup B, where the indenter was placed on a stiffener, diffuse necking in the bottom flange of the stiffener was observed. This was followed by fracture that propagated into the web and further into the top flange for a deformation larger than the displacement corresponding to the maximum load. Although the fracture initiated for a higher force and displacement in the numerical analysis, the same fracture phenomena was observed here. The tensile fracture of the stiffener flange is illustrated in Figure 3-7 (c) and (d). The indenter placed next to a stiffener resulted in similar failure modes as for test setup A and this was also captured in the numerical model.

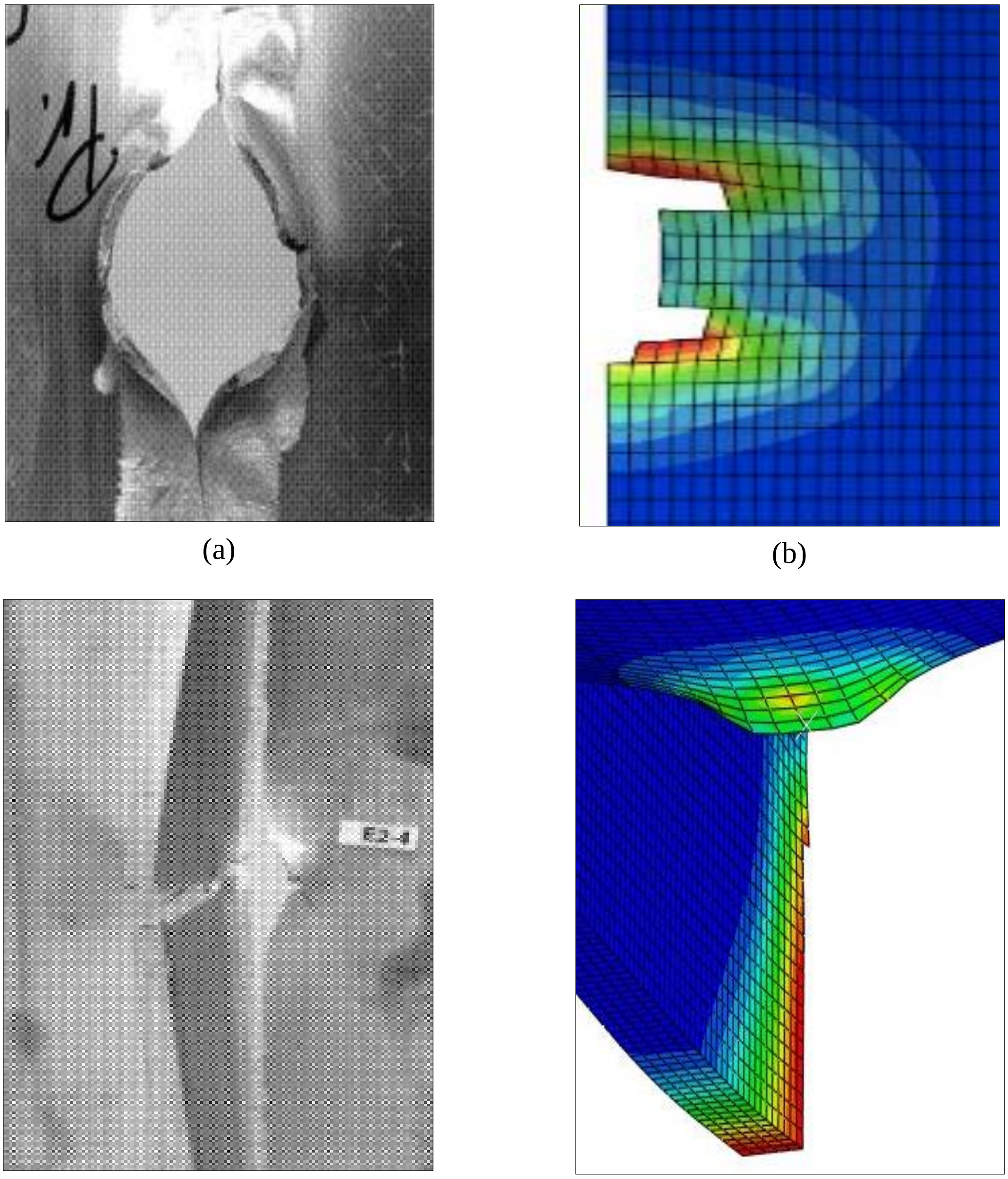

(a) (b)

(c) (d)

Figure 3-7: Failure modes: (a) A2 –failure in plate (experimental), (b) A2 – numerical (c) B1 –failure in stiffener (experimental), (d) B1 – numerical

The indenter has a constant velocity of 700 mm/s in the simulations and it should not be any brief, dynamic effects in the system. As mentioned in Section 2.6.3, an important aspect of the quasi static analysis is to make sure that the inertia forces remain small or non-existent in the system. In Figure 3-8, an energy history output over the time period of 0.1 second is shown. As the curves indicate, the kinetic energy is only a small fraction of the internal energy, i.e. it is appropriate to assume that the simulation gives an acceptable and stable solution.

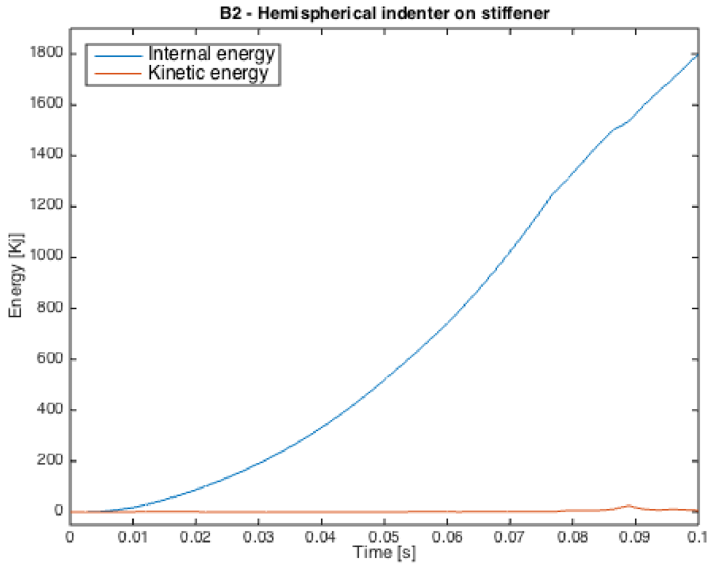

Figure 3-8: Internal and kinetic energy history output

Figure 3-9 illustrates why a fine mesh is important in many numerical simulations to obtain sufficient or better estimations. Even though the results are conservative, a mesh size equal to the thickness should be used to describe the deformation process and fracture initiation as accurate as possible.

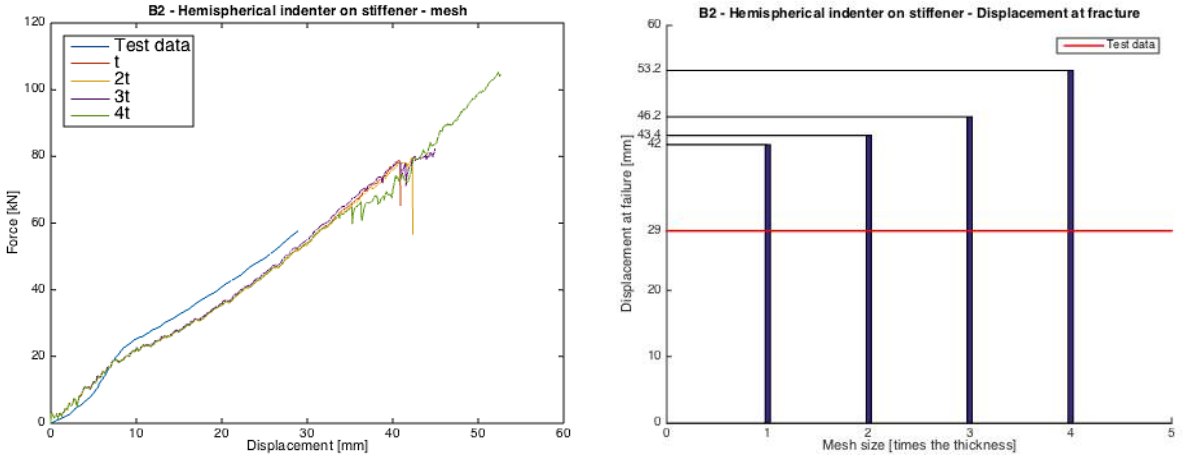

(a) (b)

Figure 3-9: (a) Force-displacement curve for different mesh sizes.

(b) Displacement at failure for different mesh sizes.

Material

There could be several reasons for the aberrations observed between the experimental and numerical data. Most of these are related to uncertainties around the simplification of the material properties used in the numerical model. The whole plate, both stiffeners and the upper flange, are modelled with the same material. In the material tests conducted by Hildrum, some deviations between the properties in the stiffeners and the top flange of the panels were found. Other research, e.g. Paulo et al. [53], suggests that different material properties in the stiffeners and the base material in aluminium panels are common and should therefore be accounted for in the numerical models.

There are also some uncertainties attached to the way the implemented material handle plasticity. For test setup B and C, where the stiffeners constitute a large part of the capacity of the panels, the results from the simulations and from the experiment are close to identical in the early phase of the simulations, but after a while some clear aberrations are seen. After a thorough investigation of the simulations it turns out that the aberrations initiate at the time when plastic strains are introduced in the stiffener, i.e. the yield strength is exceeded. This indicates that the accuracy in the simplified material model with the von Mises yield criterion and power law as hardening rule, may not be good enough to handle plasticity in a sufficient way.

As a check, some adjustments of the material properties in the numerical model were made. The stiffeners were made softer than the base material in the plate by reducing the yield stress and the Young's modulus. As Figure 3-10 illustrates, a better numerical estimation is obtained, both in the elastic and the plastic regime. The fracture is more accurately described as well. The sudden increase in the stiffness of the plate is still not captured perfectly by the numerical model, but it gives a better estimation.

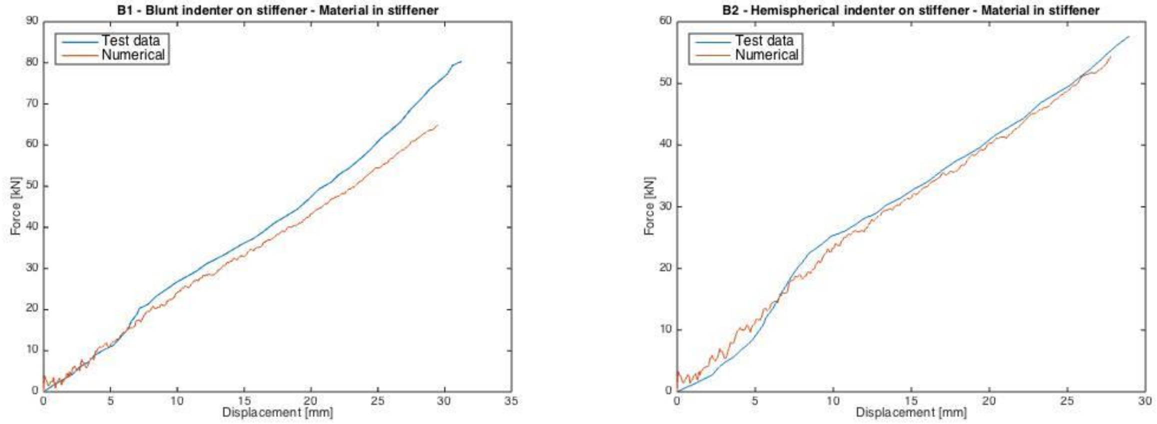

(a) (b)

Figure 3-10: Force-displacement curves with new material properties in the stiffener. (a) B1 numerical, (b) B2 numerical
$E = 65000$ MPa, $\sigma_0 = 300$ MPa, $K = 550$ MPa, $n = 0.05$.

Another possible source of error is that the panels are modelled without welds. Hildrum investigated the difference in material properties between the welding zone and the base material and concluded that there were noticeable differences in both yield strength and the hardening parameters. The yield strength in the HAZ was found to be a ratio of 0.64 softer than the yield strength in the base material. This could especially influence the results for setup A, where the place of impact is right above a weld.

Fracture criterion

The two fracture criterions, Cockcroft-Latham (CL) and Bressan-William-Hill (BWH), have been implemented in order to study how well they predict and describe fracture in the material. Since BWH predicts local instability, as opposed to CL that predicts final fracture, it is expected that the BWH will yield a lower incipience fracture force. This effect is clearly captured in setup B and illustrated in Figure 3-11 (a). Another characteristic of BWH, that may explain why this effect is not that clearly detected in setup A (Figure 3-11 (b)), is that the BWH criterion handles tension and compression in different ways. As described in Chapter 2, the foundation of the BWH instability criterion is forming limit diagrams (FLD). When the instability occurs in a tension-exposed part, like the stiffener in test B2, the left side of the FLD, i.e. Hill´s theory, will describe the instability. However, in setup A, the fracture will occur in the plate, and the instability is described by the positive quadrant of the FLD and thus, Bressan-Williams theory.

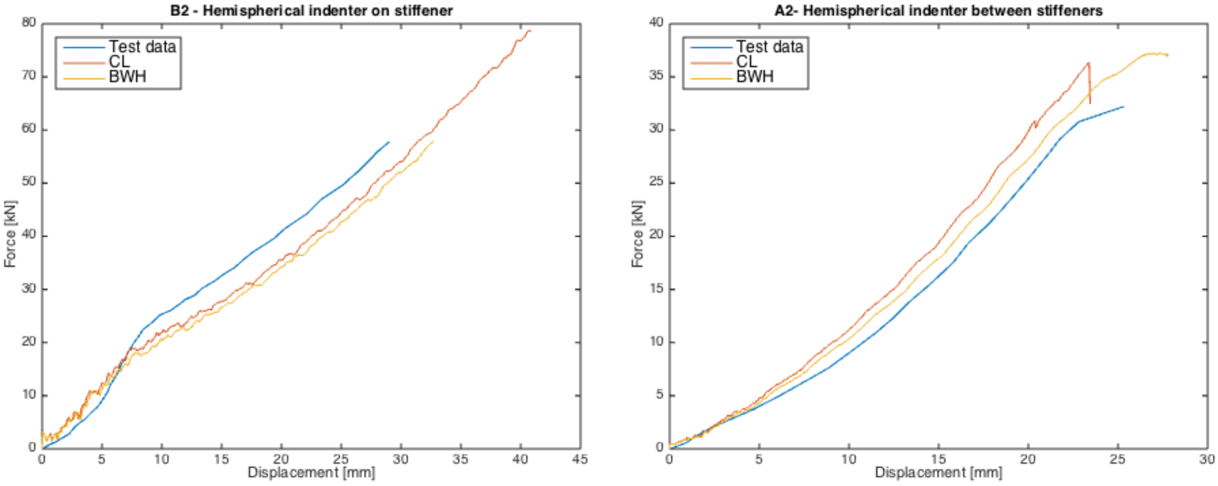

(a) (b)

Figure 3-11: Force-displacement curves with different fracture criterions, (a) B2, (b) A2

4. Preliminary analysis of T6- and T4-plates

4.1 Experimental program

Kårstad and Skajaa [12] did quasi-static experiments as part of their study on stiffened aluminum plates. A picture of the complete test rig is shown in Figure 4-1. The test setup is in many ways similar to the one used by Hildrum in her Dr. Ing. thesis, but with some adjustments and newer equipment. After some discussion, they chose to use a cylindrical indenter in their tests. The specimens were loaded transversely, between the stiffeners, at a constant rate of 10 mm/min and there was carried out experiments with the indenter both longitudinal and transversal to the extrusion direction. A laser was attached to hydraulic actuator to measure the deformation relative to the rig.

The plates used in the experiments was extruded aluminium plates (AA6082-T6), with T-stiffeners, joined together with friction stir welds, as discussed in Section 2.2. The exact geometry of the plate is shown in Figure 4-2 (a). An illustration and a photo of the rig is given in Figure 4-2 (b) and (c), respectively. To minimize the friction between the supports and the plate, Teflon plates was used.

Figure 4-1: Test rig for quasi-static experiments

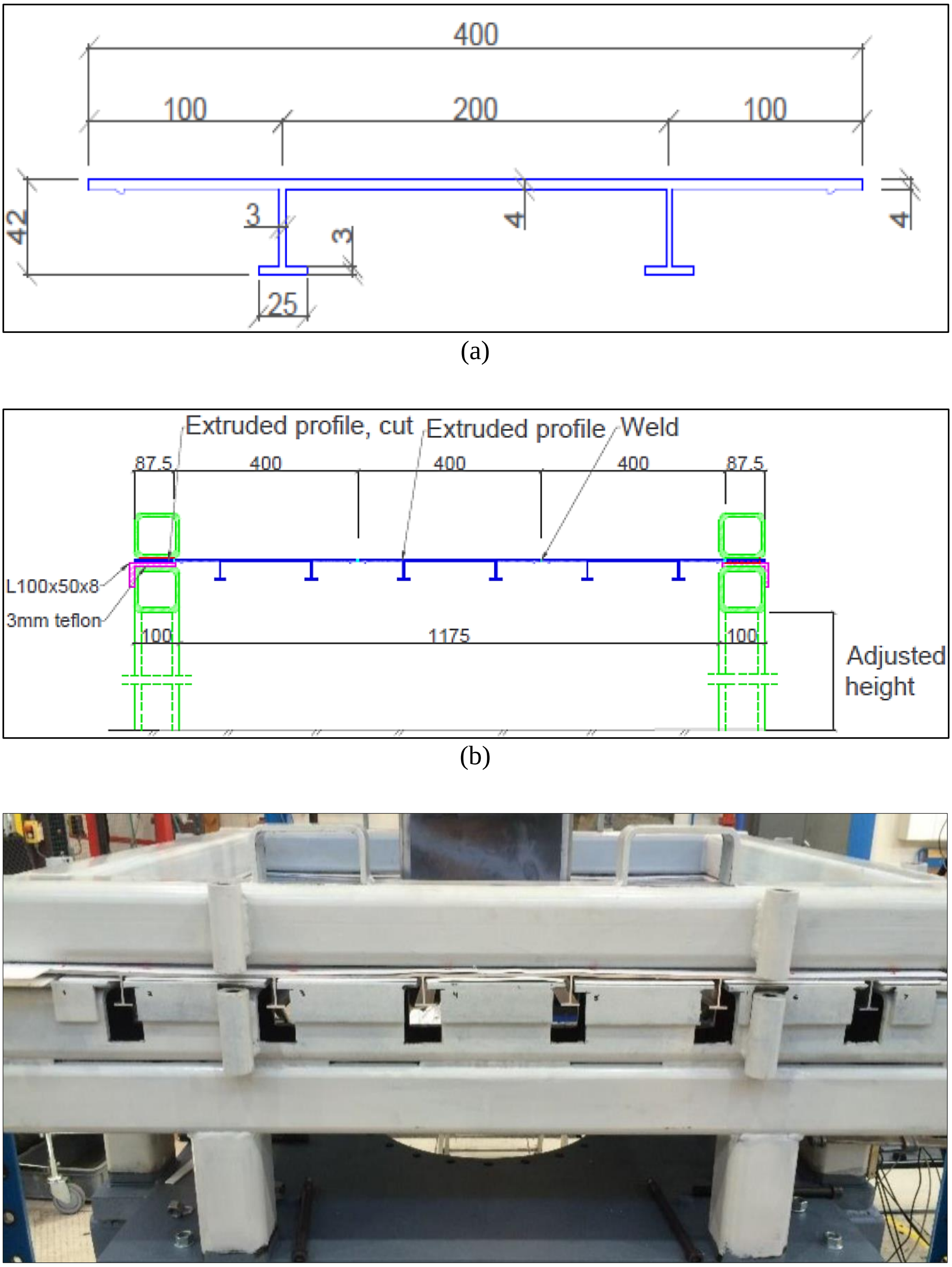

(a)

(b)

(c)

Figure 4-2: (a) Geometry of the extruded profile, (b) Illustration of plate and rig, (c) Photo of rig and indenter

4.2 Numerical simulations of T6-alloy

4.2.1 Model and material

Model

After some modifications on the model used by Kårstad and Skajaa [12], which was handed over by Associate Professor David Morin, a preliminary analysis and validation of the model was performed. The model is displayed in Figure 4-3. Only on quarter of the rig, plate and indenter are modelled due to a symmetric test setup, hence is it possible to save computational time by applying symmetric boundary conditions.

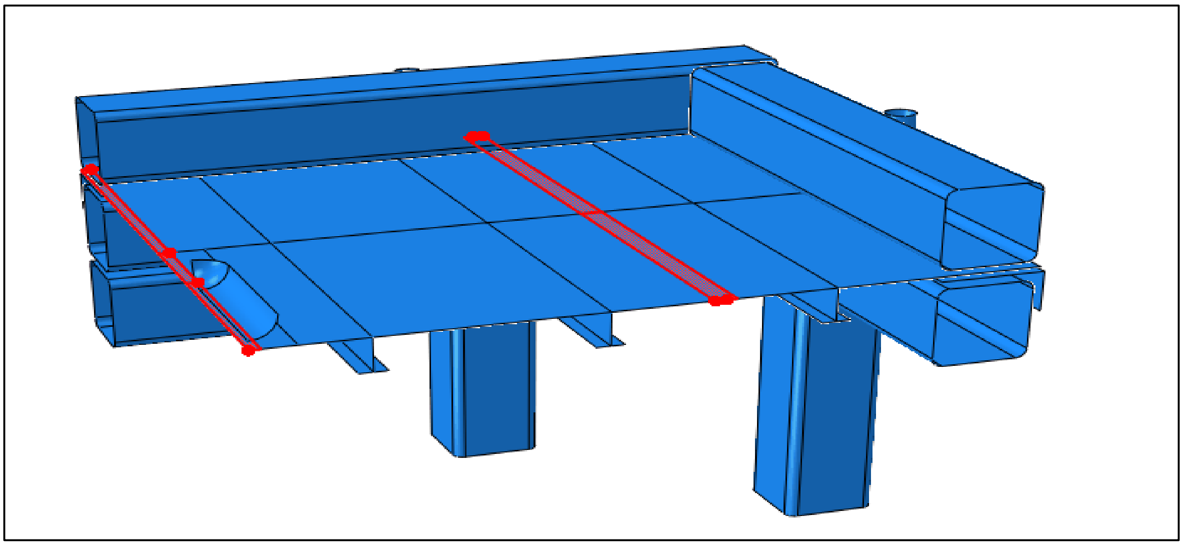

Figure 4-3: Snapshot of the model used in Abaqus/Explicit. Red areas represent the HAZ

The aluminium plates are modelled with S4R shell elements and five integration points throughout the thickness to capture bending. The rig is also modelled as deformable parts with shell elements, while the indenter is a discrete rigid part. Due to the thorough investigation of different nose shapes and sizes by Kårstad and Skajaa [12], it was decided to use a cylindrical indenter with round edges in this thesis. The geometry of the indenter is illustrated in Figure 4-4.

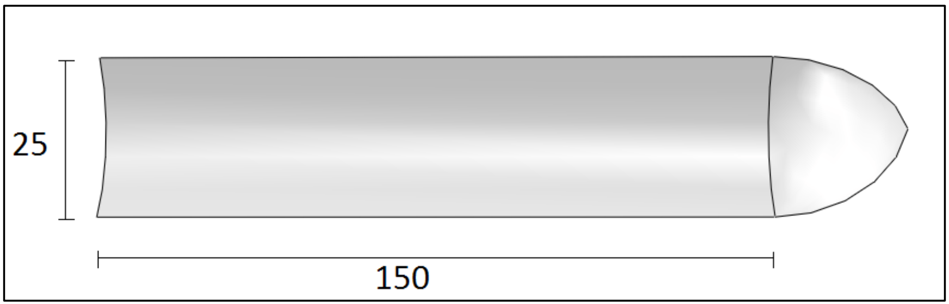

Figure 4-4: One quarter of the hemispherical indenter

To make the model as realistic as possible, the steel bolts in the rig are implemented as beam elements with a circular cross-section. Penalty contact method was enforced for all of the surface-to-surface interactions in the model. In accordance with empirical data [52], the frictional coefficient for the interaction between aluminium and steel was set to 0.61 and

0.74 between the steel parts. In the laboratory tests a Teflon-plate was put between the plate and the rig to ensure that the plate could move with as little friction as possible in the in-plane direction. Because of this, the coefficient of friction between these parts is set to 0.2.

To investigate the effect different loading positions and the direction of the indenter have on the stiffened aluminium plates, there will be completed simulations with the indenter both transversally and longitudinal to the stiffeners. In contrast to Kårstad and Skajaa [12], the indenter will hit on top of a weld, and not in the mid-span. The weld is modelled as a heat affected zone (as discussed in Chapter 2) and will therefore be given its own material properties.

Material

The material used in the numerical simulations is collected from the master thesis of Kårstad and Skajaa [12], and implemented in Abaqus with a material card from SIMLab Metal Model, provided by Associate Professor David Morin (see appendix A). The aluminium alloy used is AA6082, temper T6 with the same chemical composition as given in Table 2-1.

Power law is used to fit a curve to the material parameters, and in all simulations there are used a material density of $2700\,\frac{kg}{m^3}$, and a Poisson's ratio of 0.33. The material is also modelled with a fracture criterion, either with CL or BWH, and a simplified constitutive material model with the von Mises yield criterion. Owing to the fact that failure depends on the ratio between the in-plan size and the thickness of the shell, the mesh size and the thickness of the plate affect the failure criterion implemented through the material cards. Hence, there are implemented suitable material cards for each part of the plate, with different thickness, and for different element sizes. In Table 4-1 some of the key values used in the material card for AA6082-T6 with CL failure criterion are given.

Table 4-1: Key values from the material card for AA6082-T6, estimated with power law (Kårstad and Skajaa, 2015)

	Young´s Modulus (E) [MPa]	**σ_0 [MPa]**	**K [MPa]**	**n**	**W_c [MPa]**
Base	66 000	271.5	439.7	0.0913	62.99
Stiffeners	63 000	238.7	421.6	0.0858	57.44
HAZ	60 000	150	420	0.18	106.61

The profiles that the rig is made up from have the material properties of S355 steel and the bolts of a 12.9 bolt. Both of these materials are modelled as perfectly plastic.

Table 4-2: Material properties for S355 steel and 12.9 steel bolts (Kårstad and Skajaa, 2015)

	Density [kg/m^3]	**Young´s modulus [MPa]**	**Poisson´s ratio**	**Yield stress [MPa]**
S355 steel	7800	210 000	0.3	355
12.9 steel bolt	7800	210 000	0.3	1080

Analytical calculations of the capacity of the rig

To create a picture of what a realistic capacity of the rig is and the order of magnitude, there are performed some basic analytical calculations of the bolts and the supports. The bolts used in the connection between the upper and lower part of the rig are class 12.9 and size M16. The nominal capacity for the bolts in tension and shear is calculated using the following equations, respectively [54]:

$$F_{t,Rd} = \frac{k_2 \cdot f_{ub} \cdot A_s}{\gamma_{M2}} = 137.9\ kN \tag{3-1}$$

$$F_{v,Rd} = \frac{a_v \cdot f_{ub} \cdot A_s}{\gamma_{M2}} = 91.94\ kN \tag{3-2}$$

For a combination of tension and shear, the following equation should be fulfilled [55]:

$$\frac{F_{v,Ed}}{F_{v,Rd}} + \frac{F_{t,Ed}}{1.4 F_{t,Rd}} \leq 1.0 \tag{3-3}$$

The plastic moment capacity for the support, S355 steel, are calculated by the following equation [55]:

$$M_{pl,Rd} = \frac{W_{pl} \cdot f_y}{\gamma_0} = 328.8\ kNm \tag{3-4}$$

From this moment capacity, the maximum force that can be applied to the rig are:

$$F_{Rd} = 1400\ kN \tag{3-5}$$

4.2.2 Results and parametric study

How a plate deforms depend on many different variables, e.g. geometry, boundary and loading conditions. It is important to consider how the plate deflects and what type of deformation that takes place in the system. The plates used in this chapter are positioned between two rectangular hollow sections (RHS) in the rig and can therefore be idealized as simply supported with some rotational stiffness at the ends. An illustration of the deformation during the simulations are given in Figure 4-5.

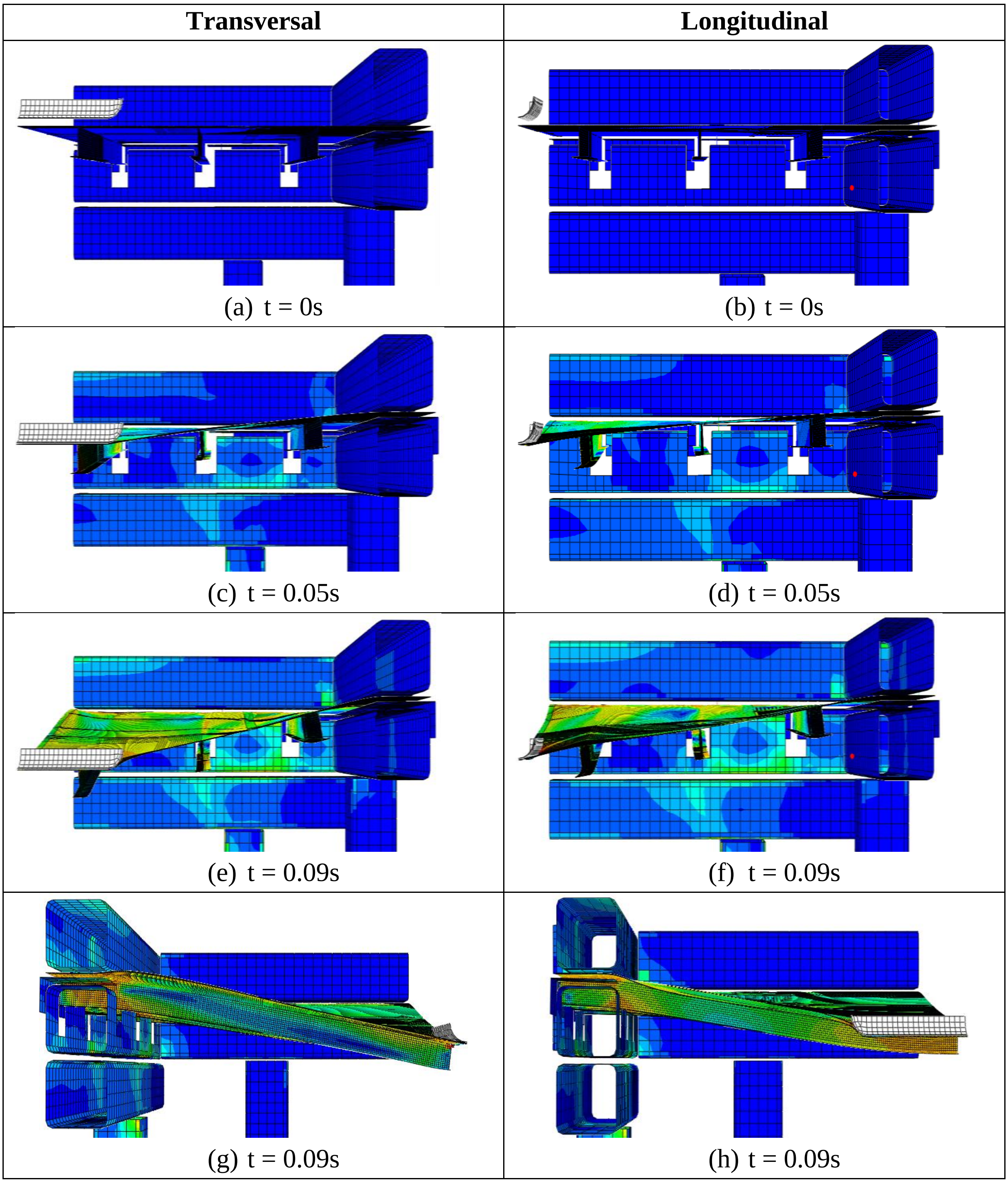

(a) t = 0s (b) t = 0s

(c) t = 0.05s (d) t = 0.05s

(e) t = 0.09s (f) t = 0.09s

(g) t = 0.09s (h) t = 0.09s

Figure 4-5:Deformation of the plate during the simulations
(a),(b) First step | (c),(d) Halfway through | (e),(f),(g),(h) Last step before fracture

The deflection and deformation of the plates are in many ways similar in both of the simulations. In the beginning of the analysis, stresses are localized around the indenter and at the supports. As the indenter moves further down, stresses start to arise in other parts of the plate due to tension. Some instability can also be seen in the stiffeners, i.e. rotation and local buckling of the web. For transversal loading, a large part of the indenter is right above the stiffener and consequently a large fraction of the force will go straight down through the web in to the bottom flange. Eventually the stiffener fails under tension and fracture is initiated in the web. This is however not the case when the indenter is placed along (longitudinal to) the weld. The stresses are in this case lower in the stiffener and higher in the area around the weld, which implies that fracture do not occur in the stiffeners for this particular loading case.

In the last part of the simulations, the stiffeners do no longer contribute to that great of an extent and the increase in capacity is mainly due to plastic deformation of the panels alone. Eventually, the concentration of stresses under the indenter leads to fracture in both of the simulations. When it comes to strength, both loading positions yields approximately the same capacity – but the total deformation is a bit larger in the transversal case.

Mesh size

In an analysis in Abaqus, the size of the mesh may have great effect on the results. A too coarse mesh may have problems describing certain phenomenon, and thus, the results may differ from the exact results, although rest of the model is running properly. An explanation for this is that that a coarse mesh will not detect strain concentrations as well as finer mesh. But as the mesh size decreases, the computational time increases, and it is therefore appropriate to find the mesh size that gives acceptable results with the lowest possible computational time. The running time for the different simulations is shown in Table 4-3.

Table 4-3: Computational time for different mesh sizes and fracture criterions

Mesh size	**Computational time (CL/BWH)**
Equal to thickness	2h 20 min / 2h
1,5 times the thickness	1h / 55 min
2,5 times the thickness	50 min / 50 min
4 times the thickness	20 min / 20 min
5 times the thickness	6 min / 6 min

Figure 4-6 shows the results for both the indenter transversal (a) and longitudinal (b) to the stiffeners, for a mesh size equal to the thickness, 1.5, 2.5, 4 and 5 times the thickness of the plate. The data has been plotted up to final fracture in the plate for both cases. The oscillating part of the force-displacement curve in Figure 4-6 (a) is caused by failure in the stiffener. Note that a mesh scaling factor is implemented with the purpose of initiating fracture sooner due to lower ductility in larger elements.

From these results it is evident that the mesh size on the plate has a noticeable effect on the results when it comes to both maximum force and displacement, and fracture initiation. Especially for the indenter longitudinal to the stiffeners, the maximum force and displacement in the plate decreases considerably with a mesh size equal to the thickness, because fracture is initiated earlier. However, the mesh size has the opposite effect on fracture in the stiffeners, where it initiates earlier for a coarser mesh. An explanation for this might be that smaller elements are needed to describe non-linear behaviour in the stiffeners more accurately.

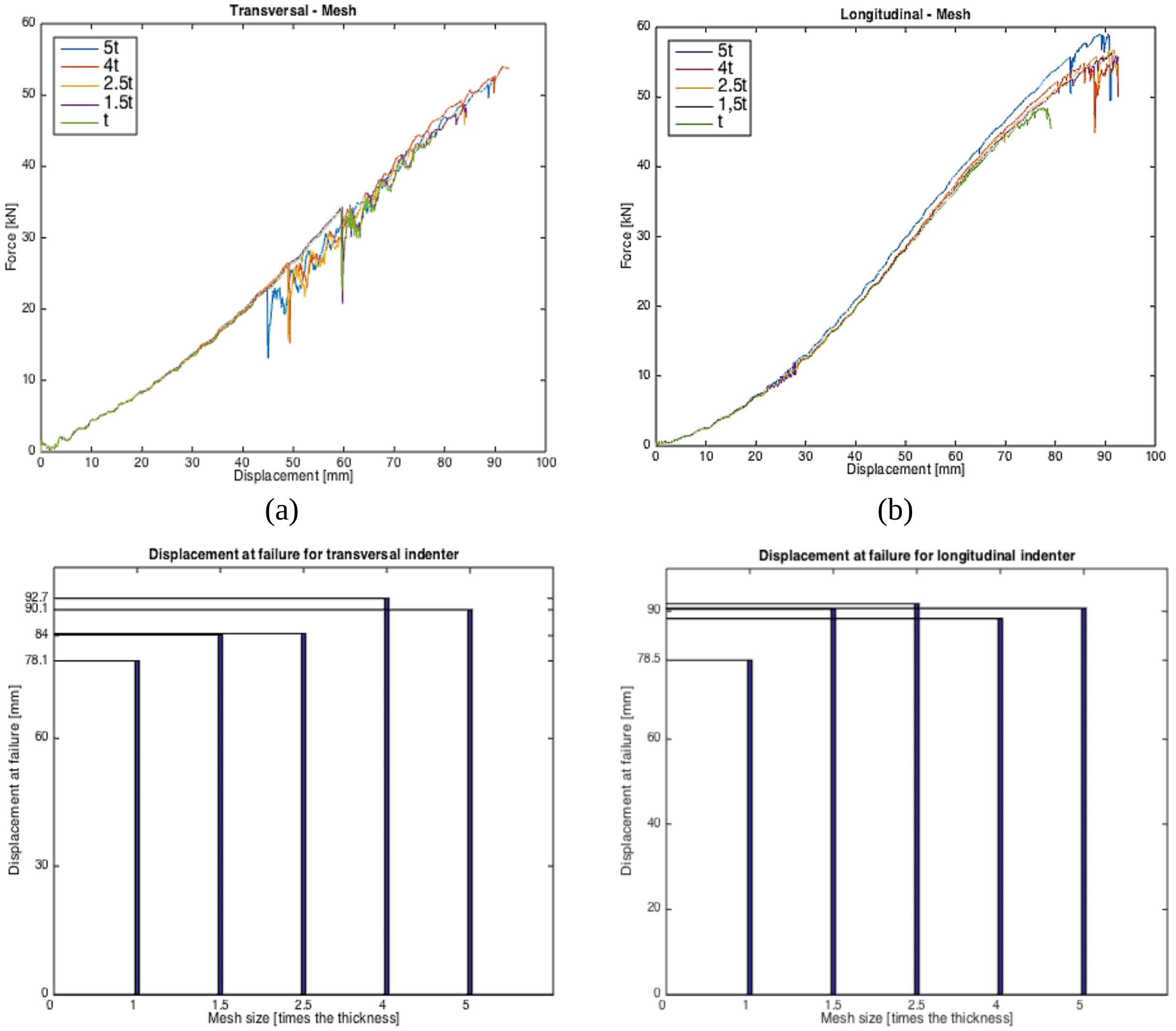

(a) (b)

(c) (d)

Figure 4-6: Force-displacement curves and displacement at failure (CL criterion)
(a),(c) Transversal loading, (b),(d) Longitudinal loading

Fracture criterion

As mentioned previously, the numerical simulations have been carried through with a fracture criterion, both the Cockcroft-Latham fracture criterion and the Bressan-Williams-Hill instability criterion. As Figure 4-7 shows, there is not any noticeable difference between the two criterions for an indenter transversal to the stiffeners, in either maximum force and displacement or fracture initiation. For the case with the indenter longitudinal to the stiffeners, the choice of fracture criterion is more interesting. With the BWH instability criterion the incipience fracture force is lower compared to CL. This is an expected outcome, since the BWH criterion predicts local instability, not final fracture.

The failure modes, illustrated in Figure 4-8, are also different for the two criterions and dependent on the orientation of the indenter. For BWH, a crack propagates perpendicular to the direction of the weld and indenter direction for the longitudinal case (see Figure 4-8 a). Consequently, the plate does not lose all its capacity at once. For the CL fracture criterion however, the crack propagates along the weld, and this leads to immediate and complete failure of the plate (see Figure 4-8 b).

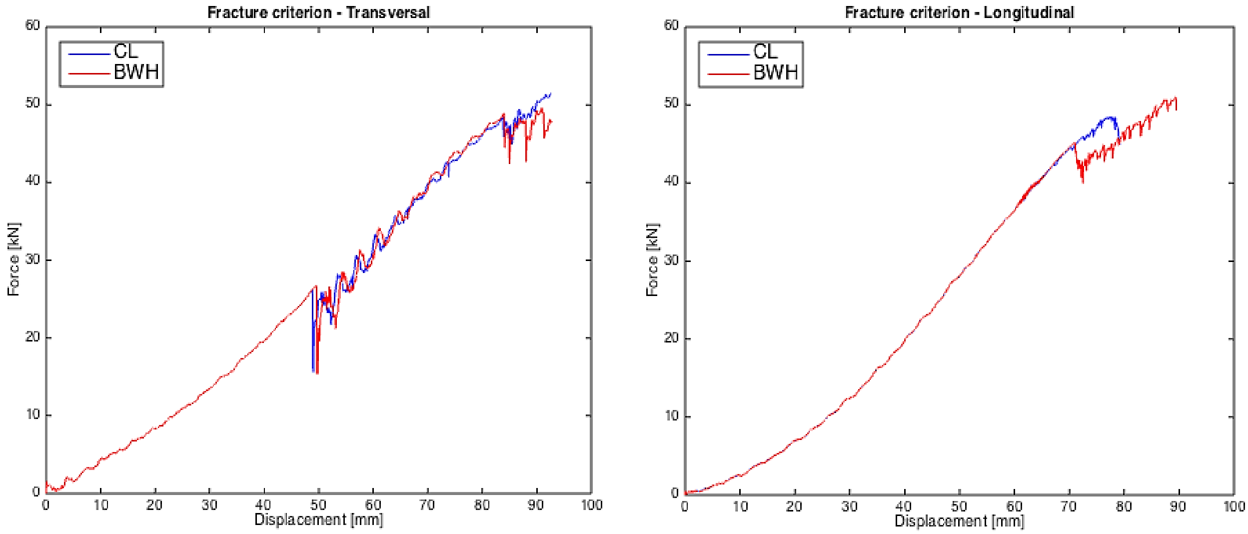

(a) (b)

Figure 4-7: Force-displacement curves for different fracture criterions. (a) Transversal loading, (b) Longitudinal loading

The fracture is initiated approximately at the same time and at the same place in the plate with both criterions when considering transversal loading, which explains the similar curves in Figure 4-7 a. The web of the stiffener fails under tension and this is also captured by both criterions, as illustrated in Figure 4-8 c and d. The BWH instability criterion also predicts failure in the bottom flange of the stiffener – but this does not seem to have any noticeable impact on the force-displacement curve.

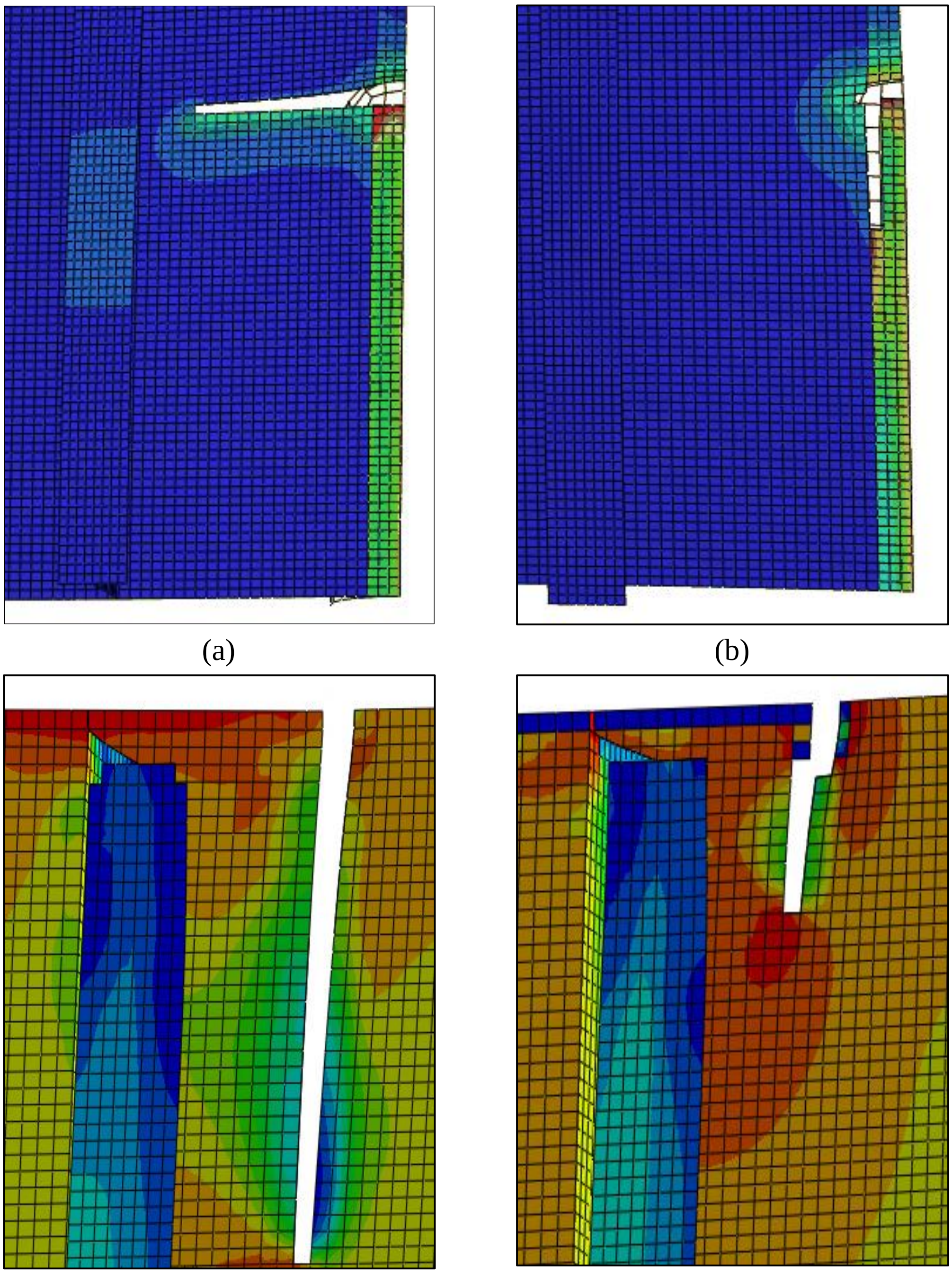
(a) (b)

(c) (d)

Figure 4-8: Failure modes for indenter longitudinal to the stiffeners; (a) BWH, (b) CL Failure modes for indenter transversal to the stiffeners; (c) BWH, (d) CL

An explanation for why the choice of fracture criterion is more interesting for an impact with a longitudinal indenter, compared to the transversal one, may be described by FLDs. With a transversal indenter the fracture will first occur in the flange of the stiffeners, which are subjected to tension, and the fracture will therefore be described by Hill´s theory. When the fracture occurs in the plate however, the fracture is described by the right side of the FLD, and the Bressan-Williams theory. And since the longitudinal indenter only will initiate fracture in the plate, this might explain the difference between CL and BWH in this case.

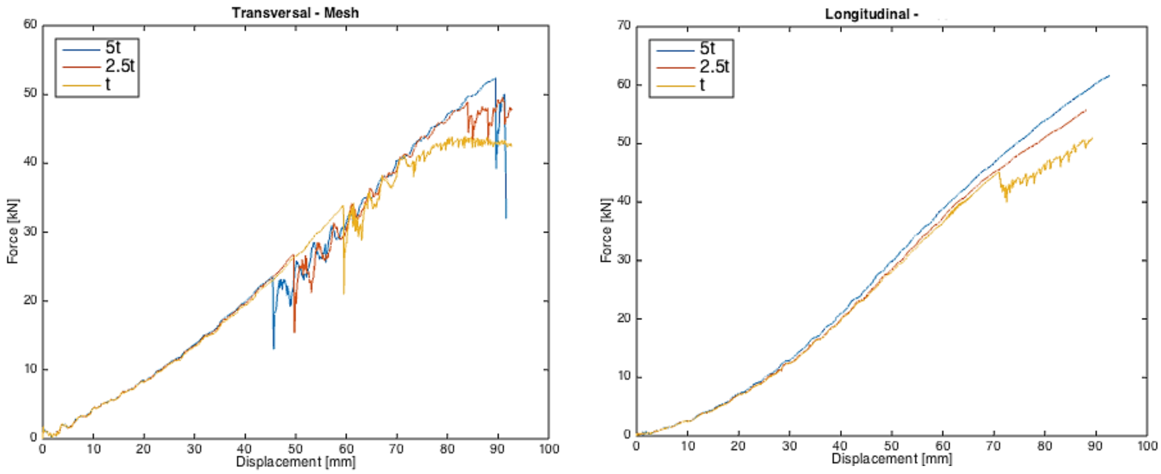

(a) (b)

Figure 4-9: Mesh sensitivity for BWH
(a) Transversal indenter, (b) Longitudinal indenter

To investigate the mesh sensitivity of the two fracture criterions, simulations are run with different mesh sizes with both CL and BWH and the results are displayed in Figure 4-6 a/b and in Figure 4-9 a/b, respectively. Both fracture criterions are implemented with a mesh scaling factor. As the curves illustrate, a coarser mesh yields a higher fracture force - approximately 12 kN or 25% for both criterions. However, the BWH instability criterion is less sensitive to changes of the mesh size if displacement at failure is being considered, which implies that the mesh scaling factor has a slightly more impact on the BWH criterion. In addition to being a less mesh sensitive, the BWH criterion is also less computational expensive compared to CL (see Table 4-3), which may be favourable in a large scale analysis.

Figure 4-10 shows different FLDs for the base material, stiffener material and FSW, where the effect of the mesh scaling factor for BWH is illustrated. Figure 4-10 (d) is a comparison between the different materials with mesh equal to the thickness and shows that the material in the FSW is very different from the base and stiffener material. This can be explained by the value of the power law parameter *n* for the FSW, which differs significantly from the two other materials, and result in a different slope of the curve in the negative quadrant of the FLD.

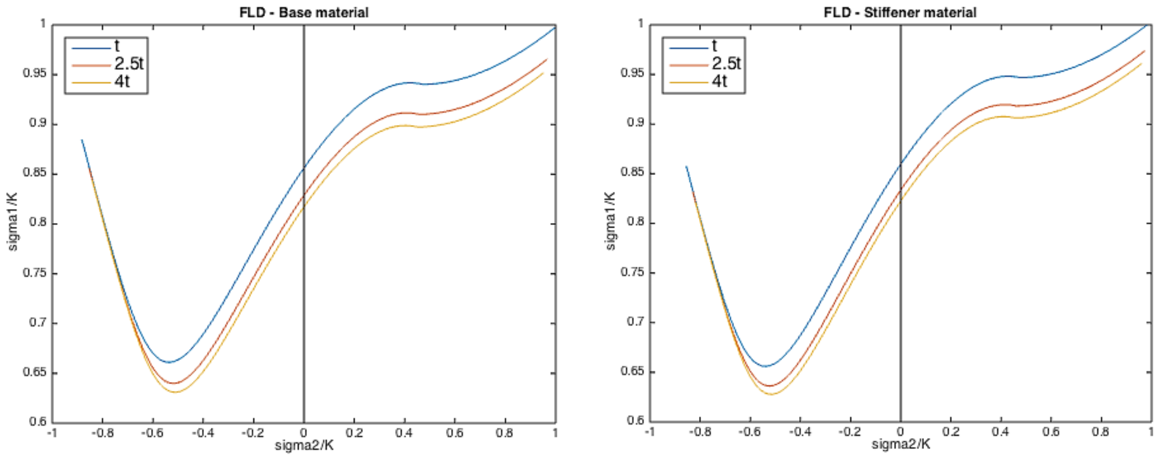

(a) (b)

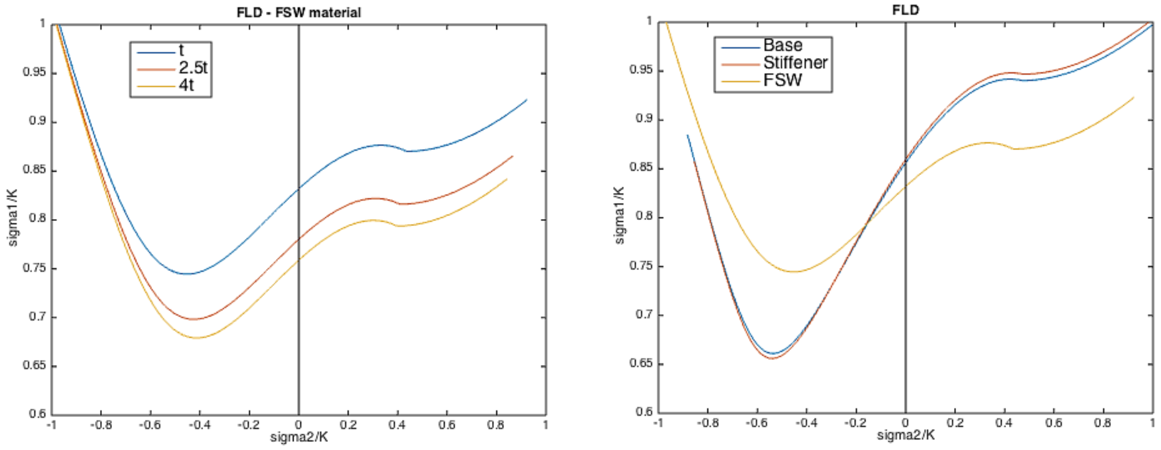

(c) (d)

Figure 4-10: FLDs for (a) Base material (b) Stiffener material (c) FSW material (d) Comparison of the three materials with mesh size equal to the thickness

<u>Friction</u>

The friction coefficient between Teflon and aluminium was found to be 0.19, and to investigate the effect of the low friction due to the Teflon, a parameter study with different coefficients was conducted. In Figure 4-11 (a) the force-displacement curves for different friction coefficients are displayed. As the plots indicate, the forces in the plate increases with a higher friction coefficient. A physical explanation for this is that a lower friction coefficient allows for more sliding between the supports and the plate, which again reduce the force necessary to deform the plate.

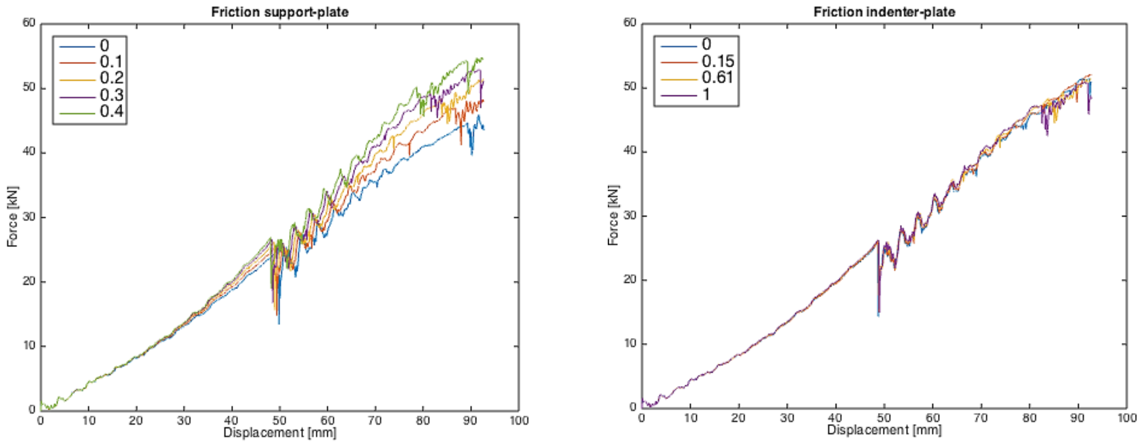

(a) (b)

Figure 4-11: Force-displacement curves for different frictions coefficients between: (a) support and plate (b) indenter and plate

The effect of the friction between the indenter and plate is also investigated, and force-displacement curves for different friction coefficients are illustrated in Figure 4-10 (b). From the curves it is evident that the difference in friction between the indenter and the plate is negligible, when it comes to both maximum force and displacement. However, for a friction coefficient close to zero between the indenter and plate, fracture will not initiate in the plate at all.

Hardening rule

As mentioned in Section 2.4.3, two different isotropic hardening rules, the power law and Voce rule, will be studied in this report. Power law is used as standard in our simulations, but to study what effect a different hardening rule has on the results, some simulations was run with the 2-term Voce rule. The necessary material data and parameters were collected from tensile tests carried out by Kårstad and Skajaa [12] and are given in Table 4-4.

Table 4-4: Key values from the material card, estimated with Voce rule

	σ_o [MPa]	Q_{R1} [MPa]	C_{R1}	Q_{R2} [MPa]	C_{R2}
Base	271.5	17.78	2058	90	15
Stiffener	238.7	36.65	1727	86	17
HAZ	150.0	30.00	220	130	40

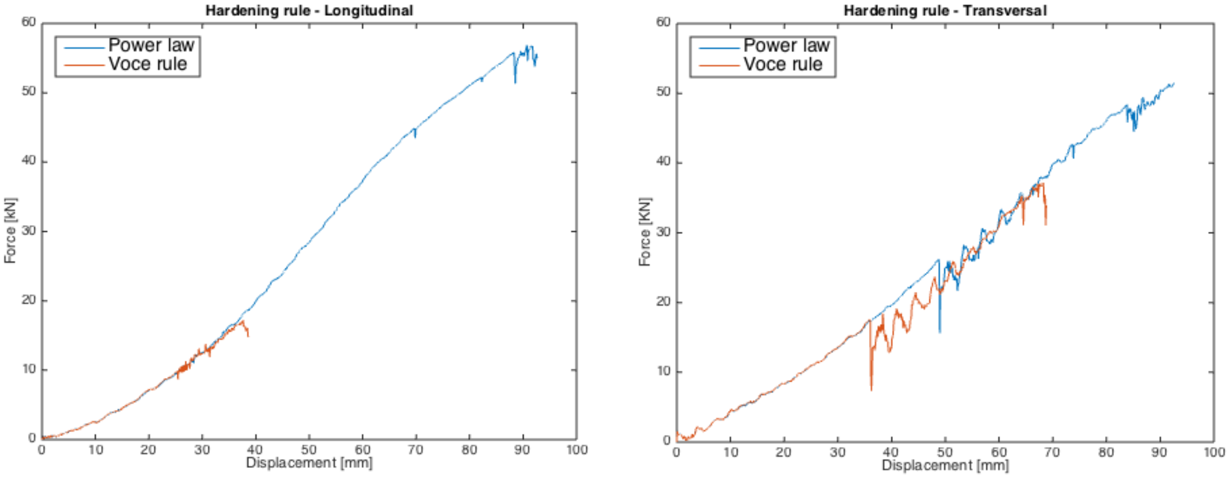

(a) (b)

Figure 4-12: Force-displacement for different hardening rules: Longitudinal loading (b) Transversal loading

The results from the simulations with Voce rule are compared to equivalent simulations with power law in Figure 4-12. It is clear for the curves that the choice of hardening rule has big influence on the capacity of the plate. Fracture initiates for a much lower force when the Voce rule is implemented. The difference is clear for the longitudinal case, where the estimated force at fracture is over three times as big for the analysis with power law. The reason for this large aberration could be explained by the extrapolation of the stress-strain curve (see Figure 4-13). The differences between the two hardening rules are pretty clear for larger strains, especially for the weld. Maximum equivalent plastic strain in the heat affected zone with longitudinal indenter is approximately 0.33 (as illustrated in Figure 4-14 (a)) and the difference in estimated stress for the two hardening rules are already clear at that point. The 2-term Voce rule predicts fracture at a much lower value of stress than the power law, and since the impact area is above the weld – the capacity is strongly dependent on the material properties of the HAZ.

The fact that the difference in the extrapolated stress-strain curves are largest for the HAZ are the reason why the results between the two hardening rules are clearest for longitudinal loading, where fracture will occur in the weld.

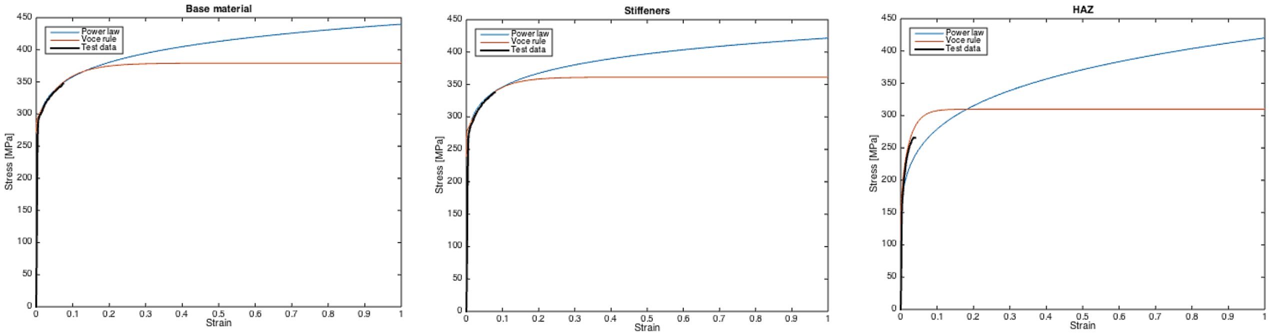

(a) (b) (c)

Figure 4-13: Stress-strain curves for different hardening rules *for:*

(a) Base material (b) Stiffener material (c) HAZ

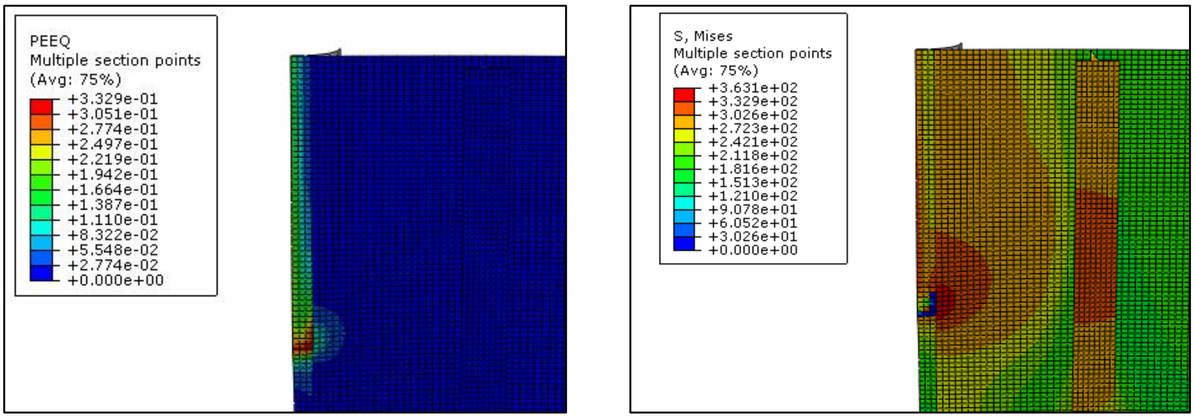

(a) (b)

Figure 4-14: (a) Equivalent plastic strain in weld last step before fracture

(b) Von Mises stress in weld last step before fracture

From Figure 4-13, it may be appropriate to think that the Voce rule will give the best estimate of the work hardening, since the power law seems to overestimate the stress-strain relationship. Even though there is not any similar experimental data to compare the numerical results with, it is clear from Figure 4-12 that power law yields the best results after all.

It is reasonable to assume that the force at fracture will decrease with approximately the same ratio as the difference between yield strength in the base material and the HAZ when indenter has been moved from the mid-span to the weld. In the test done by Kårstad and Skajaa [12], with the indenter between the stiffeners, the fracture force was approximately 150 kN. The yield strength in the base material is 271.5 MPa and 150 MPa in the HAZ, which yields a ratio of 0.55. With this in mind, power law clearly gives a much better estimation for this particular loading condition, and is therefore used as hardening rule in the following section as well.

4.3 Numerical simulations with the T4-alloy

4.3.1 Model and material

In addition to simulations of the AA6082-T6 plates in the previous section, it has also been carried out simulations with the T4-alloy in order to compare the results with the tests carried out by Kårstad and Skajaa [12]. Consequently, the numerical model is nearly identical to the one used in their analysis. After a discussion with our supervisors it was decided to model the plate without any heat affected zones, as the impact area no longer was above a weld – but in the mid-span between the stiffeners (see Figure 4-15).

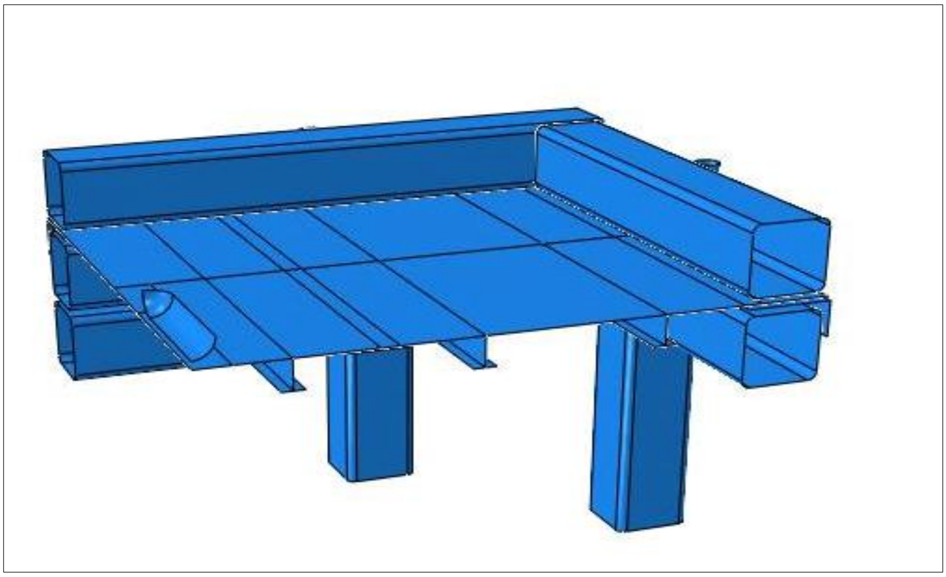

Figure 4-15: Abaqus model used in the analysis of the T4-alloy.

Table 4-5: Key values for AA6082-T4

	E [MPa]	σ_0 [MPa]	K [MPa]	n	ρ $[\frac{kg}{m^3}]$	ν
AA6082-T4	70 000	111	430	0.25	2700	0.33

In Section 2.1, the different temper designations were discussed, and the most evident differences between T4- and T6-alloys can be seen in ductility and strength. Due to natural ageing, it is reasonable to expect that T4-treated alloys allow for more plastic deformation than T6-alloys, but a consequence of this is lower strength. Key material properties are given in Table 4-5. To investigate the effect of these material differences, a small parametric study of the T4-alloy is conducted in the next section, where the results will be compared to the numerical results from Kårstad and Skajaa.

4.3.2 Results and parametric study

The deformation pattern in the T4-plate is in many ways similar to what we observed for the T6-plate in Section 4.2.2, but due to different material properties in the plates and different loading positions, the overall response and capacity differ considerably from the T6-plates. An illustration of the deformation in the simulations are given in Figure 4-16.

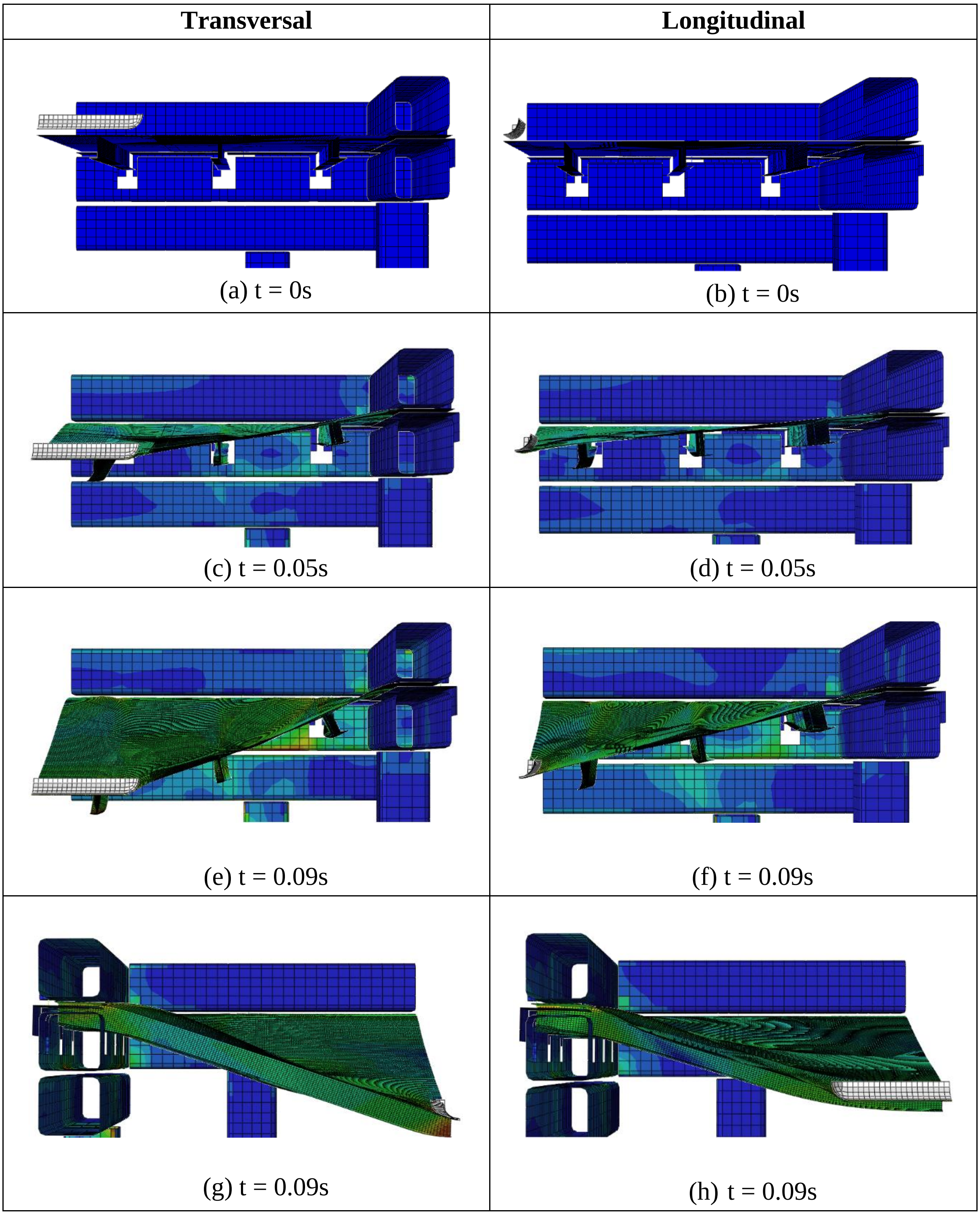

(a) t = 0s
(b) t = 0s
(c) t = 0.05s
(d) t = 0.05s
(e) t = 0.09s
(f) t = 0.09s
(g) t = 0.09s
(h) t = 0.09s

Figure 4-16: Displacement for T4-plate during the simulations
(a),(b) First step | (c),(d) Halfway through | (e),(f),(g),(h) Last step before fracture

In the first phase of the impact, stresses are localized around the indenter in the mid-span and at the supports. Gradually stresses start to arise throughout the plate and the plastic deformation causes the web in the T-stiffener to deflect. Fracture is however not initiated in the stiffeners in neither of the simulations, because the material is too ductile. As the indenter moves further down, it is obvious that a considerably amount of the energy has been absorbed through plastic deformation of the stiffeners. Lateral displacement and rotation of the stiffener have caused noticeably changes to the initial form and geometry of the plate. Eventually, the concentration of stresses under the indenter leads to fracture in both of the simulations.

The overall deflection is larger for the transversal case, which yields a slightly higher capacity than for the longitudinal case. This difference in capacity can be explained by the fact that the utilization of the stiffener is better in the transversal case, where part of the indenter is placed right above the stiffener.

Mesh size

The mesh size has the same effect on the results for the T4-plate as we observed for the T6-plate. As the curves in Figure 4-17 illustrate, the estimated fracture force increase noticeably with a coarser mesh, especially in the transversal loading case. A very coarse mesh will not detect fracture for either of the loading directions, even for very large displacements.

To investigate the mesh sensitivity of the two fracture criterions, simulations are run with both CL and BWH for different mesh sizes and with a mesh scaling factor. As the results illustrate, BWH yields better correlation between the mesh sizes than CL, when both force and displacement at failure are being considered. It is therefore reasonable to assume that the mesh scaling factor has a greater influence on the BWH instability criterion and that it is less sensitive to changes of the mesh size than the CL fracture criterion.

When it comes to run time, the simulations with BWH are slightly faster and less computational expensive than CL when finer mesh are being used in the analysis, as shown in Table 4-6. Since the plate is modelled without welds, the analysis is expectedly less demanding than the T6-analysis that was carried through in Section 4.2.2.

Table 4-6: Computational time for different mesh size and fracture criterions

Mesh size	**Computational time (CL/BWH)**
Equal to thickness	2h 5 min / 1h 55 min
2 times the thickness	55 min / 50 min
4 times the thickness	15 min / 15 min

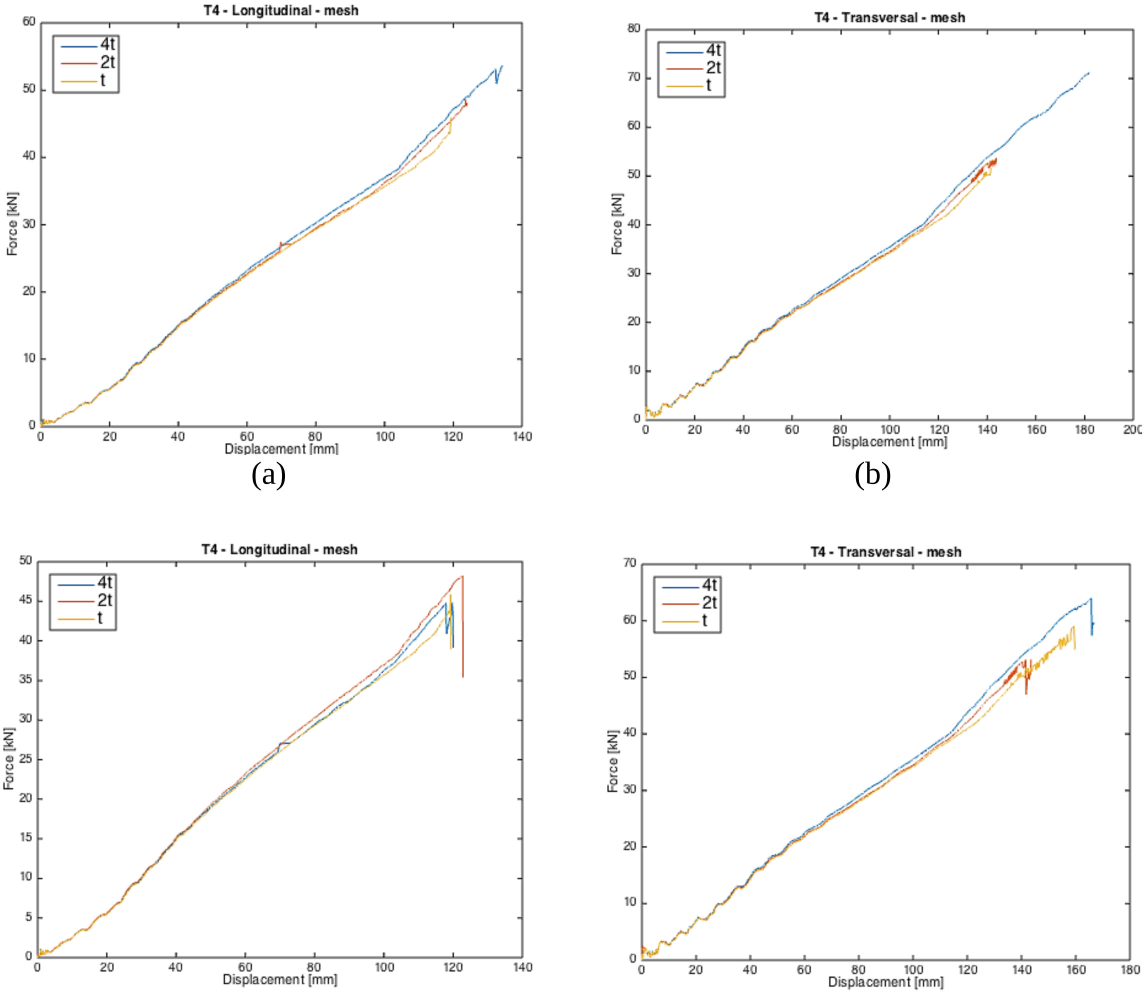

(a) (b)

(c) (d)

Figure 4-17: Force-displacement curves for different mesh sizes and fracture criterion
(a) Longitudinal (CL), (b) Transversal (CL)
(c) Longitudinal (BWH), (d) Transversal (BWH)

<u>Fracture criterion</u>

As emphasized in Section 4.2.2, the initiation of fracture in the T6-plate was strongly dependent on the loading direction and what type of fracture criterion that was implemented. This is not the case for the T4-alloy, where fracture only occurs in the plate and not in the stiffeners, as illustrated for BWH in Figure 4-18. The estimated force and displacement at fracture are also virtually equal for the two criterions in both loading directions, as illustrated in Figure 4-19. A small aberration is seen in incipient fracture force, but this is expected, because BWH defines local instability, not final fracture.

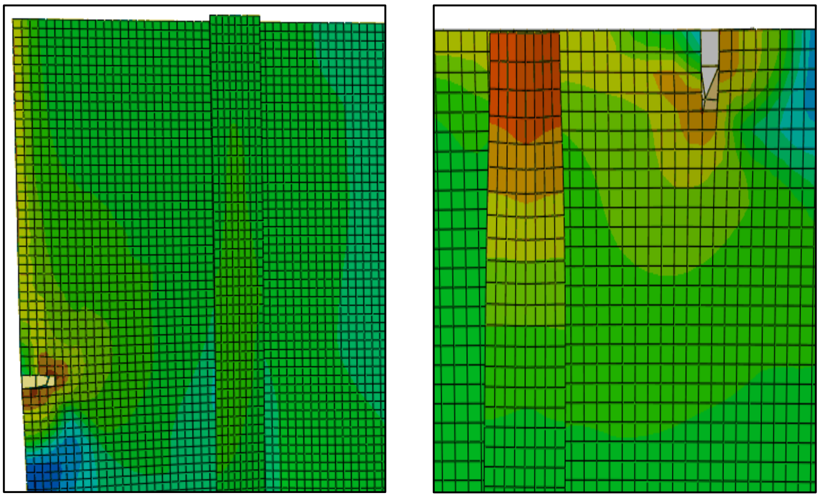

(a) (b)

Figure 4-18: Failure in plate with BWH; (a) Longitudinal loading, (b) Transversal loading

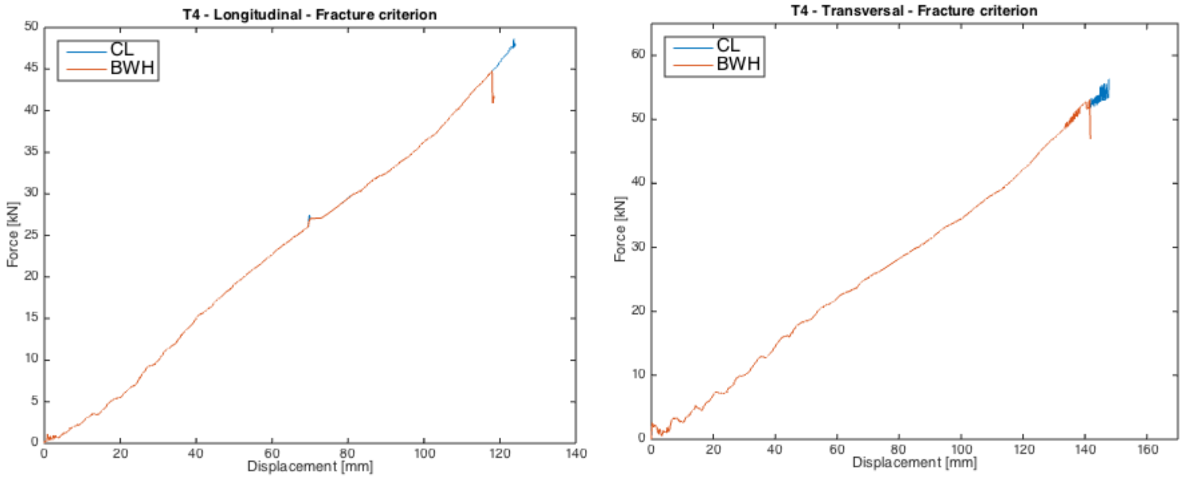

(a) (b)

Figure 4-19: Force-displacement curves for different fracture criterions.
(a) Longitudinal loading (b) Transversal loading

Friction

The same behaviour that was observed in the study of friction coefficients for the T6-plate can also seen for the T4-alloy. Lower friction between support and plate yields lower forces and stresses in the plate (see Figure 4-20a), since it allows for more sliding between the parts. However, in the simulation with frictionless contact, fracture do not occur in the plate at all. The stresses in the plate are simply not high enough to initiate fracture.

The friction between the indenter and the plate is less sensitive to changes and yields approximately the same results as long the friction coefficient is not zero (see Figure 4-20b), in which case fracture do not occur in the plate at all.

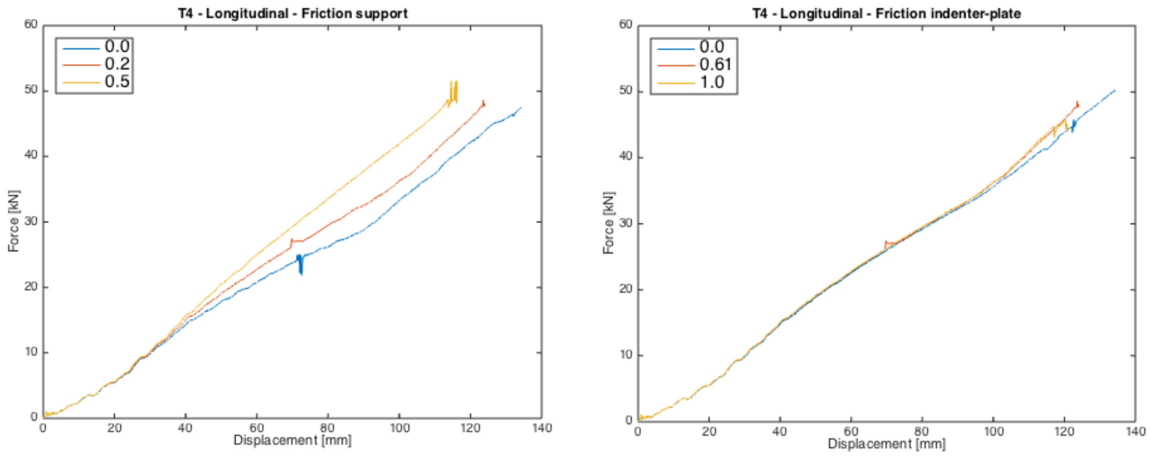

(a) (b)

Figure 4-20: Force-displacement curves for different friction coefficients between: (a) Support and plate (b) Indenter and plate

4.3.3 Comparison with T6-analysis by Kårstad and Skajaa

Since the model used for the numerical analyses of the T4-alloy is almost identical as the one used by Kårstad and Skajaa [12], it is interesting to look at what differences the material properties between T4 and T6 does to the overall response and capacity of the plates.

The differences are fundamental, which is clear from Figure 4-21. The artificial ageing of the T6-alloy gives higher strength, which yields a fracture force that is 3-5 times higher, depending on the loading direction, than for the T4. On the other hand, the T6-alloy loses some of the ductility and it is therefore more brittle. Because T4-plates are softer, the in-plane stiffness is reduced, and the displacement at failure is approximately a ratio of 1.7 higher than for the T6-plates. Hence, the overall plastic deformation is larger in the T4-plate.

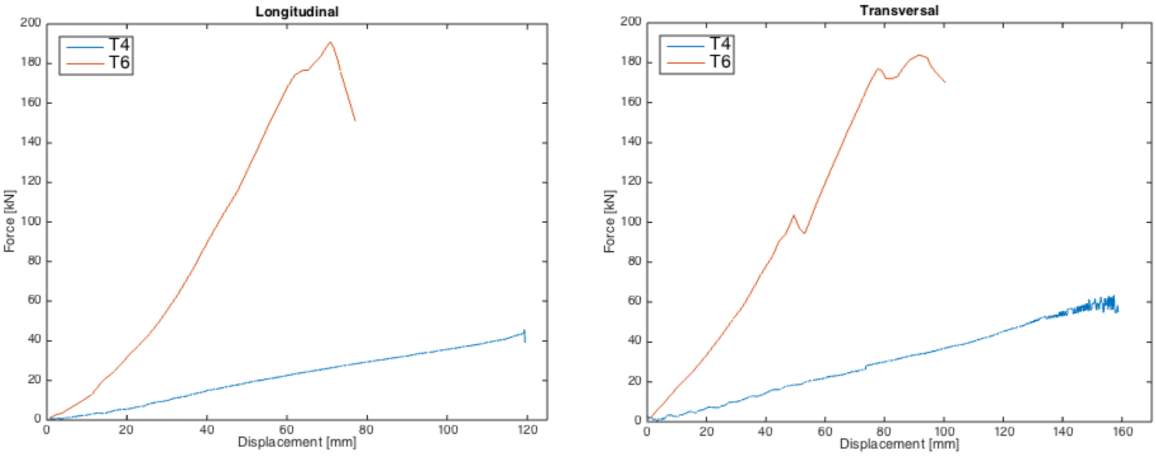

(a) (b)

Figure 4-21: Force-displacement curves for T4 and T6

(a) Longitudinal direction (b) Transversal direction

Even though failure do not occur in the stiffeners, there are some other interesting aspects with the stiffeners in the T4-plates. The large deflection caused by the indenter lead to buckling several places in the plate, as Figure 4-22 illustrates. Buckling is a highly non-linear problem that comes from instability in relatively long and slender material sections without any stiffening. Local buckling may increase the possibility of premature collapse of the plate and thus, the capacity may decrease. This phenomenon is seen in both the T4- and the T6-plate, but to a much greater extent in the former. Some photos of the T4-model are provided in Figure 4-22 to show how part of the plate deforms during the simulation.

It is noteworthy that in the simulations of the T4-plates, idealisations were made to simplify the analysis and the results should therefore be studied with precaution. Because the same material properties were assigned to all parts of the plate and that no HAZ was implemented in the model, it is reasonable to think that a simulation with a more accurate material card will give the same or even lower estimate of the capacity.

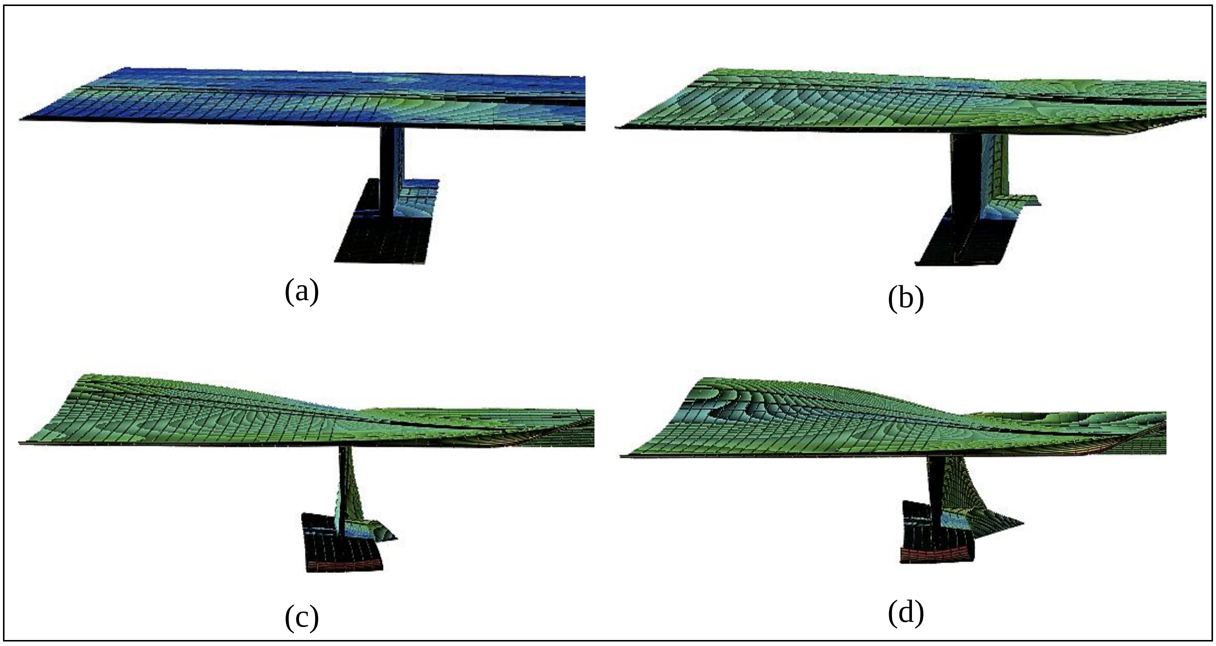

Figure 4-22: Part of the T4-plate under transversal loading after: (a) 0 s (b) 0.04 s (c) 0.06 s (d) 0.08 s

5. Conclusion and proposal to future work

5.1 Impact loading of plate from Dr. Ing thesis

The numerical models presented in Chapter 3 yields acceptable estimates when compared to the data from the experimental tests carried out by Hildrum in her Dr.-Ing thesis. The failure modes from the experiments are particularly well captured and described in the simulations. However, the estimated force and displacement at failure do vary in accuracy. Five of the total six models overestimate the capacity, of which the model used for setup A1 were the only one to give a conservative estimate. For the simulations where the impact is above or next to a stiffener, and the stiffeners constitute a large part of the capacity, the numerical model yields a too soft response.

The plate is modelled without a welding zone, but Hildrum found noticeable differences in strength between the base material and the HAZ. The yield strength in the HAZ was a ratio of 0.64 lower than the yield strength in the base material. With this in mind, to implement a HAZ with its own material properties would definitely influence the results for setup A, where the impact is right above a weld. In addition to the differences in material properties between the HAZ and the base material, other research suggests that different material properties in the stiffeners and the top flange are common in extruded aluminium profiles [53]. Due to this fact, a slightly softer material was implemented in the stiffeners, and this resulted in better estimation in both the elastic and plastic regime, as well as initiation of fracture.

Despite different material in the stiffeners, the numerical model did not capture the sudden increase in the stiffness when the yield strength is exceeded, that was detected in the experimental tests. This indicates that the simplified material model with the von Mises yield criterion may not be good enough to handle plasticity in a sufficient way, and it could therefore be interesting to implement an anisotropic yield criterion to study how that would affect the results.

Proposal for future work:

- Implement an anisotropic yield criterion in the numerical simulations and study how this affect the accuracy of the numerical estimations.
- Model the plate with own material properties for the HAZ and the stiffeners.
- Conduct static tests of the same plate, but in a different rig – that is, with different boundary conditions – to study how this affects the capacity and the response of the plate.

5.2 Impact loading of T4- and T6-plates

In the preliminary analysis for the AA6082 alloy, some interesting points about the two fracture criterions were observed, e.g. the difference in efficiency and mesh sensitivity. BWH yields a better coherence between different mesh sizes than CL, especially when it comes to displacement at failure. A mesh size close or equal to the thickness of the element should be used when CL is implemented, which coincide well with the results from parametric study that Kårstad and Skajaa did [12]. BWH is also less computational expensive, which makes it more favourable in a large scale analysis, for both the T4- and T6-alloy.

Two different hardening rules, the Voce rule and the power law, were used to estimate the implemented material. The results from the two hardening rules differs significantly when it comes to predictions of the load level at failure and thus the capacity. Voce rule predicted failure at an unnaturally low fracture force for the longitudinal loading direction, and this shows the importance of calibrating the hardening parameters properly – especially in parts of the structure where fracture is likely to occur. The Voce parameters were in this case not calibrated precise enough and it is reasonable to believe that the power law gave a more realistic and better estimation of the stress-strain behaviour in HAZ.

The expected differences between T4 and T6, due to the difference in material properties and behaviour, are clearly captured by the numerical models. A lot of the same effects that was put to light in the preliminary analysis for the T6-alloy were also found for T4-alloy, but with some exceptions. For the T6-alloy, the difference between BWH and CL was close to negligible for the transversal loading, where fracture first is initiated in the stiffeners. For the case with longitudinal loading and fracture in the plate, the difference was much clearer, especially when it comes to describing the failure modes. With the T4-alloy, fracture did not initiate in the stiffeners for a transversal load. The difference between CL and BWH was also smaller for this heat treatment.

On the basis of the numerical modelling in the preliminary analysis of the two different AA6082 alloys, it is concluded that T6 is the best choice for aluminium panels exposed to impact loads. The foundation for the conclusion is the higher strength, which gives it a wider range of application, even though the ductility in a T4 alloy is higher. T4-treated aluminium alloys might not be in a fully stable condition in room temperature and some of the material properties may therefore change over time.

The impact tests conducted in the Dr. Ing- thesis of Hildrum and in the preliminary analysis in this thesis are not identical, but they have some similarities that makes it possible to compare the behaviour of the two aluminium plates. The tests have some differences when it comes to the geometry, boundary conditions and shape of indenter, but the test setup in this thesis, for longitudinal loading, is in many ways similar to the test with the indenter between stiffeners (setup A2) carried out by Hildrum.

Even though there are used an AA6082-T6 alloy in both tests, there are some aberrations between the materials. As Figure 5-1 (a) illustrates, the base material used by Hildrum has higher strength. However, the capacity is higher for the plate used in the preliminary analysis, as illustrated in Figure 5-1 (b). In a direct comparison, the setup used in the preliminary analysis yields a softer response than setup A2, but it allows for more plastic deformation and thus, more energy is absorbed and the capacity is higher.

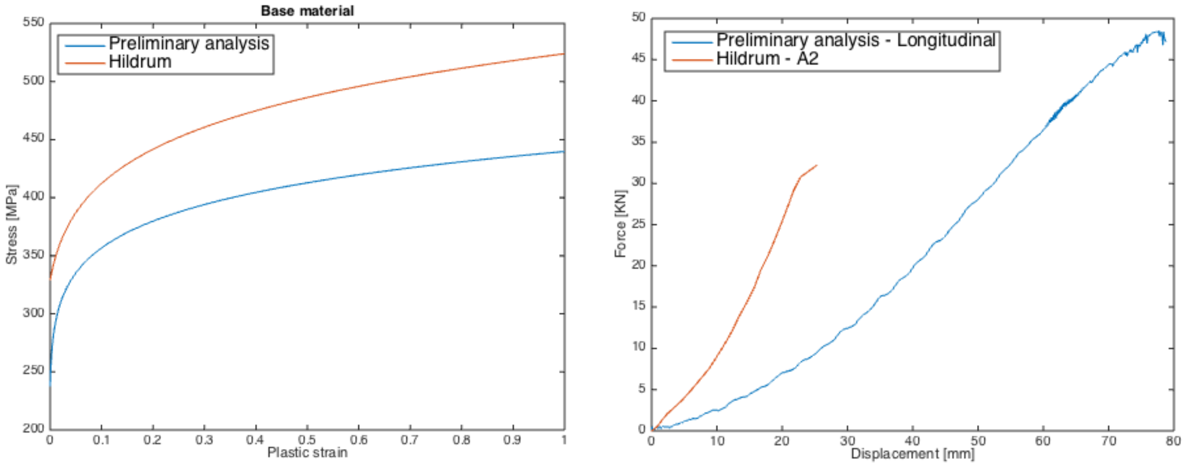

(a) (b)

Figure 5-1: Comparison between the preliminary analysis and results from Hildrum:
(a) Stress-strain curve for the base material
(b) Force-displacement curve (CL criterion, mesh size equal to thickness)

Proposal for future work:

- Conduct static tests of the T6-plate with impact above the weld.
  Compare the experimental and numerical results and validate the finite element model.

- Conduct static tests of the T4-plate with impact between the stiffeners and validate the finite element model. Compare the results with experimental data from the tests carried out by Kårstad and Skajaa on the T6-plate.

- Implement an anisotropic yield criterion in the numerical simulations and study how this affect the accuracy of the numerical estimations.

- Investigate how the geometry of the stiffeners affect the behaviour and the capacity of plates subjected to impact loads, e.g. the difference between T- and L-stiffeners.

Appendices

Appendix A

In this appendix, relevant MATLAB codes are provided. This includes codes for creating material cards with both the CL-criterion and the BWH-criterion

A.1 MATLAB code for generating material card with CL-criterion

```
clc
clear all
%%------------------------------------------------------------
-----------%%
% Define material constants
%%------------------------------------------------------------
-----------%%
rho    = 2.7e-9; %Density
E0     =  70000; %Young's modulus
nu     =    0.3; %Poisson's ratio
sigma0 =    280; %Yield stress
K      =    400; %hardening modulus
n      =    0.2; %hardening exponent
%%------------------------------------------------------------
-----------%%
% Define element shape
%%------------------------------------------------------------
-----------%%
leote = 1.0; %ratio between the in-plane size and the
thickness of the shell
%%------------------------------------------------------------
-----------%%
% Compute the stress-strain curve
%%------------------------------------------------------------
-----------%%
pmax       =  1.0; %maximum plastic strain
npoints    = 1000; %number of points in the stress-strain
curve
p          = (0:0.001:1)';
npoints    = npoints+1;
epsp0      = (sigma0/K)^(1/n);
model(1,1) = sigma0;
for i=2:npoints
   model(i,1) = K*(epsp0+p(i))^n;
end
%%------------------------------------------------------------
-----------%%
% Compute failure model
%%------------------------------------------------------------
-----------%%
%%%%%%%%%%%%%%%%%%%%%%%%%%%%%%%%%%%%%%%%%%%%%%%%%%%%%%%%%%%%%%
%%%%%%%%%%%%%
% define stress triaxiality and Lode parameter
%%%%%%%%%%%%%%%%%%%%%%%%%%%%%%%%%%%%%%%%%%%%%%%%%%%%%%%%%%%%%%
%%%%%%%%%%%%%
T = -0.33:0.01:0.66;
p =  0:0.001:1.0;
for i=1:length(T)
    % lode parameter
```

```
    if(T(i)<-0.333)
        L(i) = -3/(9*T(i)^2-1)*(1-sqrt(12*T(i)^2-27*T(i)^4));
    elseif(T(i)<0 && T(i)>=-0.333)
        L(i) =  sqrt(27*T(i)^2/(4-9*T(i)^2));
    elseif(T(i)<0.333 && T(i)>=0)
        L(i) =  -sqrt(27*T(i)^2/(4-9*T(i)^2));
    else
        L(i) = 3/(9*T(i)^2-1)*(1-sqrt(12*T(i)^2-27*T(i)^4));
    end
end
en  = 2.0*n;
ef  = n+(en-n)/leote;
Wc  = K*(ef)^(n+1)/(n+1);
for i=1:length(T)
   pf(i) = ((n+1)*Wc/(K*max(0,T(i)+(3-
L(i))/(3*sqrt(3+L(i)^2)))))^(1/(n+1));
end
%%--------------------------------------------------------------
-----------%%
% Plot results
%%--------------------------------------------------------------
-----------%%
subplot(1,2,1)
plot(p,model)
axis([0 max(p) 0 max(model)])
xlabel('Equivalent plastic strain')
ylabel('Equivalent stress (in MPa)')
grid on
subplot(1,2,2)
plot(T,pf)
axis([-0.2 0.67 0 1.0])
xlabel('Stress triaxiality')
ylabel('Equivalent plastic strain')
grid on
%%--------------------------------------------------------------
-----------%%
% Export material card
%%--------------------------------------------------------------
-----------%%
fich=fopen(['mat_' num2str(leote) '.inp'],'w');
% Add material
fprintf(fich,'*Material, name=SMM_AA6082-T6\n');
% Add Density
fprintf(fich,'*Density\n');
fprintf(fich,'%6d\n',rho);
% Add Elasticity
fprintf(fich,'*Elastic\n');
fprintf(fich,'%6d,%6d\n',E0,nu);
% Add plasticity
fprintf(fich,'*Plastic\n');
for i=1:length(p)
```

```
    fprintf(fich,'%6d,%6d\n',model(i),p(i));
end
% Add fracture model
fprintf(fich,'*Damage Initiation, criterion=DUCTILE\n');
fprintf(fich,'%6d,%6d\n',1000,-0.67);
for i=1:length(T)
    fprintf(fich,'%6d,%6d\n',pf(i),T(i));
end
fprintf(fich,'*Damage Evolution, type=DISPLACEMENT\n');
fprintf(fich,'%6d,\n',0.001);
% Close file
fclose(fich);
```

A.2 MATLAB code for generating material card with BWH-criterion

```
clc
clear all

%%%%%%%%%%%%%%%%%%%%%%%%%%%%%%%%%%%%%%%%%%%%%%%%%%%%%%%%%%%%%%
%%%%%%%%%%%%%
% Define material parameters
%%%%%%%%%%%%%%%%%%%%%%%%%%%%%%%%%%%%%%%%%%%%%%%%%%%%%%%%%%%%%%
%%%%%%%%%%%%%

rho = 2.7e-9; % Density
E0 = 60000; % Young's modulus
nu = 0.33; % Poisson's ratio
sigma0 = 250; % Yield stress
K = 420; % Power law modulus
n = 0.180; % Power law exponent
epspl = 0; % Yield plateau strain
matname = 'SMM_AA6082_T6'; % Name of the material card

%%%%%%%%%%%%%%%%%%%%%%%%%%%%%%%%%%%%%%%%%%%%%%%%%%%%%%%%%%%%%%
%%%%%%%%%%%%%
% Mesh scaling factor
%%%%%%%%%%%%%%%%%%%%%%%%%%%%%%%%%%%%%%%%%%%%%%%%%%%%%%%%%%%%%%
%%%%%%%%%%%%%

element_size = 20; % Shell element size
plate_thickness = 4; % Shell element thickness
scale_factor = (1+plate_thickness/element_size)/2; % Scaling
factor

%%%%%%%%%%%%%%%%%%%%%%%%%%%%%%%%%%%%%%%%%%%%%%%%%%%%%%%%%%%%%%
%%%%%%%%%%%%%
% Define additional parameters
%%%%%%%%%%%%%%%%%%%%%%%%%%%%%%%%%%%%%%%%%%%%%%%%%%%%%%%%%%%%%%
%%%%%%%%%%%%%

p = (0:0.001:3)'; % Equivalent plastic strain
beta = (-0.999:0.001:1)'; % Strain rate ratio

%%%%%%%%%%%%%%%%%%%%%%%%%%%%%%%%%%%%%%%%%%%%%%%%%%%%%%%%%%%%%%
%%%%%%%%%%%%%
% Compute stress strain curve
%%%%%%%%%%%%%%%%%%%%%%%%%%%%%%%%%%%%%%%%%%%%%%%%%%%%%%%%%%%%%%
%%%%%%%%%%%%%

epsp0 = (sigma0/K)^(1/n)-epspl; % strain for power law
for i=1:length(p)
    if p(i,1) <= epspl
        sigmay(i,1) = sigma0;
    else
```

```
        sigmay(i,1) = K*(p(i,1)+epsp0)^n;
    end
end

figure
plot(p,sigmay,'r')
grid on
xlabel('equivalent plastic strain')
ylabel('Yield stress')

csvwrite('yield_stress.csv',[p,sigmay]) % Export the stress-
strain curve
                                        % for plot
%%%%%%%%%%%%%%%%%%%%%%%%%%%%%%%%%%%%%%%%%%%%%%%%%%%%%%%%%%%%%%
%%%%%%%%%%%%%
% Compute BWH
%%%%%%%%%%%%%%%%%%%%%%%%%%%%%%%%%%%%%%%%%%%%%%%%%%%%%%%%%%%%%%
%%%%%%%%%%%%%

for i=1:length(beta)
    if beta(i) <= 0.0
        factor1 =
2*K*(1.0+beta(i)/2)/(sqrt(3*(beta(i)^2+beta(i)+1)));
        factor2 =
2*sqrt(beta(i)^2+beta(i)+1)/(sqrt(3)*(1.0+beta(i)));
    else
        factor1 = 2*K/(sqrt(3*(1-(beta(i)/(2+beta(i)))^2)));
        factor2 = 2/sqrt(3);
    end
    sig1c(i) = factor1*(factor2*n*scale_factor)^n;
    sig2c(i) = (2*beta(i)+1)/(2+beta(i))*sig1c(i);
end

figure
plot(sig2c/K,sig1c/K,'r')
grid on
xlabel('sigma2/K')
ylabel('sigma1/K')
csvwrite('BWH_locus.csv',[sig2c'/K,sig1c'/K]) % Export the
critical
%                                               principal
stress for plot

%%%%%%%%%%%%%%%%%%%%%%%%%%%%%%%%%%%%%%%%%%%%%%%%%%%%%%%%%%%%%%
%%%%%%%%%%%%%
% Write material card
%%%%%%%%%%%%%%%%%%%%%%%%%%%%%%%%%%%%%%%%%%%%%%%%%%%%%%%%%%%%%%
%%%%%%%%%%%%%

disp('Write material card');
```

```
fich=fopen('mat_baseT6_BWH_tykkelse.inp','w'); %Input file
name
% Write material card name
fprintf(fich,['*Material, name=' matname '\n']);
% Write density
fprintf(fich,'*Density\n');
fprintf(fich,'%6d,\n',rho);
% Write elastic properties
fprintf(fich,'*Elastic\n');
fprintf(fich,'%6d,%6d\n',E0,nu);
% Write crushable foam keyword

fprintf(fich,'*Plastic\n');
for i=1:length(p)
    fprintf(fich,'%6d,%6d\n',sigmay(i,1),p(i,1));
end

% Add fracture model
fprintf(fich,'*Damage Initiation, criterion=FLSD\n');
for i=1:length(beta)
    fprintf(fich,'%6d,%6d\n',sig1c(i),sig2c(i));
end

fprintf(fich,'*Damage Evolution, type=DISPLACEMENT\n');
fprintf(fich,'%6d,\n',0.001);
fclose(fich);
```

References

1. **Norwegian Public Roads Administration.** Coastal Highway Route E39. *Coastal Highway Route E39 Summary.* [Online] May 05, 2016. http://www.vegvesen.no/_attachment/300340/binary/527486?fast_title=Ferjefri+E39+summary+January+2012+%28English%29.pdf.

2. **Backman, M.E. and Goldsmith, W.** The mechanics of penetration of projectiles into targets. *International Journal of Engineering Science, Vol. 16.* 1978, pp. 1-99.

3. **Børvik, T.** *Ballistic Penetration and Perforation of Steel Plates.* s.l. : Faculty of Engineering Science and Technology (IVT,NTNU), 2001.

4. **Zukas, J.A.** *IMPACT DYNAMICS: THEORY AND EXPERIMENT.* s.l. : US Army Armanent Research And Development Command, 1980.

5. **Langseth, M. and Larsen, P.K.** Dropped objects' plugging capacity of steel plates: An. *International Journal of Impact Engineering, Vol. 9, No 3.* 1990, pp. 289-316.

6. **Langseth, M and Larsen, P.K.** The behavior of square steel plates subjected to a circular blunt ended load. *International Journal of Impact Engineering, Vol.12.* 1992.

7. —. Dropped objects' plugging capacity of aluminium alloy plates. *International Journal of Impact Engineering, Vol.15.* 1994, pp. 225-241.

8. **Langseth, M., Hopperstad, O. S. and Berstad, T.** Impact Loading of Plates: Validation of Numerical Simulations by Testing. *International Journal of Offshore and Polar Engineering, Vol. 9.* 1999.

9. **Wang, G., Arita, K and Liu, D.** Behavior of a double hull in a variety of stranding or collision scenarios. *Marine Structures, Vol. 13.* 2000, pp. 147-187.

10. **Hildrum, Hilde Giæver.** *Stiffened aluminum plates subjected to impact loading.* s.l. : Dr.ing thesis, Department of Structural Engineering, NTNU, 2002.

11. **Liu, B., Villavicenio, R. and Guedes Soares, C.** Simplified analytical method to evaluate tanker side panels during minor collision incidents . *International Journal of Impact Engineering, Vol. 78.* 2015.

12. **Kårstad, Bente Larsen and Skajaa, Birgitte.** *Impact behaviour of stiffened aluminium plates.* s.l. : Master thesis, Department of Structural Engineering, NTNU, 2015.

13. **Hydro.** Aluminium, enviroment and society. *Hydro: Aluminium and health.* [Online] May 03, 2016. http://www.hydro.com/upload/Documents/downloadcenter/About%20aluminium/Aluminium_environment-and-society.pdf.

14. **Wang, T.** *Modelling of Welded Thin-Walled Aluminium Structures.* s.l. : Doctoral thesis, Department of Structural Engineering. NTNU, 2006.

15. **Callister, William D. Jr.** *Materials Science and Engineering: An introduction (7th edition).* s.l. : John Wiley & Sons inc., 2007.

16. **Sapa.** Sapa Industrial Extrusions. *Extruded Aluminium* . [Online] [Cited: May 24, 2016.] http://www.sapagroup.com/pages/522574/Brochures/Sapa%20Alloy%206082.pdf.

17. **Norwegian Standard.** *Aluminium and aluminium alloys, Temper designations.* s.l. : Norsk Standard, 1993.

18. **Porter, D.A and Easterling, K.E.** *Phase transformations in metals and alloys (2nd ed.).* London : Chapman & Hall, 1992.

19. **Grong, Øystein.** *Metallurgical Modelling of Welding (2nd edition).* s.l. : Institute of Materials , 1997.

20. **Kallee, S. W., Nicholas, E. D. and Thomas, W. M.** Friction stir welding - invention, innovations and applications. *TMS Friction Stir Welding and Processing Conference.* 2001.

21. **Mistikoglu, S. and Çam, G.** Recent Developments in Friction Stir Welding of Al-alloys. *Journal of Materials Engineering and Performance, vol. 23.* 2014, pp. 1936-1953.

22. **Ashby, Michael F. and Jones, David R. H.** *Engineering Materials 1 - An Introduction to Properties, Applications and Design (4.th edition).* s.l. : Elsevier, 2012.

23. **Hopperstad, O. S. and Børvik, T.** *Lecture Notes, Material Mechanics, Part 1.* s.l. : Structural IMpact Laboratory, NTNU, 2013.

24. **Dieter, George E.** *Mechanical Metallurgy.* s.l. : McGraw-Hill Book Company, 1988.

25. **Lubliner, Jacob.** *Plasticity Theory (Revised Edition).* s.l. : Courier Corporation, 2005.

26. **Lademo, O. G., Hopperstad, O. S. and Langseth, M.** An evaluation of yield criteria and flow rules for aluminium alloys. *International Journal of Plasticity, vol. 15.* 1999, pp. 191-208.

27. **Chen, Y., et al.** Stress–strain behaviour of aluminium alloys at a wide range of strain rates. *International Journal of Solids and Structures, vol. 46.* 2009, pp. 3825–3835.

28. **Hosford, William F.** *Mechanical Behavior of Materials (2nd edition).* s.l. : Cambridge University Press, 2009.

29. **Pineau, A., Benzerga, A. A. and Pardoen, T.** Failure of metals I: Brittle and ductile fracture. *Acta Materialia, vol. 107.* 2016, pp. 424-483.

30. **Srivatsan, T. S., Vasudevan, S. and Park, L.** The tensile deformation and fracture behaviour of friction stir welded aluminium. *Materials Science and Engineering: Volume 466, Issue 1-2.* 2007, pp. 235-245.

31. **Liu, H. J., et al.** Tensile properties and fracture locations of friction-stir-welded joints of 2017-T351 aluminium alloy. *Journal of Materials Processing Technology, Volume 142, Issue 3.* 2003, pp. 692-696.

32. **Moreira, P. M. G. P., et al.** Mechanical and metallurgical characterization of friction stir welding joints of AA6061-T6 with AA6082-T6. *Materials & Design, Volume 30, Issue 1.* pp. 180-187.

33. **Ule, B., et al.** *Cockcroft-Latham Fracture Criterion and Bulk Formability of Copper Base Alloys.* Ljubljana, Slovenia : Faculty for Mechanical Engineering, 1994.

34. **Cockroft, M. G. and Latham, D. J.** Ductility and workability of metals. *Journal of the Institute of Metals.* 1968, pp. 33-.

35. **Alsos, H. S., et al.** Analytical and numerical analysis of sheet metal instability using a stress based criterion. *International Journal of Solid and Structures, Volume 45, Issue 7-8.* 2008, pp. 2042-2055.

36. **Viatkina, E. M, Brekelmans, W. A. M and Geers, M. G. D.** *Forming limit diagrams for sheet deformation processes.* s.l. : Netherlands Institute for Metals Research, Eindhoven University of Technology, Department of Mechanical Engineering, 2001.

37. **He, J., et al.** Effect of nonlinear strain paths on forming limits under isotropic and anisotropic hardening. *International Journal of Solids and Structures, Volume 51, Issue 2.* 2014, pp. 402-415.

38. **Hill, R.** *On discontinuous plastic states, with special reference to localized necking in thin sheets.* s.l. : Department of Theoretical Mechanics, University of Bristol, 1952.

39. **Alsos, H.S, Amdahl, J. and Hopperstad, O.S.** On the resistance to penetration of stiffened plates, Part II: Numerical analysis. *International Journal of Impact Engineering, Volume 36, Issue 7.* 2009, pp. 875-887.

40. **Bressan, J. D. and Williams, J. A.** The use of a shear instability criterion to predict local necking in sheet metal deformation. *International Journal of Mechanical Sciences, vol. 25.* 1983, pp. 155-168.

41. **Cook, Robert D., et al.** *Concepts and Applications of Finite Element Analysis, 4th Edition.* s.l. : John Wiley & Sons, inc, 2002.

42. **Hughes, Thomas J. R.** *The Finite Element Method: Linear Static and Dynamic Finite Element Analysis* . s.l. : Dover, 2012.

43. **Mathisen, Kjell Magne.** Formulation of Geometrically Nonlinear FE. *Sintef - Geilo Winter School.* [Online] 2012. [Cited: May 15, 2016.] https://www.sintef.no/globalassets/project/evitameeting/2012/kmm-geilo-2012-lecture-11b.pdf.

44. —. Solution Methods for Nonlinear Finite Element Analysis (FEA). *Sintef - Geilo Winter School.* [Online] 2012. [Cited: May 14, 2016.] https://www.sintef.no/globalassets/project/evitameeting/2012/kmm-geilo-2012-lecture-11a.pdf.

45. **Dassault Systèmes.** *Abaqus 6.14: Abaqus Theory Guide.* 2016.

46. **Mathisen, Kjell Magne.** *TKT4197 Nonlinear Finite Element Analysis, Lecture 9: Solution of the Num. Dyn. Equil. Eq.* s.l. : Department of structural engineering, NTNU, 2015.

47. **Dassault Systèmes.** *Abaqus 6.14: Abaqus Analysis User's Guide.* 2016.

48. **Mathisen, Kjell Magne.** Finite element modelling of structural mechanics problems. *Sintef - Geilo Winter School.* [Online] 2012. [Cited: May 14, 2016.] https://www.sintef.no/globalassets/project/evitameeting/2012/kmm-geilo-2012-lecture-10.pdf.

49. **iMechanica.** iMechanica - web of mechanics and mechanicians. *Explicit analysis: Quasi-static.* [Online] 2006. [Cited: May 26, 2016.] http://imechanica.org/files/l5-quasi-static.pdf.

50. **Dassault Systèmes.** Abaqus 6.14: Getting started with Abaqus, interactive edition. [Online] 2016. [Cited: April 10, 2016.] http://abaqus.software.polimi.it/v6.14/books/gsa/default.htm.

51. **Bell, Kolbein.** *An engineering approach to FINITE ELEMENT ANALYSIS of linear structural mechanics problems.* s.l. : Fagbokforlaget Vigmostad & Bjørke AS, 2014.

52. **Engineering Toolbox.** Friction and Friction Coefficients. [Online] May 14, 2016. http://www.engineeringtoolbox.com/friction-coefficients-d_778.html.

53. **Paulo, R.M.F, Teixeira-Dias, F. and Valente, R.A.F.** Numerical simulation of aluminium stiffened panels subjected to axial compression: Sensitivity analyses to initial geometrical imperfections and material properties. *Thin-Walled Structures, vol. 62.* 2013, pp. 65-74.

54. **EUROPEAN COMMITTEE FOR STANDARDIZARION (CEN).** *Eurocode 3: Design of Steel Structures. Part 1-8: Design of Joints.* s.l. : Norwegian Standard, 2009.

55. —. *Eurocode 3: Design of Steel Structures: Part 1-1: General Rules and Rules for Buildings.* s.l. : Norwegian Standard, 2008.

56. **Nanninga, Nicholas E.** *High cycle fatigue of AA6082 and AA6063 aluminum extrusions.* Michigan Technological University. s.l. : Michigan Tech, 2008.

57. **Khadyko, M, et al.** An experimental–numerical method to determine the work-hardening of anisotropic ductile materials at large strains. *International Journal of Mechanical Sciences, vol. 88.* 2014.